

Anticrack Model for Slab Avalanche Release

Zur Erlangung des akademischen Grades
Doktor der Ingenieurwissenschaften
der Fakultät für Maschinenbau
Universität Karlsruhe (TH)

genehmigte
Dissertation
von

Ing. phys. dipl. Joachim Heierli

Tag der mündlichen Prüfung: 19. Dezember 2008
Hauptreferent: Prof. Dr. rer. nat. habil. Peter Gumbsch Ord.
Korreferent: Prof. Dr. rer. nat. habil. Michael Zaiser

Contents

0.1	Abstract	vi
0.2	Zusammenfassung	vii
0.3	Common symbols	viii
0.4	Acknowledgments	ix
1	Introduction	1
1.1	Slab avalanches and whumpfs	1
1.2	Debris collapse	3
1.3	Cracks and anticracks	4
1.4	Brittle fracture	7
1.5	Crack energy	8
2	Review of experimental evidence	9
2.1	Slope angle	9
2.2	Snowpack subsidence	10
2.3	Specific fracture energy	14
2.4	Artificial triggering	15
2.5	Crack-face friction	17
2.6	Young's modulus of snow	18
3	Review of avalanche release models	19
3.1	Simple shear models	20
3.1.1	Short cracks	20
3.1.2	Long cracks	21
3.1.3	Long cracks in a brittle weak layer of finite thickness	24

3.1.4	Formation energy for shear cracks	25
3.2	Collapse models	25
3.2.1	The flexural wave model	25
3.2.2	The solitary wave model	26
3.2.3	Nucleation of collapse waves	28
3.3	Statistical physics approach	29
4	Anticrack nucleation	31
4.1	Energy of formation of a mixed-mode anticrack	31
4.2	Generalisation to arbitrary elastic mismatch	39
4.3	Limiting cases	40
4.4	Nucleus instability	41
4.5	Skier instability	42
4.6	Gap instability	43
4.7	Derivations	44
4.7.1	Energy of an anticrack nucleus.	44
4.7.2	Energy of an anticrack with free faces	45
4.7.3	Energy of a notch	50
4.7.4	Energy reduction by a line force	51
4.8	Numerical verification	53
4.9	Examples	55
5	Anticrack propagation	63
5.1	Action functional for collapse waves	63
5.2	General asymptotic solution	64
5.3	Approximate asymptotic solution	66
5.4	Example	68
6	Discussion	69
6.1	Model validation	69
6.1.1	Experiments	69
6.1.2	Phenomenology	74

6.2	Scaling relations	75
6.3	Discussion of model assumptions	76
6.4	Interpretation of the anticrack model	78
6.5	Triggering mechanisms	83
6.6	Further research	84
7	Conclusion	87
A	Material properties of snow and ice	93
B	FEM results for crack energies	95

0.1 Abstract

The aim of this thesis is to lay the groundwork for a new and comprehensive theory of slab avalanche release in dry snow. Simple shear fracture models have long been considered as standard explanation of slab avalanche formation. These models assume brittle fracture to take place in a slip plane of zero thickness. The change in strain energy in response to crack formation then depends only on the shear loading of the slip plane, but not on the compressive loading. In reality, the fracture process takes place in a weak layer composed of sparsely packed ice grains. When such a granular aggregate fails, the debris pack tighter and the weak layer undergoes a reduction in volume, resulting in the subsidence of overlying snowpack layers. As a consequence, the change in strain energy also depends on the compressive loading of the weak layer. It is shown that subsidence significantly contributes to the driving force for crack nucleation and crack propagation, and that failure nucleates as a mixed-mode anticrack and propagates as a non-linear wave which progressively delaminates the slab over a large area. In the first part of the work the mechanical energy of an anticrack resulting from a collapsed section in the weak layer is calculated. The anticrack experiences gravity-induced shear stress τ and compressive stress σ . It is shown that anticrack energy can be partitioned into a contribution proportional to τ^2 and one proportional to σ^2 . The energy of a notch can be partitioned into contributions proportional to τ^2 , $\sigma\tau$ and σ^2 . From the expressions for crack and notch energies, criteria for fracture propagation are deduced, in particular for cracks of size zero (spontaneous crack nucleation). It is found that skiers and gaps in the snowpack can nucleate slab avalanches even if there are no pre-cracked areas in the weak layer. In the second part of this work an asymptotic solution describing the propagation of fracture in weak layers is proposed. The corresponding action functional is formulated and non-linear wave solutions with velocity below the shear wave speed are analysed. Expressions for the propagation velocity, wavelength, deformation profile and dispersion of the non-linear collapse waves are obtained.

Experimental evidence from field tests confirms the developed criterion for fracture propagation in weak layers. Experiments on long snow samples, in which the deformation field during fracture propagation is measured with high precision, confirm the calculated properties of the collapse waves. The anticrack model explains instabilities known as whumpfs, their connection with avalanche hazard, as well as the remote triggering of avalanches. The calculation leads to a two-stage scenario of slope failure. In the first stage, nucleation and propagation of a mixed-mode anticrack delaminates the slab from the snow below. This process can occur with or without shear loading and for arbitrary amounts of crack-face friction. In the second stage frictional forces between the crack faces decide whether the slab will slide, causing an avalanche, or subside, causing a whumpf.

0.2 Zusammenfassung

Das Ziel dieser Promotionsarbeit ist die Erstellung der Grundlagen für eine neue und umfassende Theorie der Auslösung von Schneebrettlawinen. Scherbruchmodelle galten bisher als Standarderklärung der Schneebrettauslösung. In diesen Modellen wird angenommen, dass ein spröder Scherbruch ohne Volumenänderung des Materials stattfindet, so dass die Änderung der Verzerrungsenergie allein von den Scherkräften in der Bruchebene abhängt. Tatsächlich aber findet der Bruch in einer schwachen Schneeschicht endlicher Dicke statt, die aus lose gepackten Eiskörnern besteht. Bricht dieses Aggregat, entsteht eine Schuttmasse, die dichter gepackt ist als das ursprüngliche Material, so dass eine Volumenreduktion eintritt. Dadurch leisten auch die kompressiven Kräfte in der Schneedecke Arbeit. Es wird gezeigt, dass diese Arbeit nicht vernachlässigt werden kann. Dabei stellt sich heraus, dass der Kollaps der schwachen Schneeschicht als Antiriss beginnt und sich in Form einer nicht-linearen Kollapswelle fortpflanzt, welche die zuvor gebundenen Schneeschichten grossflächig abtrennt. Im ersten Teil der Arbeit wird die mechanische Energie eines Antirisses berechnet, welcher aus einem kollabierten Abschnitt der Schwachschicht hervorgeht. Der Antiriss unterliegt einer Scherspannung τ und einer Druckspannung σ . Es zeigt sich, dass die Energie des Antirisses in Beiträge proportional zu τ^2 und proportional zu σ^2 aufgeteilt werden kann. Die Energie einer Kerbe hingegen kann in Beiträge proportional zu τ^2 , zu $\sigma\tau$ und zu σ^2 aufgeteilt werden. Aus den analytischen Ausdrücken für Antiriss- und Kerbenenergie ergeben sich Kriterien für spontane Bruchausbreitung. Insbesondere wird das spontane Wachstum von Antirissen oder Kerben der Länge null untersucht. Damit kann gezeigt werden, dass spontane Bruchnukleation durch Skifahrer wie auch durch Lücken in der Schneedecke in einer intakten, nicht vorgebrochenen Schwachschicht möglich ist. Im zweiten Teil wird eine asymptotische Lösung für die Bruchausbreitung vorgeschlagen. Das betreffende Wirkungsfunktional wird angeschrieben und Lösungen, die sich mit einer Geschwindigkeit unterhalb der von Scherwellen ausbreiten, werden analysiert. Es ergeben sich analytische Ausdrücke für Ausbreitungsgeschwindigkeit, Wellenlänge, Verschiebungsprofil und Dispersion der Kollapswelle.

Feldexperimente bestätigen die Kriterien für die Bruchausbreitung für den Fall künstlich erzeugter Kerben. Experimente an Schneeschichtungen, bei welchen die Verschiebung mit hoher Genauigkeit gemessen wurde, bestätigen berechnete Eigenschaften der Kollapswelle. Das Antirissmodell erklärt die als Wummgeräusche bekannte Instabilität von Schnee, ihre Verknüpfung mit Schneebrettlawinengefahr, und die Möglichkeit der Fernauslösung von Schneebrettlawinen. Die Berechnungen führen zu einem Zweiphasenszenario der Schneebrettauslösung. In der ersten Phase entsteht der Antiriss, breitet sich aus, und trennt die aneinandergrenzenden Schneeschichten von einander ab. Dieser Prozess kann auch ohne Scherspannung und mit beliebig grosser Bruchflächenreibung ablaufen. In der zweiten Phase entscheidet die Reibung, ob das Schneebrett als Lawine abgleitet oder als Wummgeräusch nur absackt.

0.3 Common symbols

Latin:

c	Propagation velocity of collapse wave.
c_p	Propagation velocity of longitudinal wave, $c_p = (E/\rho)^{1/2}$.
c_s	Propagation velocity of shear wave, $c_s = (kG/\rho)^{1/2}$.
E	Elastic modulus of slab material for plane deformation.
E_0	Elastic modulus of substrate material for plane deformation.
g	Acceleration of gravity.
G	Shear modulus of slab material for plane deformation.
G_0	Shear modulus of substrate material for plane deformation.
h	Slab thickness (slope-normal).
h_f	Collapse amplitude (slope-normal).
k	Timoshenko's correction factor ($k=5/6$ for rectangular sections).
l_0	Half-length of anticrack at tangency (first crack-face contact).
l	Unsupported length of anticrack after tangency, wavelength of collapse wave.
p	Line charge on the slab, force per unit width (e.g. N/m).
r	Crack half-length
u_x, u_y	Slope-parallel, slope-normal displacement of a point on the slab's centre line.
V	Crack energy.
w_f	Specific fracture energy of weak layer.
x, y	Slope-parallel and slope-normal coordinates.

Greek:

α, β	Dundurs' elastic mismatch parameters for interface cracks.
η	Elastic constant, $\eta = [E/(3kG)]^{1/2}$.
μ	Coulomb friction coefficient between crack faces.
ν	Poisson's ratio of slab material.
ν_0	Poisson's ratio of substrate material.
ψ	Rotation angle of a cross section of the superstratum.
σ	Far-field compressive stress at the surface of the interface layer, $\sigma = -\rho hg \cos \theta$.
τ	Far-field shear stress at the surface of the interface layer, $\tau = \rho hg \sin \theta$.
τ_r	Friction force per unit surface of the interface layer, $\tau_r = \min(\tau , \mu \sigma)$.
τ_f	Resultant shear stress on weak layer, $\tau_f = \tau - \tau_r$.
θ	Slope angle.
θ_μ	Friction angle of crack faces, $\theta_\mu = \arctan \mu$.

0.4 Acknowledgments

The present work emerged during my joint activity as research associate at the Centre for Materials Science and Engineering of the University of Edinburgh and as Ph.D. student at the Institute for Reliability of Systems and Components of the Karlsruhe Institute of Technology between January 2007 and October 2008. The research was funded by the European Commission under the "New and Emerging Science and Technologies Pathfinder" programme "Triggering Instabilities in Materials and Geosystems" (contract NEST-2005-PATH-COM-043386, <http://www.trigs.eu>) and the DFG project Gu367/30.

I have been very fortunate for getting in personal touch with two distinguished materials physicists, Professor Peter Gumbsch and Professor Michael Zaiser, who took joint responsibility of my Ph.D. formation. Both took large influence on my academic education and gave a persuasive direction to my research. They generously enabled me to conduct a Ph.D. research on a subject of my own choice, and governed me very liberally and efficiently in doing so. I would like to express my gratitude to both of them in equal shares.

I would like to thank Alec van Herwijnen for the very stimulating collaboration. His talent for impeccable experimentation is the perfect counterpart to my theoretical appetite. He realised and evaluated the experiment presented in section 6.1.1. Likewise, I am most grateful to Alain Duclos for linking theory and practice. His many years of experience under field conditions and the database <http://www.data-avalanche.org> he attends were of invaluable help during the making of this thesis. For pleasantly biting scientific debate and most useful advice my profound appreciation is due to Henning Löwe, Jane Blackford and Prof. François Louchet. For kindly sharing all sorts of information I am indebted to Stéphane Caffo, Luca Egli, Dave Gauthier, Stefan Harvey, Prof. Bruce Jamieson, Martin Jonsson, Prof. Ian Main, Jürg Schweizer and Christian Sigrist. Jakob Rhyner gave me precious support in the early days when I started to dig into the present subject. Karim Ghazi-Wakili nucleated the idea to go for a Ph.D. and pushed me over the energy barrier. Monika Seifried and my family provided me with loving support during my stay in the Scottish capital.

The Royal Society under the international joint project grant No. R39010 started me up financially when I arrived in Edinburgh in early January 2007. Part of the present work has previously been published in *Science* [31] and *Cold Regions Science and Technology* [33]. Most of the theoretical research was carried out with Maple 10 for formal mathematics, CRAN R for numerical programming and ANSYS 11 for finite element modelling.

Chapter 1

Introduction

1.1 Slab avalanches and whumpfs

Snow avalanches occur in two fundamentally different modes. Loose snow avalanches fan out from one point, entraining granules of snow of low cohesion by collisions. They often occur during manifest meteorological events such as snow storms or rapid warming. Slab avalanches are the result of fracture processes which releases a large area of snowpack at once. They release spontaneously or may be triggered by human activities such as skiing, walking, use of explosives or driving snow vehicles. Slab avalanches may be considerably delayed with respect to manifest meteorological events. They originate in the extended failure of a subsurface layer in stratified snow [53]. As shown in Fig. 1.1, the primary fracture plane is located in the subsurface layer on the base of the slab [65]. The slab progressively debonds from the substrate by propagation of fracture along this layer, which subsequently acts as a sliding plane and erodes. The peripheral wall is a secondary fracture plane resulting from tensile or shear failure of the slab subsequent to the failure of the weak basal layer [65]. Once the secondary fracture cuts out a portion of the slab, this portion starts avalanching. In the present work the fracture process is assumed to take place in dry snow. In this case, no melt water is present in the primary fracture plane.

The first step in understanding the formation of slab avalanches is the comprehension of another instability typical of snow: the so-called 'whumpf'. A whumpf is a sudden subsidence of the snowpack over a more or less wide area, perceived by skiers¹ as a brief shake of the snow cover accompanied by more or less perceptible acoustic emission. The term whumpf is an echoism of this perception. In perennial snow and polar firns, the term 'firn-quake' has been used to describe a similar phenomenon [14]. For a long time practitioners have perceived whumpfs as warning signs of imminent avalanche hazard [8, 29, 85]. Curiously however, snowpack subsidence and whumpfs have received little attention in the snow science literature for a

¹When speaking of skiers in the text, any other type of human presence on the snowpack is meant to be included, e.g. snowboarders, pedestrians, occupants of (motor)sledges and other snow-vehicles.



Figure 1.1: Fracture pattern showing the basal fracture plane (eroded) and the peripheral wall. This slab avalanche of exceptional size released spontaneously at Glacier du Vallonnet, France, on April 4 2007. The slab was over 2 m thick. Photo: A. Duclos, www.data-avalanche.org.

long time. It is only a few years now since whumpfs were first studied systematically in field experiments [40]. Previous to the present work, the role of subsidence in the nucleation of fracture was obscure and has never been modelled. From the point of view of the established models of avalanche formation, subsidence was regarded as a secondary process which is subsequent to shear fracture and plays no direct role in slope failure. Snowpack subsidence and whumpfs are at times still dismissed today as warning signs of snowpack instability. The following account of an avalanche incident is extracted from the database www.data-avalanche.org:

"Nous n'avions rien à faire dans une face sud à 15 h ce jour (pourtant la neige encore dure sous la face sud-ouest nous a fait croire qu'on avait encore un peu de temps). Les 2 woufs avec tassement du manteau pendant la montée (dans des endroits plats) ont éveillé notre attention mais auraient dû tirer la sonnette d'alarme." Olivier Lesbros, Petit Pinier, Face SO, 02/2008.²

When afterwards the skiers descended into a large slope, they triggered a slab avalanche but luckily escaped. One skier was able to ski out of the slab while it was already in motion, the other was on the edge of the slab and only entrained for a few metres. The two skiers involved in this incident will certainly pay increased attention to whumpfs during their next outings. Meanwhile, one goal of the present work will be to find an explanation for the connection between whumpfs and slab avalanches. In doing so, a simple question needs to be answered: what exactly

²We had nothing to do in a south-facing slope at 3 p.m. this afternoon (however the snow was still hard in southwestern slopes and we thought we had a little more time). During the climb, two whumpfs with subsidence of the snow cover (on flat ground) raised our concerns but should have rung the alarm bells [translated by author].

happens in the snowpack during fracture? Is it a simple shear fracture (a local slip) that triggers the slab avalanche as postulated by the established models?

As a material, snow is an aggregate of small, often monocrystalline grains of ice [6]. The grains can be approximately spherical, polyhedron-shaped or planar and measure between a few tenths of a millimetre and a few millimetres in size. They do not generally slip over each other but are bonded by cohesive forces. Therefore a highly sparse microstructure can be maintained over time, the bulk density of which can be as low as 50 kg/m^3 . This granular aggregate is permanently in a transient state of sintering, driven by grain boundary diffusion, surface diffusion and sublimation-condensation [3, 6]. Consequently, the granular structure constantly changes and internal stresses continually adapt to new boundary conditions. This aggregate constitutes, according to Kirchner [44], a remarkably weak, brittle and unreliable material. Kirchner reported that the failure strength of fresh snow follows a Weibull distribution with modulus between 1 and 2. Compared with common materials, this value is extremely low. A particular snow specimen has therefore a high probability to break under a fraction (or a multiple) of the average stress sustained by many such samples.

Understanding slab avalanches is of direct relevance to the public. Avalanche hazard along traffic routes implies road and railway closures, hampers public mobility and causes distress to the temporarily isolated population. Heavy snowfalls vastly disrupt human activities, supplies and infrastructure but at the same time are a welcome prospect for recreation and winter sports. The questions how and why snow slopes turn unstable and regain stability, and how a single skier can trigger vast avalanches involving thousands of tons of snow, place snow avalanche research into the realm of materials science.

1.2 Debris collapse

Intact snow occupies between two and twenty times the specific volume occupied by its condensed phases - water and ice. Once fractured, its debris occupies a fraction of the specific volume of the previously intact snow (Fig. 1.2). As a familiar example, we may suddenly sink in when we step over a surface of snow. In fact, this material property plays a key role in the understanding of whumpf and slab avalanche formation, for loss of volume within the material implies that previously supported layers may suddenly subside. This process contributes to the transformation of gravitational potential energy into strain energy and fracture energy.

Flimsy bodies like a house of cards, weak snowpack layers made up of surface hoar, depth hoar or faceted grains, but also sturdy bodies like a building can undergo volumetric collapse under failure. The reason is that the intact structure envelops more unoccupied space than the fractured pile of debris. Other assemblages of grains such as a face-centered cubic packing of stable, congruent spheres in three dimensions have no ability to collapse when undergoing

fracture. In that case, fracture is necessarily dilatant³.

In general, as fracture takes place, some materials undergo volumetric changes, which can be positive or negative. For example, non-cohesive granular assemblages alternate between dilatancy and gravitational compaction as a result of stick-slip dynamics under shear [78]. Cohesive granular assemblages can undergo a reduction in volume in addition to elastic compression, when applied stress is sufficient to break the cohesive bonds between grains. A physical example is given by porous sandstone, which can lose a fraction of its porosity under tectonic loading [74]. It is observed that the compaction is not evenly distributed throughout the volume of the sandstone, but concentrates in thin, planar bands named compaction bands. Another physical example is given in Fig. 1.2 which shows a collapsed and an uncollapsed section of a subsurface layer of old surface hoar in a seasonal snowpack [37]. The fracture pattern shown on this photograph was due to a whumpf caused by a skier. The debris collapsed and caused the snowpack to subside. In this particular case, subsidence propagated for about 8 m and then came to an abrupt stop. Where this happened, a vertical fracture plane was observed, cutting through the slab to the surface.

1.3 Cracks and anticracks

The strength of a material depends on the actual physical sample which is observed. Each individual physical sample contains a unique realisation of inhomogeneities, flaws and cracks, around which the fracture process may nucleate [27]. As long as the unique realisation of defects is unknown, the strength of a material is necessarily a random variable. There are two basic ways to study the effect of cracks and flaws on failure. Either one assumes a continuous body containing a single crack of variable size and studies the change in energy due to such a crack in response to applied stress - this is the realm of fracture mechanics - or one views the solid as a random medium accumulating damage in a statistical sense [2] and resorts to discretised computational physics to perform simulations of an aggregate of particles, ordered for example in a lattice [86]. If the levels of damage in the material are high prior to failure, the discrete description is preferable. If the levels of damage are low, failure is likely to be ruled by a single dominating crack, or a few of them. In this situation, the continuum description may be the more appropriate. These two basic ways can, of course, be combined by assuming one portion of the system continuous and the other discrete. In the present work, the continuum approach is chosen throughout the system.

Physically speaking, a *crack* is a disruption of the material in a solid body [27, 36]. In general terms it can be thought as occupying a portion of space where bonds are broken, of volume \mathcal{V}

³This statement was conjectured in 1611 by Kepler in a masterpiece of materials science *and* mathematics, in which he searches for an explanation for the hexagonal symmetry of snow flakes [41]. Kepler's conjecture is now considered proven, although apparently not to the unanimity of all mathematicians.

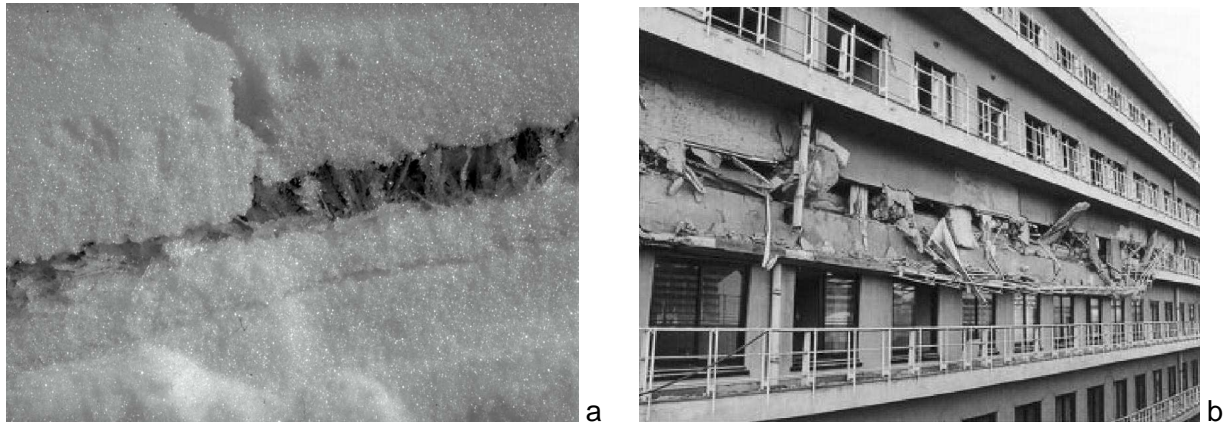


Figure 1.2: Volumetric collapse of debris. **a:** Arrested collapse due to a whumpf in buried surface hoar [37]. The debris on the left is less than 1 cm thick; the intact part on the right is 2 cm thick. Reprinted from the Journal of Glaciology with permission of the International Glaciological Society. **b:** Structural collapse of a building during the 1995 earthquake in Kobe, Japan. Only the middle floor collapsed, the other floors remained comparatively undamaged. Architectural Institute of Japan [16].

and envelope $\partial\mathcal{V}$ (N.B. \mathcal{V} can be of measure zero but not $\partial\mathcal{V}$). The disruption locally interrupts stresses, and therefore is a supplementary boundary condition to the system [1]. Topologically the internal surface of a crack and the external surface delimiting the entire body are equivalent, and can be treated in exactly the same manner. The presence of one or more cracks in a solid affects its internal energy, because the strain field adapts to the particular boundary conditions determined by the cracks.

A particular type of crack occurs for $\mathcal{V} = 0$ with finite envelope $\partial\mathcal{V} \neq 0$. Such cracks are essentially planar ("penny-shape" geometry). To understand how the presence of a planar crack affects the state of a homogeneous, linear-elastic solid, the intact solid (without crack) is assumed to be subjected to non-zero forces on its external surface (Fig. 1.3). This causes the solid to deform, resulting in an internal stress field expressed by the Cauchy stress tensor. At any point, six independent values σ_{ij} , $i, j = 1, 2, 3$ describe the state of stress in the intact solid. Let now a small, isolated crack of very small thickness d be centered in the solid (Fig. 1.3). This introduces new boundary conditions on the crack surface $\partial\mathcal{V} \cong B_1 \cup B_2$ and therefore a new stress field σ'_{ij} , $i, j = 1, 2, 3$. With the convention of summation over repeated indices, the boundary conditions are of the form $\sigma'_{ij}n_j = \sigma_i$, where the n_j are the components of the normal vector to either B_1 or B_2 and the σ_i are the imposed stresses on B_1 and B_2 (in the following one can assume $\sigma_i = 0$ for free crack surfaces). Choosing the coordinate system as shown in Fig. 1.3, one obtains $n_j = \pm\delta_{j2}$, and the boundary conditions become $\sigma'_{i2} = 0$. Therefore, the internal state is only affected by the crack if either $\sigma_{12} \neq 0$, $\sigma_{22} \neq 0$ or $\sigma_{32} \neq 0$, in which case

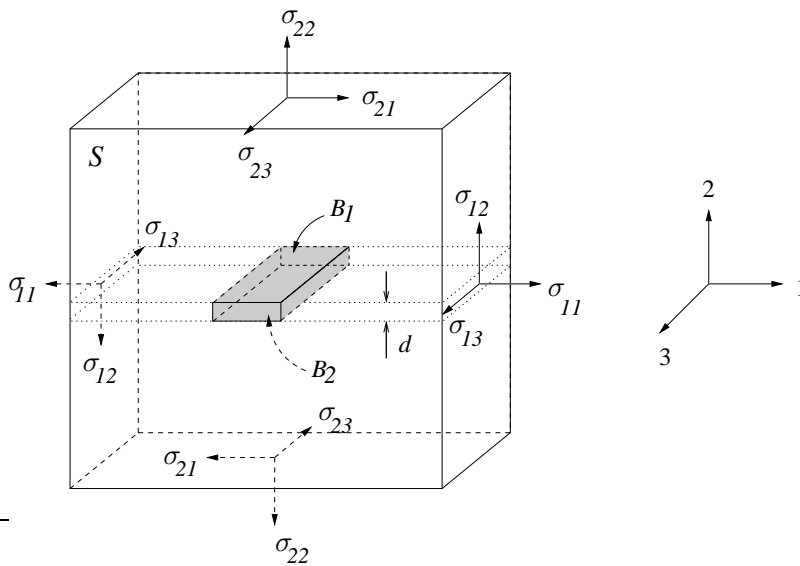


Figure 1.3: Fracture modes: Consider a volume element S containing a portion of crack of small thickness d and free crack faces B_1 and B_2 . The coordinate system is chosen with the 2-axis perpendicular to the crack plane, as shown. The crack section is in mode I if only the far-field stress $\sigma_{22} > 0$ is applied, in anticrack mode if only $\sigma_{22} < 0$ is applied, in mode II if only $\sigma_{12} \neq 0$ is applied and in mode III if solely $\sigma_{23} \neq 0$ is applied. If any of σ_{12} , σ_{22} and σ_{23} appear in pairs, the crack is in mixed-mode. If $d \rightarrow 0$, then σ_{11} , σ_{13} and σ_{33} do not affect the state of the crack.

the solid must deform to accommodate the new boundary conditions on B_1 and B_2 . The other components of the stress field (σ_{11} , σ_{13} , and σ_{33}) do not interact with the crack (if however the crack were not entirely planar or d significant, these components would also interact with the crack, for $n_j \neq \pm\delta_{j2}$). Each of the boundary conditions can be accommodated individually. As a result of linear elasticity the superposition principle is applicable and the general solution is a linear combination of the three individual solutions, or modes. The situation where $\sigma_{22} > 0$ but $\sigma_{12} = \sigma_{32} = 0$ is called mode I. Accordingly, $\sigma_{12} \neq 0$ but $\sigma_{22} = \sigma_{32} = 0$ is called mode II and $\sigma_{32} \neq 0$ but $\sigma_{22} = \sigma_{12} = 0$ is called mode III. A crack with only mode II and mode III components is termed a *shear crack*.

An *anticrack* is a crack subjected to a fracture mode in which the displacement field is equal in magnitude but opposite in sign to a classical mode I crack [18]. In standard materials this mode is not physically possible because of material interpenetration. In cohesive-granular materials, loss of cohesion may be accompanied by a reduction in specific volume of the resulting granular debris, clearing the space required for 'inward' displacement of the crack faces. Knight and Knight may be credited for the earliest observation of anticracks in superheated ice, in which material on either side of a nucleus moves towards the fracture plane due to volume decrease during melting [45]. Fletcher and Pollard proposed the concept of anticrack as an inverse mode I crack and applied it to rocks which may go in solution under high applied pressure, resulting in a deformation field with negative divergence in the surrounding rock [18]. More recently Sternlof,

Rudnicki and Pollard applied the anticrack concept to explain the formation of compression bands in sandstone [74]. Altogether it appears natural to apply the anticrack concept to snow. Fig. 1.2 gives an example where such an inward, anticrack-type fracture with volume reduction has occurred during a whumpf. The application of the anticrack concept to fracture in snow and its generalisation to limited volume reduction is the central topic of this work. It should be emphasised that, contrary to the antimode of mode I, the antimodes of mode II and mode III are indistinguishable from the modes II and III themselves.

A *notch*, finally, is a line defect in the outer surface of a body. Notches are caused by manufacturing, chemical action or mechanical contact with other solids. In snow they can be produced artificially with a snow-saw. Notches are likely to be of finite width and therefore allow anti-mode I displacements.

1.4 Brittle fracture

Brittle materials fail without accumulating significant amounts of plastic deformation. They feature an elastic stress-strain response until rupture (or nearly so) and fail suddenly. In brittle fracture, cracks tips of atomic sharpness propagate by the successive rupture of atomic bonds [28, 47]. In cohesive-granular materials, where granules replace atoms as indivisible particles, the scale of a crack-tip is many orders of magnitude larger. In snow, grain size ranges from 0.1 to about 5 mm, and this is a natural cut-off for the size of a crack tip in snow. Such cracks are therefore essentially macroscopic.

As opposed to brittle materials, ductile materials accumulate substantial amounts of plastic deformation before failure. Under sufficient loading, they undergo irreversible changes which affect their physical properties. Snow is ductile at low deformation rates and brittle at high deformation rates with a transition region between 10^{-4} and 10^{-3} s^{-1} [58]. As far as processes with higher rate are concerned, the brittle approximation is reasonable. This simplifies the evaluation of changes in energy as they can be calculated with elastic field theory, as done in most models of snow failure [5, 12, 50, 53].

In a brittle, homogeneous and isotropic material, a crack subjected to a combination of modes I, II and III preferentially grows into a direction normal to the mode I loading, effectively reducing its loading in the shear modes II and III [35]. For this reason cracks tend to propagate in mode I in such materials. Mode II cracking comes into play in the cracking of layered materials, especially along weak interfaces, but even interface cracks rarely and consistently develop in pure mode II, but mix with other mode components when the elastic properties of the materials on either side of the interface do not match [15, 35].

1.5 Crack energy

The energy of formation of a crack or simply *crack energy* is the sum of two contributions: Firstly, the energy expended in creating the new crack surfaces due to cohesive bonding in the fracture plane. Secondly, the difference in mechanical energy of the system in the final state (containing the crack) and the system in the initial state (in absence of the crack). Crack energy therefore depends on cohesion, geometry, applied stress and, if present, on other material defects such as pores or other cracks. In the present work, in which brittle fracture is assumed, a single crack is entirely characterised by a single size parameter r (its radius or half-length), and its crack energy is denoted by $V(r)$. The crack energy function is a powerful tool for analysing crack stability. It quantifies the energy required to create a crack of radius r in the system, and, by derivation, the change in energy to expand a crack of radius r by a small amount dr . If the derivative $\partial_r V(r)$ of the crack energy is negative, crack growth is energetically favourable at r . If $\partial_r V(r)$ is positive and crack growth is a reversible process, one would assume that the crack contracts. However, crack growth is quite often an irreversible process, and obviously so in the case of collapse. In this case the crack remains stuck at its current size r or disappears in time through the action of sintering.

The saddle points of the crack energy function and the behaviour in the neighbourhood of $r = 0$ are of special physical interest and lead to the notion of a critical crack. If a system with a crack of radius r is in a saddle point of the crack energy function, it fulfills the Griffith-Irwin criterion [27] and the crack can expand until it encounters a region of growing or constant $V(r)$. If on the other hand a system contains no macroscopic crack at all, one can equivalently view it as containing a crack of size $r = 0$, characterised by the crack energy $V(0) = 0$. If this system is in a state where $\partial_r V(0) \leq 0$, then a crack can nucleate from an infinitesimal fluctuation, at least from the view of continuum physics. Examples of this situation will be encountered in chapter 4. Once nucleated, the crack can expand until it hits a configuration where $\partial_r V(r) > 0$. If on the contrary $\partial_r V(r)$ remains negative during growth, the crack can cut through the entire system, which is said to fail. The determination of the saddle points can be carried out analytically or numerically by solving the equation $\partial_r V(r) = 0$ and ensuring that $\partial_{rr} V(r) < 0$.

Chapter 2

Review of experimental evidence

Until recently, the validation of theories aiming to explain snow avalanche formation was regarded as difficult or even impossible [64] and no data were available for the task. This unsatisfactory situation took a turning-point with two very significant contributions: the publication of the first fracture toughness measurements on snow by Kirchner, Michot and Suzuki in 2000 [43] and the publication of the propagation velocity of collapse waves in snow by Johnson, Jamieson and Stewart in 2004 [40]. These contributions triggered the development of new theoretical approaches, new laboratory experiments and new field techniques. In 2006/2007 several research teams independently proposed experiments destined to test the initiation and propagation of fracture in snow [24, 69, 72]. The bottom line of these experiments is to study the stability of snow samples under the influence of artificial cracks in order to quantify the propensity of the snowpack to propagate fracture.

2.1 Slope angle

Slab avalanches are generally said to release from slopes steeper than 30° , but this figure is rather indicative and occasionally quite lower release angles have been reported [62, 65]. Slope angle however cannot be characterised by a single value, such as an average. The tilt angle of the snowpack fluctuates considerably in space at various scales and even varies from layer to layer (especially in wind-loaded slopes). When a slab avalanche is triggered, the spatial distribution of the local tilt angle of the fracture plane in the release area is likely a decisive factor but it is rarely reported.

Concerning whumpfs, there seems to be no restrictions on slope angle. Whumpfs are observed on slopes of any angle and occur frequently in horizontal or low-angle terrain. Moreover, whumpfs triggered on flat ground can be immediately followed by the release of a remote slab avalanche on an adjacent slope [39]. Relative to the position of the trigger, the remote event may occur up or down slope, on the opposing flank of the valley (sometimes a kilometre away),

but also within the same slope. In these cases the fracture starts as a whumpf and subsequently becomes a slab avalanche within a remote perimeter. Whumpfs and remotely triggered avalanches have been studied systematically by Johnson [38, 39]. They generally involve weak layers composed of buried surface hoar, faceted grains and depth hoar.

2.2 Snowpack subsidence

The sudden subsidence of stratified snow has been mentioned in scientific publications since the 1930's (see Table 2.1). The phenomenon received various denominations: firnstoss, firn quake¹, snowpack collapse and, most simply, whumpf. In most cases the observations were fortuitous and, except in the case of Johnson [40], none of the narrators were actually prepared to record the subsidence. Instead, they report an element of surprise as they sensed the snowpack collapse under their feet or vehicles, while engaged in other work. The snow surface was observed to drop by up to several centimetres over a large area [73, 79]. The phenomenon was attributed to the collapse of a subsurface layer of loosely packed ice particles [7]. In most instances it was observed that the subsidence is not instantaneous over the area but progressing rather slowly, i.e. at 'visible' speed. Indeed, most narrators report of sensing the velocity of the collapse front: some describe it as originating from themselves and moving away, others as a passing perturbation, first approaching, then moving away. Truman [79] visually characterises the perturbation as wave-like. Bohren and Beschta [7] rule out elastic waves (longitudinal or shear waves) as carriers for collapse propagation. In the present work, the perturbation that propagates the subsidence across the snowpack will be referred to by the term *collapse wave*. Because of their irreversibility, collapse waves are per se non-linear waves.

In some cases of collapse, acoustic emissions have been reported [14, 73, 79]. The emission is usually perceived as continuous (not intermittent as is often observed in plastic deformation), and moving along with the collapse front. The sounds were qualified as 'whumpf', 'whomph', 'swishing', 'hissing', 'crashing', 'wind-like', 'train-like', 'aircraft-like' or even 'bangs'. These sounds usually last from a fraction of a second to a couple of seconds, but Truman reports hearing continuous acoustic emission for up to 10 s. Intensities range from inaudible to quite loud. In the frequency domain, the sound could possibly overlap with infrasound. In some instances no sound is sensed by the human ear but the collapse is clearly perceived by the body.

The first successful measurement of the velocity of a collapse wave in snow is credited to Johnson et al. [40]. Geophones were used to measure the arrival times of a collapse wave at an array of points, finding a propagation velocity close to 20 m/s [40]. At this time much higher fracture propagation velocities were expected, as proponents of shear models had predicted fracture

¹'Firn' indicates perennial snow, as opposed to seasonal snow. The term stems from the Swiss German 'fern', meaning 'last year'.

speeds between 100 m/s and 1000 m/s [4]. However, the order of magnitude of Johnson's result was later confirmed by van Herwijnen [83]. The data collected by Johnson are compiled in Table 2.2.

Fig. 2.1 shows an example of whumpf as it appears on the surface. The subsidence and the perimeter of the whumpf, where fracture arrested, are clearly visible. Collapsed weak layers have been documented photographically on several occasions [37, 65, 69, 83]. One of these photographical documents [37] is reprinted in the left panel of Fig. 1.2. In this instance the weak layer was composed of buried surface hoar crystals and the fracture was triggered by a skier about 10 metres away from the site where the picture was taken. The figure shows the point where fracture propagation abruptly arrested. The fracture pattern exhibits a transverse fracture through the slab up to the surface. The stratification shown in Fig. 1.2 is a somewhat remarkable example, as weak layers often are less conspicuous than this one. Other types of weak layers, such as faceted crystals and depth hoar also actively propagate fracture. An example of a depth hoar layer is shown in Fig. 2.2.

The volumetric collapse of a weak snowpack layer has been frequently observed. Van Herwijnen [83] reported volumetric collapse in twelve field experiments which involved various types of weak layers (10 layers composed of buried surface hoar, 1 of depth hoar and 1 of faceted crystals) and various triggering mechanisms (4 rutschblock tests, 3 cantilever beam tests and 5 instances of skier triggering in the slope). These results convey the message that collapse of the weak layer is not an exception but the rule in the fracture of snow.

The simultaneity of slope-parallel displacement of the slab (shear strain in the weak layer) and slope-perpendicular displacement (collapse of the weak layer) during fracture nucleation has been demonstrated by van Herwijnen and Jamieson [83]. In their experimental setup, the weak

Table 2.1: Observations of collapse waves. Minimum propagation distance d , collapse amplitude h_f , velocity c and acoustic emission (AE) of collapse waves in seasonal snow (seas.) and firns.

Observation		Snow cover	d [m]	h_f [mm]	c [m/s]	AE
Sorge	[73]	arctic firn	-	25	-	hiss-crash-hiss
Bradley	[8]	seas.	-	-	-	startling sound
Truman	[79]	seas.	-	10 – 20	6	swish
Bohren et al.	[7]	seas.	3 – 30	> 10	> 60	whomph
den Hartog	[14]	antarctic firn	8 km	perceivable	330	
Jamieson et al.	[37]	seas.	8	10	-	whumpf
Johnson	[39]	seas.	-	1 – 10	-	whumpf
Johnson et al.	[40]	seas.	12.7	2	20 ± 2	whumpf
van Herwijnen et al.	[83]	seas.	-	1 – 12	10 – 40	-

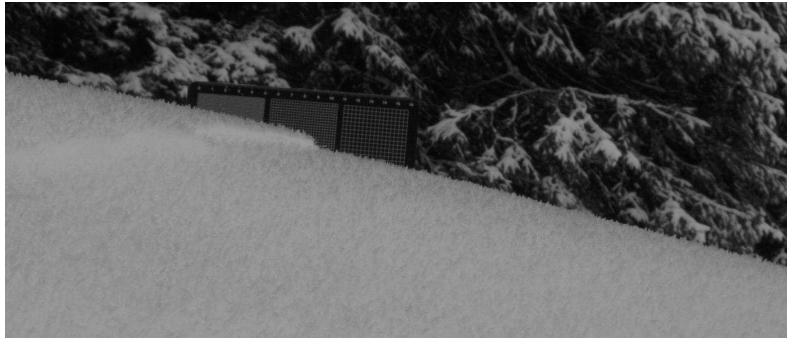


Figure 2.1: Perimeter of a whumpf, where fracture arrested. The snow surface sank by approximately 1 cm in the collapsed area on the right. This particular whumpf was triggered while digging a pit, 20 m away from where the image was taken. Photo: J. Heierli.

layer was laid open by exposing a cross-section of the snowpack. The fracture process was captured on a high-speed video camera and displacements were measured with an accuracy of 0.1 mm in space and a resolution of 4 ms in time. It was shown that slope-parallel and slope-normal displacements initiate simultaneously. Importantly, no shear-induced dilation during the nucleation phase was observed in these experiments. Van Herwijnen and Jamieson also measured fracture propagation velocities on slopes [83]. The results indicate velocities between 10 m/s and 40 m/s, thus confirming the order of magnitude obtained previously by Johnson [39]. In summary:

1. There is experimental evidence demonstrating that subsidence is not an exception but the rule in the fracture of snow [83]. Collapse amplitudes between 1 to 25 mm have been reported.
2. Collapse waves propagate with various speeds, reportedly $6 - 60 \text{ ms}^{-1}$ in fresh sea-

Table 2.2: Compilation of the characteristic properties of a whumpf in seasonal snow, after Johnson et al. [40]. The propagation velocity was measured with a string of geophones.

Notation	Description	Range	Units
h	Thickness of slab	0.40	m
ρ	Average density of slab	190	kg/m^3
ρ_{\max}	Maximum density of slab near weak layer	240	kg/m^3
h_f	Collapse amplitude at arrest	2	mm
	Age of weak layer	50	days
θ	Slope angle	0	deg
c	Propagation velocity (mean between 4.75 m to 12.70 m)	20 ± 2	m/s
d	Minimum propagated distance from trigger point	12.7	m

sonal snow [7, 40, 79]. In dense arctic firn, velocities up to about 300 ms^{-1} have been reported [14]. These figures are an order of magnitude smaller than the speed of elastic waves in the corresponding slabs.

3. Collapse waves can travel over long distances, reportedly up to 300 m in seasonal snow [39], and several miles in polar firns [14]. They can travel for a rather long time (up to 10 s in seasonal snow, [79] and more in firn). As a consequence, the collapse wave must be energetically self-sustained.
4. In some instances the transverse failure of the overlying slab can arrest the propagation of the subsidence (Fig. 1.2).
5. Acoustic emissions are often, but not always, perceived during subsidence. They appear to cover a wide spectrum of sounds, from a 'wumm' or 'whumpf' to hissing, crashing or banging sounds (Table 2.1).

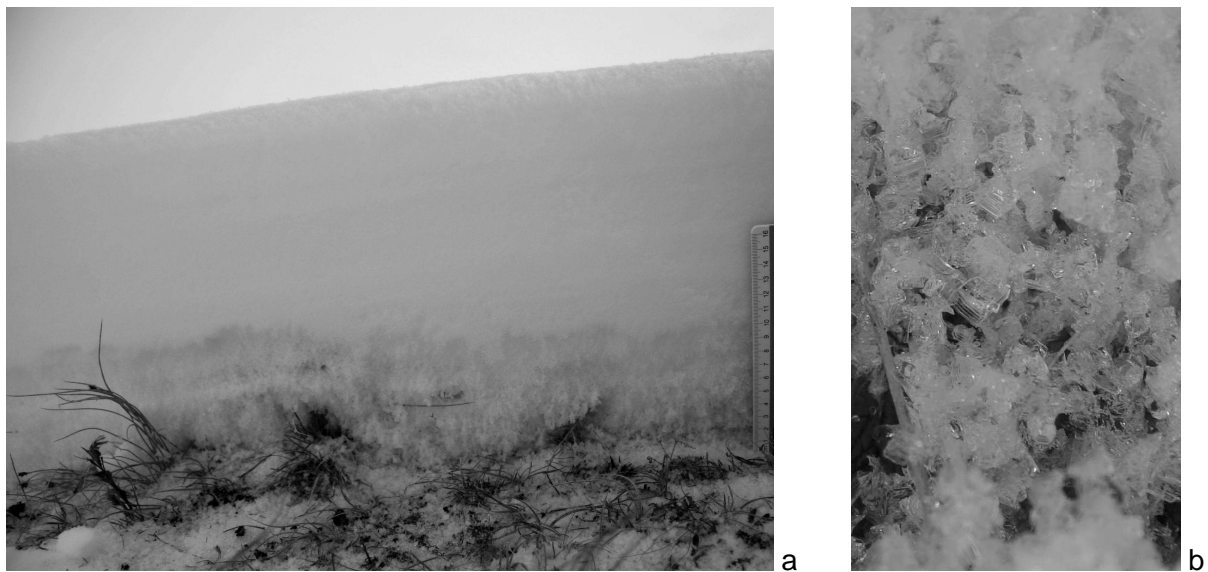


Figure 2.2: Depth hoar. **a:** Layer of depth hoar at the bottom of the snowpack (here 10 cm thick). **b:** Loosely bonded, polyhedron-shaped depth hoar grains (diameter 4 mm). The cohesion of these grains is easily disturbed by mechanical action. The geometry of the structure favours a tighter rearrangement as the bonds break. Photo: Alain Duclos, ALEA.

2.3 Specific fracture energy

A pivotal analysis of the failure behaviour of snow samples was undertaken in 2000 by Kirchner, Michot et al. [42–44]. By analysing several hundred homogeneous snow samples, they found that fracture toughness in shear is about the same as in tension [42], that there is no size dependence in their measurements of the strength of snow [44], and that the strength of snow distributes according to a Weibull distribution with extremely low modulus, reportedly between 1 and 2 for various types of snow [44]. Their work incited snow scientists to establish a database of fracture properties for natural snow. Following Kirchner and Michot's original work, several new test methods have been proposed [20, 21, 51, 68–70], including notch experiments which will be discussed in section 2.4.

In presence of elastic mismatch across an interfacial crack [15], the fracture toughness K is a complex number and the fracture energy w_f relates to K by the relation $K\overline{K} = w_f E^*$, where E^* is an adequate elastic modulus [52] and the overline denotes complex conjugation. In general, K and w_f depend on the fracture mode. Data on the fracture toughness and specific fracture energy of stratified snow failing along weak layers are still not abundant today. Measurements are available from four sources [20, 51, 68, 69]. Some relate to mode II fracture, others to mode I fracture. A compilation of measured fracture energies of weak layers without distinction of mode is shown in Fig. 2.3. The specific fracture energies of weak layers appear to fall between 0.01 and 0.1 J/m² with average 0.04 ± 0.01 J/m² [68].

The fracture energy of a weak snow layer can be compared to the gravitational potential energy available through its collapse. For a numerical example, the measurements given in Table 2.2 are considered. In that case, the available potential energy $\rho g h h_f$ is 0.75 J/m² per millimetre

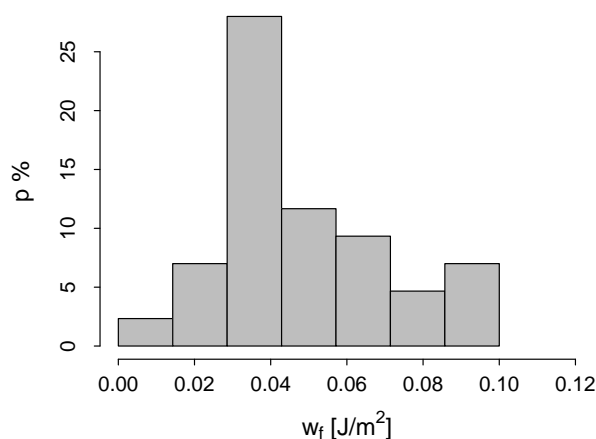


Figure 2.3: Compilation of measured fracture energies w_f , based on data from [20, 51, 68, 69].

collapse amplitude, which is significantly larger than typical fracture energies with range between 0.01 and 0.1 J/m². In the case of Johnson, who reported a collapse by a total of 2 mm, the excess is a factor fifteen at least. Some of this potential energy may not be converted into fracture energy but dissipated otherwise. However, a large amount of potential energy is, at least in principle, convertible into fracture energy. In summary:

1. Low density snow and weak layers appear to undergo brittle fracture. The failure of individual samples is most unpredictable.
2. Fracture toughness in shear is about the same as in tension for snow [42]. This is likely due to the random cohesive-granular structure of snow, in which the microscopic fracture planes are always loaded in mixed-mode.
3. The fracture energy of weak layers likely ranges from 0.01 to 0.1 J/m², with mean 0.04 J/m², but more experimental data should be collected.

2.4 Artificial triggering

At the International Snow Science Workshop in 2006, two new types of field experiments - designated as PST, 'propagation saw test' and ECT, 'extended column test'- were presented with the aim of assessing the propensities for fracture nucleation and fracture propagation in snow. These experiments were carried out in situ on stratified snow containing a weak layer. Cuboid samples were carefully isolated from the environment as shown in Fig. 2.4. In PST-type tests, Sigrist and Schweizer [69] as well as Gauthier and Jamieson [24] notched the weak layer with a snow saw. Under favourable circumstances, after saw-cutting between 10 cm and 40 cm this initiated a rapid, self-sustained propagation of fracture to the opposite end of the sample, debonding the slab on the passage. If tilted enough, the debonded slab would start to slide en bloc, like a miniature slab avalanche. Under unfavourable circumstances, the notch would either not become critical at all, or become critical but arrest after propagating a small distance. A transverse failure of the slab as shown in Fig. 1.2 is then often observed. In ECT-type tests, Simenhois and Birkeland [72] use a similar geometry but, instead of notching with a snow saw, they tap on the upper surface to induce the fracture in the weak layer. The possible outcomes of the ECT test are similar to the outcomes of the PST test. Due to the absence of pre-cracked areas, this method is very satisfactory from the point of view of nucleation, but quantitative studies seem to be difficult to model with the present specification. Using either nucleation method (PST saw cut or ECT tap), the snow specimen can be oriented in an arbitrary direction. In practice, the PST works best if the sample is oriented with the long side of the cuboid parallel to the down-slope direction. The ECT is easier to manage when the long side of the cuboid is oriented sideways, parallel to the contour line.

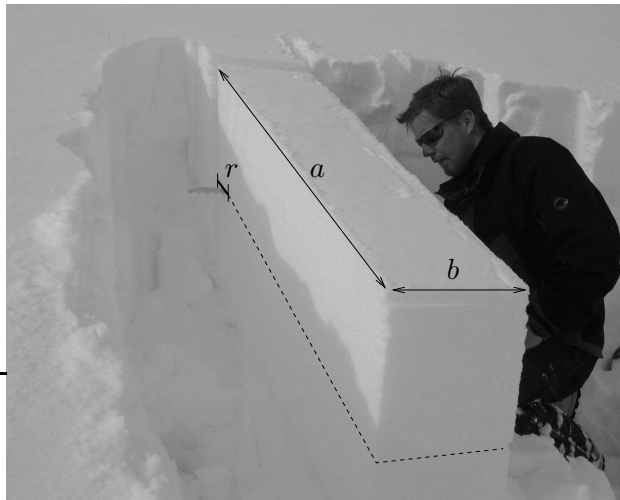


Figure 2.4: Notch experiment in field conditions, cutting into the weak layer (dashed) with a snow saw from uphill. A slightly longer cut than shown gives rise to the sudden propagation of the fracture through the entire weak layer. a : length of sample in downslope direction, b : length of sample in slope-lateral direction (parallel to contour line of terrain), r : notch length. Reprinted with permission of C. Sigrist.

Gauthier's PST experiments were intended and designed for evaluating the snowpack's propensity for fracture propagation [24], but something even more important was reported: The notch experiment worked in horizontal snow just as well as on inclined slopes. Very comparable critical notch lengths were measured for different slope angles (Table 2.3). In 23 experiments dated 24-01-2006, 17 dated 8-02-2006 and 22 dated 26-02-2006, Gauthier observes that the critical notch length depends very weakly on slope angle. Sigrist, in his experiment, laid the emphasis on obtaining a value for the energy release rate at the fulfilment of the Griffith criterion [68, 69]. This experiment is unique in the sense that all necessary parameters to describe the fracture process were measured independently. These data thus constitute an excellent test case for a theoretical model. Sigrist's results are given in Table 2.4. In summary:

1. In-situ experiments have recently been developed to study crack formation and crack propagation in snow [24, 69, 72]. Failure is triggered artificially by notching or tapping.
2. Fracture propagation takes place on slopes as well as in the horizontal snowpack. The critical notch lengths needed to trigger fracture propagation are of the order of a few decimetres, regardless of slope angle.

Table 2.3: Notch experiment results from Gauthier and Jamieson (PST). Critical notch length r_c , average slab density ρ and slab thickness h (measured slope-perpendicularly). Compiled from data published in [23, 25].

Date	Slab ρ [kg/m ³]	h [m]	Slope θ [deg]	Notch r_c [m]	Notch location
24-01-2006	134	0.11	0	0.13	-
	134	0.11	30	0.19	low end
	134	0.11	38	0.22	low end
08-02-2006	260	0.98	0	0.36	-
	233	1.29	23	0.36	top end
26-02-2006	85	0.51	0	0.07	-

Table 2.4: Notch experiment results from Sigrist and Schweizer. Critical notch length r_c , average slab density ρ , elastic modulus E and thickness h . From data published in [69].

Date	ρ [kg/m ³]	E [MPa]	h [m]	θ [deg]	w_f [J/m ²]	r_c [m]	Notch location
27-01-2006	187	7(3)	0.26	30	0.07(2)	0.23(2)	top end

2.5 Crack-face friction

An example of the action of friction forces between slab and bed surface is visible in Fig. 1.1. On the far right of the picture, half a dozen snow blocks came to a rest after moving a few metres (other arrested snow blocks are visible further behind). The slope angle at this place was approximately $26^\circ \pm 3^\circ$, with $22^\circ \pm 2^\circ$ above and $32^\circ \pm 2^\circ$ below (measured by A. Duclos on IGN maps). As the deceleration is due in large parts to the contact forces between slab and substrate (air friction is small in the initial phase of slab avalanche motion), friction angles appear to be around 26° in this case. However, as the contact surfaces are eroded by the relative motion, this does not exactly quantify the initial crack-face friction during crack propagation.

In-situ measurements of crack-face friction are not available at present, but a comprehensive study of dynamic friction of snow has been performed by Casassa, Narita and Maeno [11] who used shear box experiments to measure frictional forces of snow-snow contacts in the laboratory. Results are related in terms of a total friction coefficient μ defined as $\mu = \tau_T / \sigma$, where τ_T is the total friction force per unit area and σ is the normal stress across the contact faces. The relative speed between contact faces in the shear box was varied between 1 m/s and 25 m/s. In the context of slab avalanche release, measurements for small speeds are of particular interest. For snow-snow friction between solid blocks Casassa et al. obtain $\mu \geq 0.4$ [11]. Compatible results were obtained by sliding blocks over slopes, where μ was found to range between 0.45

and 0.65 with average 0.58 [10]. Similar values of μ have been reported by Fyffe [20] who measured $\mu = 0.4$ to 0.5. Fyffe estimated crack-face friction coefficients to take values between 0.4 and 0.7. Attempts to distinguish the contributions of Coulomb friction $\mu_c \sigma$ and adhesion a , where $\mu_c \sigma + a = \mu \sigma$, resulted in small values of a , and sometimes questionable negative values [11]. Until the role of adhesion is clarified in snow-snow contacts, $\mu \approx \mu_c$ will be assumed for the present purpose. In summary:

1. Friction coefficients between snow blocks in low-speed contact (about 1 m/s) appear to take values above 0.4, and perhaps as high as 0.7. Corresponding friction angles $\theta_\mu = \arctan \mu$ are then above $\geq 22^\circ$, and perhaps as high as 35° .
2. Crack-face friction cannot in general be neglected in avalanche formation models.

2.6 Young's modulus of snow

Material properties for various types of snow are compiled in Appendix A. Amongst these, estimates of the Young's modulus or elastic modulus E are subject to large scatter due to various types of grains, aggregate structure, bulk density and temperature. E is generally modelled as a function of bulk density ρ , regardless of structural parameters. A first compilation of elastic moduli was given by Mellor [57] in 1975. Recent studies are due to Shapiro [67], Frolov and Fedyukin [19], Schweizer and Camponovo [66], Takei and Maeno [77] and Sigrist [68]. The models proposed by these authors can lead to very different estimates of the elastic modulus of a sample.

An extensive experimental study is due to Scapozza [63] who measured the elastic modulus of 200 homogeneous field samples under various conditions. The samples consisted of fine-grained, rounded snow, typical of slab snow. Temperatures ranged from -19°C to -1.8°C . The measurements were based on uni-axial compression tests with imposed strain. The strain rates were varied between 10^{-6} and $2 \times 10^{-3} \text{ s}^{-1}$. Scapozza's empirical model for Young's modulus is obtained by linear regression of $\ln E$ and ρ , leading to:

$$\hat{E} = E_0 \exp(\rho/\rho_0) \quad \text{with } E_0 = 0.2 \text{ MPa}, \quad \rho_0 = 67 \text{ kg/m}^3,$$

where \hat{E} stands for the model estimate of E . Scapozza found that the residuals $E - \hat{E}$ follow no identifiable pattern in temperature or strain rate and that his estimate of E is independent of temperature and strain rate in the tested range. Some calculations in the present work depend on estimating the value of Young's modulus, as this property cannot usually be measured under field conditions. Until a precise model for Young's modulus for snow emerges, Scapozza's model is consistently used in the present work to evaluate Young's modulus when no independently measured value is provided in the sources.

Chapter 3

Review of avalanche release models

In this chapter, current theories of snow avalanche release are reviewed and confronted with both the phenomenology and the experiments presented in the previous chapter. Snow slope failure has traditionally been described in terms of a 'snow stability index' [13,60]. In this approach, failure is associated with a homogeneous response to loading throughout the entire material: no local stress concentrations are considered and each volume element is supposed to carry an equal load. A sample is expected to fail when loaded to a critical level of stress, the "strength of the material". The obvious advantage of this approach is its simplicity. The obvious problem is that nature very much tends to localise damage, rather than to spread it homogeneously across a material. The inadequacy of this approach called for methods based on sound physical principles and the problem of snow failure was approached by the methods of fracture mechanics and statistical physics. In those, strength is associated with the actual physical sample, which is considered inhomogeneous in some places. The inhomogeneities are regarded as discontinuities (flaws or cracks), around which stress concentrations develop and fracture may take place. The sample is expected to fail according to the specific configuration of discontinuities it contains. Fracture mechanics regards the existence of cracks as given, and studies their growth. Statistical physics avoids the concept of pre-cracked areas altogether. Instead, failure is envisaged as a localisation and/or accumulation of damage in the material [86].

The two most recent reviews on snow avalanche formation [64, 65] sum up the state of knowledge reflected by the current models. Since these reviews were written, however, new experimental results [25, 40, 69] and a new theoretical approach to the failure of stratified snow [30,32,33] have put a question mark on the general validity of the current models. The new approach explores the role played by porosity and volumetric collapse in the fracture process.

In the following discussion, if not stated otherwise, elastic deformation is considered as plane strain. The bulk material is homogeneous with density ρ , plane-strain Young's modulus E and Poisson's ratio ν . The acceleration of gravity is denoted by g .

3.1 Simple shear models

The release of slab avalanches is commonly related to the simple shear fracture of a weak subsurface layer [4, 5, 12, 22, 50, 53–55, 75, 86]. The simple shear model goes back to McClung [53] and was originally developed by Palmer and Rice for over-consolidated clay [59]. The model has never been validated for snow avalanches [64]. Validation was regarded as "difficult, maybe even impossible" [64]. Despite this setback, the simple shear model inspired a considerable amount of theoretical work dealing with various aspects of shear failure.

3.1.1 Short cracks

Louchet and Faillettaz [50] consider the case of an incipient crack in a subsurface layer of weak snow. The half-length r of the crack is small with respect to its depth h under the surface (Fig. 3.1). Physically, the crack is considered to be a planar slip surface of zero thickness in the weak layer plane. The strata of snow above and below the weak layer are assumed to have identical elastic properties. In absence of a crack, the weak layer is loaded by gravity with a uniform shear stress $\tau = \rho gh \sin \theta$, where θ is the slope angle. Within the crack, tangential contact forces between the crack faces reduce the loading stress by an amount τ_r . The other components of the stress tensor remain balanced within the crack. Therefore the crack is loaded in mode II (one of the two cases of simple shear). It is further assumed that the crack can grow in the weak layer but cannot kink out into the surrounding layers. As a direct application of the Griffith criterion [27], Louchet and Faillettaz find the following expression for the critical crack length:

$$r_c = \frac{1}{\pi} \frac{w_f E}{(\tau - \tau_r)^2}, \quad (3.1)$$

where w_f is the specific fracture energy required to separate a unit area of weak layer. Louchet and Faillettaz actually derived this equation for $\tau_r = 0$, but the generalisation is straightforward. The crack is unstable if and only if its half-length r exceeds the critical length r_c . Eq. 3.1 holds

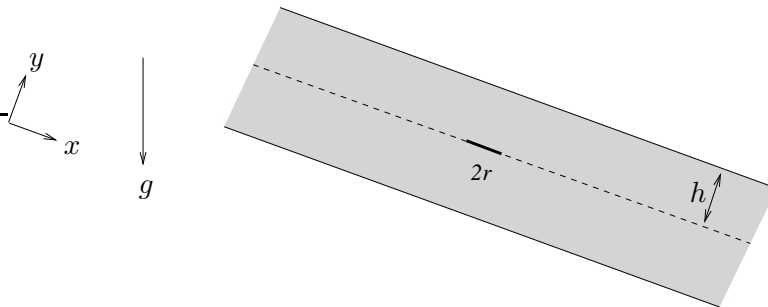


Figure 3.1: A short crack in a weak layer embedded between layers with identical elastic properties.

for $r \ll h$ and can be used as a condition for a stable flaw to turn unstable. The asymptotic behaviour of the critical length in Eq. 3.1 is $r_c \sim (\tau - \tau_r)^{-2}$ for $\tau > \tau_r$. For $\tau = \tau_r$, a critical length r_c does not exist. Assuming Coulomb friction with coefficient μ between crack faces (section 2.5), a friction angle $\theta_\mu = \arctan(\mu)$ can be defined. The asymptotic behaviour of r_c can then be reformulated in terms of slope angle and friction angle. Using that $\tau - \tau_r \propto \sin \theta - \mu \cos \theta$ if $\theta > \theta_\mu$ and zero otherwise, and expanding r_c around $\theta = \theta_\mu$ in a Laurent series, it is easy to show that $r_c \sim (\theta - \theta_\mu)^{-2}$ for $\theta > \theta_\mu$ and $r_c \rightarrow \infty$ for $\theta \leq \theta_\mu$. Physically speaking, on slopes inclined less than the friction angle, a short slip surface cannot grow. On steeper slopes it can, but it is increasingly difficult to satisfy the criterion $r \geq r_c$ the closer the slope angle approaches the friction angle. Summing up:

1. The critical length of short simple shear cracks between strata with similar elastic properties is given by Eq. 3.1. Cracks can grow if their half-length r is larger than the critical r_c determined by this equation, provided that $r_c \ll h$.
2. On slopes steeper than the friction angle, the critical length of a short shear crack goes asymptotically as $r_c \sim (\theta - \theta_\mu)^{-2}$. On slopes inclined less than the friction angle, the simple shear crack cannot propagate.

3.1.2 Long cracks

McClung applied the classical Palmer-Rice model for the growth of slip surfaces in over-consolidated clay to the formation of dry slab avalanches [53]. The Palmer-Rice model [59] expresses the condition for a slip surface or cohesive mode II crack to expand into a homogeneous and elastic material.

In the Palmer-Rice model, a planar slip surface of characteristic length r is located at depth h below the surface and assumed (for an unspecified reason) to grow only in its own plane (see Fig 3.2). The slip amplitude in x -direction is denoted by δ and is a function of x . Shear stress is transmitted across the slip surface (from one face to the other) according to a known, strain-softening stress-displacement relation $\tau(\delta)$. This relation is assumed to decrease monotonically for $\delta \gtrsim 0$ and to converge to a constant τ_r when $\delta \rightarrow +\infty$ (residual friction). The energy required to separate a unit area of incipient slip surface is then $\int [\tau(\delta) - \tau_r] d\delta$, and is denoted by w_f . The faces of the slip surface are considered to be and to remain in contact all the time. Furthermore, straining and displacements in the material below the slip surface are neglected [59]. The deformation of the material above the slip surface is assumed to be one-dimensional in x -direction and the same across the thickness of the slab. The latter is a reasonable assumption for $r \gg h$. In this case, the two topologies shown in Fig. 3.2 a and b are energetically identical up to a factor of two.

In snow the situation is somewhat different as the slip surface evolves in a pre-existing weak layer sandwiched between younger strata on top and older strata below (Fig. 3.3). The presence

of the weak layer gives a good reason for the slip surface to grow in its own plane. The different qualities of the strata on either side lead, in principle, to the necessity of taking into account elastic mismatch. This is avoided by assuming similar material properties for these strata. The remaining assumptions required to apply the Palmer-Rice model were regarded by McClung as suitable for snow and inherited. In particular, the assumption that the slab displaces only in x -direction seemed acceptable to McClung, although it meant that any subsidence (positive or negative) during the course of fracture had to be ignored. Under these restrictions, the Palmer-Rice model is applicable. For the case of a linear-elastic material, the following expression for the critical crack length is obtained [53]:

$$r_c^2 = 2h \frac{w_f E}{(\tau - \tau_T)^2}, \quad (3.2)$$

where $\tau = \rho g h \sin \theta$. At the critical crack length r_c , crack-driving forces and crack-resistance forces are just balanced. If the slip surface is longer than r_c , its growth is energetically favourable. In snow, values for r_c computed with Eq. 3.2 are typically 1 metre to a few metres [4, 20, 64, 75], depending mostly on the amount of crack-face friction. According to the model, a pre-existing shear crack of size r , initially sub-critical ($r < r_c$), can become critical by the increase of τ during precipitation, which may decrease r_c until $r > r_c$, resulting in a direct action avalanche (occurring during snowfall). For delayed action avalanches (occurring after snowfall), a mechanism of slow growth of sub-critical, persistent shear cracks has been invoked, but it has not been made clear where the energy for this process could come from (as long as $r < r_c$ energy is demanded for growth), nor how the process might be initiated.

The crucial problems for the simple shear model are that (i) it does not account for the subsidence of the slab which is often observed and (ii) it does not explain the fracture of weak

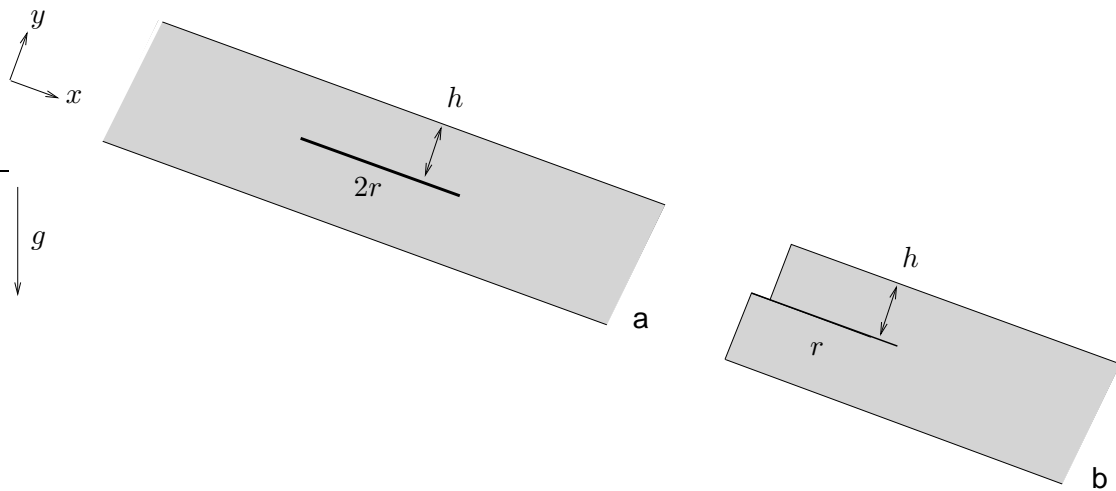


Figure 3.2: The Palmer Rice model considers the formation and propagation of a slip surface in a homogeneous material. **a.** Embedded slip surface. **b.** Step in a slope.

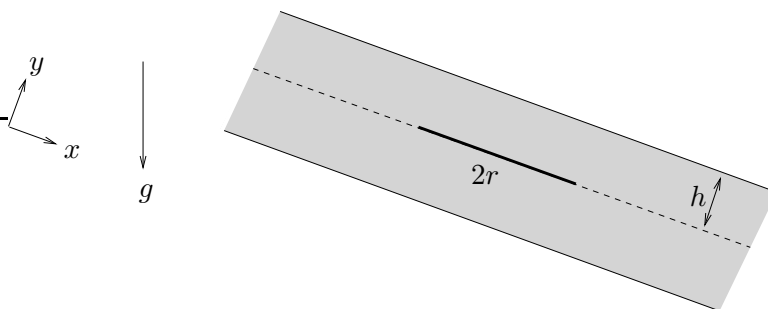


Figure 3.3: McClung's model considers a long shear band, slip surface or shear crack ($r \gg h$) in a weak layer embedded between two layers with identical elastic properties.

layers in horizontally stratified snow. The asymptotic behaviour of the critical length in Eq. 3.2 is $r_c \sim (\tau - \tau_r)^{-1}$ for $\tau > \tau_r$. As previously, a critical length r_c does not exist when $\tau = \tau_r$. Using the same argument as before, the asymptotic behaviour of r_c can be reformulated in terms of slope angle minus friction angle: $r_c \sim (\theta - \theta_\mu)^{-1}$ for $\theta > \theta_\mu$, and r_c does not exist for $\theta \leq \theta_\mu$. Physically speaking, the result is still the same as in section 3.1.1: on slopes inclined less than the friction angle, a long slip surface cannot grow. On steeper slopes it can, but again the criterion $r \geq r_c$ is increasingly difficult to satisfy the closer the slope angle approaches the friction angle, as r_c grows out of bounds (the only difference being a divergence with exponent of -1 instead of -2). This conflicts with observations. The experiments discussed in section 2.4 have shown that it is about as easy to form a critical crack in a horizontal stratification as in a 40° slope: critical lengths are about the same. This very much suggests that the shear model neglects some relevant energy contribution which is convertible into fracture energy.

Another important implication follows from the shear model. A simple shear crack can grow if and only if $\tau > \tau_r$, as Eq. 3.2 shows. Wherever the residual forces match the gravitational load, $\tau - \tau_r = 0$ and the crack cannot become critical. Instabilities such as whumpfs, which involve no or if any, very limited slope-parallel motion, are thus very difficult to understand within the simple shear model. For the same reason, remotely triggered avalanches cannot be explained, for the entire portion of slab which was undercut by the shear crack necessarily slips and is expected to participate in the release.

The simple shear model Eq. 3.2 was updated by Bazant, Zi and McClung [5] by applying an 'effective crack size' correction c_f , which simply replaces r_c in Eq. 3.2 by $r_c + c_f$:

$$(r_c + c_f)^2 = 2h \frac{w_f E}{(\tau - \tau_r)^2}. \quad (3.3)$$

The term c_f is assumed to be a positive constant of about half the size of the zone where plastic flow occurs. The intention of this correction is to deal with non-linear, elastic-plastic effects in the crack tip zone [76]. However, all previous statements regarding Eq. 3.2 apply for the updated model, as r_c is only shifted by a constant. The essential problems of the shear model are thus

not addressed by the 'effective crack size' correction. In summary:

1. On slopes steeper than the friction angle, the critical length of a long shear crack goes asymptotically as $r_c \sim (\theta - \theta_\mu)^{-1}$. On slopes inclined less than the friction angle, the simple shear crack cannot propagate.
2. The simple shear model conflicts with the observation that fracture propagates across horizontally stratified snow and does not take into account the subsidence of the slab. Remotely triggered avalanches are difficult to understand within the simple shear model.

3.1.3 Long cracks in a brittle weak layer of finite thickness

Chiaia, Cornetti and Frigo [12] consider a weak layer of finite thickness. The weak layer's thickness is h_w and its shear modulus G_w . Like McClung, they consider a mode II situation in which the displacement $u_x(x)$ of the slab is parallel to the x -direction and uniform across the thickness. Assuming a long crack and a brittle weak layer, the stress-displacement relation is linear until the weak layer instantaneously fails, and constant afterwards, i.e. $\tau(x) = (G_w/h_w)u_x(x)$ until failure and $\tau(x) = \tau_r$ after failure¹. Based on these assumptions, Chiaia, Cornetti and Frigo find that the original form of McClung's criterion Eq. 3.2 can be maintained if the critical length r_c is replaced by $r_c + \psi$, where $\psi = (Eh_w h_w / G_w)^{1/2}$,

$$(r_c + \psi)^2 = 2h \frac{w_f E}{(\tau - \tau_r)^2}. \quad (3.4)$$

This equation has the same form as Bazant, Zi and McClung's effective crack size correction Eq. 3.3, but the roles of c_f and ψ are different. Here ψ relates to the relaxation of elastic strain in the slab ahead of the crack tips, while c_f relates to the size of the fracture process zone, where irreversible changes take place. It should be emphasised that, assuming brittle fracture, Eq. 3.4 is an exact analytical result, while the 'effective crack size' correction is an *ad hoc* assumption. In summary:

1. Taking into account the finite thickness of the weak layer and assuming it brittle, the critical length of a shear crack is reduced by an amount given by ψ . Within the assumptions, this result is exact.
2. Eq. 3.4 takes the same analytical form as an 'effective crack size' correction. The essential problems of the shear model (subsidence of the slab and fracture propagation in the horizontal) are not addressed.

¹The model is actually derived for $\tau_r = 0$, but the generalisation is straightforward.

3.1.4 Formation energy for shear cracks

A more general viewpoint can be taken by expressing Eqs. 3.1 to 3.4 as saddle points of a crack energy function $V(r)$ valid for cracks of any length. For the crack energy to correspond to a formation energy, $V(0) = 0$ must be imposed. It is easily shown that the following three expressions for crack energy (taken in this order) reproduce Eqs. 3.1, 3.2 and 3.4 by demanding $\partial_r V(r) = 0$,

$$V(r) = 2w_f r - \frac{(\tau - \tau_r)^2}{E} \pi r^2, \quad r \ll h, \quad (3.5)$$

$$V(r) = 2w_f r - \frac{(\tau - \tau_r)^2}{3Eh} r^3, \quad r \gg h, \quad (3.6)$$

$$V(r) = 2w_f r - \frac{(\tau - \tau_r)^2}{3Eh} [(r + \psi)^3 - \psi^3], \quad r \gg h. \quad (3.7)$$

Later in chapter 4 the advantages of taking this viewpoint will become more evident.

3.2 Collapse models

The collapse approach towards weak layer fracture emerged prior to the shear fracture approach, but was not developed for decades. Reports of subsidence can be found as early as 1930 [73]. Truman very clearly described the physical properties of collapse waves in seasonal snow in 1973 [79]. Bohren and Beschta proposed in 1974 that the collapse of a prevalent, structurally weak subsurface layer characterised by weak inter-granular bonding was the cause of the observed collapse waves [7]. Lackinger thought that the bending associated with the collapse wave would generate transverse fractures of the type shown in Fig. 1.2, reducing the circumferential support of a slab undercut by fracture [46].

3.2.1 The flexural wave model

In the 1999/2000 winter, Johnson et al. measured in situ the propagation velocity of a collapse wave by means of geophones spread out in the snowpack [38, 40]. A collapse amplitude of about 2 mm and a velocity of 20 ± 2 m/s were measured (see section 2.2). The collapse wave had spread over flat ground and it was therefore straightforward to estimate the gravitational potential energy released during the event. Johnson came up with about 1 J/m² [39]. On the other hand, the fracture energy of the buried surface hoar that had collapsed during the event was estimated between 10^{-2} and 10^{-1} J/m², a small amount in comparison [39]. Therefore, even if only a small amount of the gravitational potential energy released by collapse were convertible to fracture energy, a new understanding of fracture in snow would be necessary, as shear fracture models do not account for this process.

On a conceptual level, Johnson detailed the fracture process as follows: The very first event of the failure process is the local collapse of a portion of weak layer. As a consequence, the support of the overlying slab is lost and the slab bends, increasing the shear strain in the still intact weak layer at the edge of the collapsed zone. Accordingly the weak layer fractures in shear and the collapse is translated outwards, progressively fracturing the weak layer further and further, resulting in a bending wave (Fig. 3.4). The shear fracture of the weak layer is coupled with the propagation of the bending wave, which is modelled as a linear flexural wave propagating through a free, unsupported slab [39].

With hindsight, this is a remarkable intuitive description of the collapse process, except for two elements: Firstly, it is unnecessary to insist on the fracture in shear of the weak layer. Energetically only the microscopical fracture mode matters, which is in mixed-mode due to the random assemblage of the weak layer. The load increase on the intact weak layer is in any case both in shear and in compression. Secondly, the interpretation of the bending wave as a linear flexural wave in a free beam [39] is inadequate for describing a collapse process. Flexural waves result from a linear differential equation, describing a process that leaves a state of equilibrium and returns to the same state of equilibrium. Consequently and paradoxically, the actions of gravity and irreversibility -both essential- were cast aside in Johnson's model calculations [39]. In summary:

1. If a small amount of the gravitational potential energy freed by collapse is convertible to fracture energy, a new understanding of fracture in snow is necessary.
2. The collapse wave should not be confused with a linear-elastic flexural wave, which is an inappropriate approach to a inherently non-linear problem.

3.2.2 The solitary wave model

Based on Johnson's experimental results [40] and the inadequacy of flexural waves to describe the phenomenon, Heierli [30] proposed an analytical model for fracture propagation in horizontally stratified snow under steady-state conditions. The model treats the propagating collapse wave as a non-linear wave in form of a kink-shaped solitary wave (see Fig. 3.4). The main difference with the previous, flexural wave approach is that the non-linear wave describes a transition from one metastable state of equilibrium to another state of equilibrium of lower energy. The most prominent assumption of the model is that the displacement of the slab at the crack front obeys free fall motion. The main results consist of simple expressions for the propagation speed and the wavelength of a collapse wave in snow

$$c^4 = \frac{g}{2h_f} \frac{D}{\rho h}, \quad l^4 = \gamma^4 \frac{2h_f}{g} \frac{D}{\rho h}, \quad \gamma \cong 2.331, \quad (3.8)$$

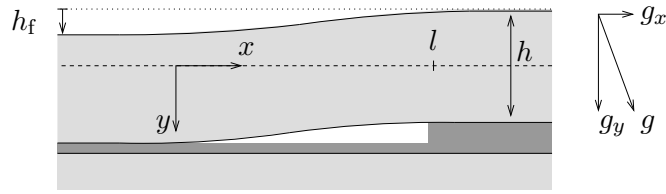


Figure 3.4: The collapse wave propagates the fracture front in horizontal terrain by gaining gravitational potential energy through subsidence. After Johnson [39].

where l is the total wavelength of the disturbance (the total length between loss of support and recovery of support), and c is the propagation velocity of the disturbance. D is the flexural rigidity of the slab. In plane strain $D = Eh^3/12$, where E is the plane strain Young's modulus of the slab material, ρ and h are the density and thickness of the slab respectively. h_f and g represent the collapse amplitude and the acceleration of gravity. The two relations in Eq. 3.8 can be put into the equivalent form:

$$\frac{1}{\gamma^2} (lc)^2 = \frac{D}{\rho h}, \quad \frac{1}{\gamma^2} \left(\frac{l}{c}\right)^2 = \frac{2h_f}{g}. \quad (3.9)$$

This model was applied to whumpfs and firm quakes and the order of magnitude of the observed propagation velocities was reasonably reproduced. However, there are limitations to the model. Firstly, there is no physical solution of Eq. 3.9 for $c = 0$. Therefore the limit of the static problem is not contained in the model. Secondly, the model does not take into account the limiting velocities of shear and pressure waves in the slab. These problems will be addressed later in chapter 5.

The non-linearity of the model resides in the boundary conditions at the crack front and at touch-down (Eq. 5 in [30]). This becomes apparent if this equation is written in a form valid in the entire space accessible to the disturbance: $(D/\rho h) \partial_{x'}^4 u(x') + c^2 \partial_{x'}^2 u(x') + g \vartheta(\partial_{x'} u(x')) = 0$, where $x' = x - ct$ and ϑ stands for the unit step function $\vartheta(x) = 1$ if $x > 0$ and 0 if not. The ϑ -function introduces a strongly non-linear effect on u , which is localised in two narrow zones at the front and at the end of the kink wave. Summing up:

1. The solitary wave model of the collapse wave results in an energetically self-sustained perturbation and therefore propagation is not limited by the energy initially available during trigger action, but unlimited in principle.
2. A combination of properties of slab and weak layer determines the wavelength and propagation velocity. The velocities reasonably match measured propagation velocities and wavelengths of collapse waves.

3.2.3 Nucleation of collapse waves

Because the solitary wave model does not contain the static limit $c \rightarrow 0$, the next obvious step is the application of the concept of weak layer collapse to the nucleation of a collapse wave (Fig. 3.5). Heierli and Zaiser [32] proposed a simple model for horizontal snow and shallow weak layers. The underlying idea is that the collapse of the weak layer frees potential energy that contributes to the propagation of fracture, by a term which is not accounted for by the simple shear model and originates in the subsidence of the unsupported slab. The model proposes to calculate the energy barrier for crack propagation by finding the saddle point in the crack energy function $V(r)$. Modelling the strain in the deformed slab in terms of the Euler-Bernoulli beam equation, the following crack energy is obtained:

$$V(r) \cong \begin{cases} 2w_f r + \frac{8}{15} \sigma h_f l_0 \left(\frac{r}{l_0}\right)^5, & h \ll r < l_0, \\ 2(w_f + \sigma h_f)(r - l_0) + V_0, & r \geq l_0, \end{cases} \quad (3.10)$$

where $\sigma = -\rho h g$ is the compressive (thus negative) stress acting on the undisturbed weak layer and l_0 is the crack half-length at which the slab makes contact with the substrate. It is given by $l_0^4 = 2Eh^3 h_f / |\sigma|$. The term V_0 simply ensures continuity of the crack energy function at $r = l_0$. A first condition for propagation arises from the requirement that the energy function decreases beyond the saddle point at r_c , i.e. $\partial_r V(r) < 0, \forall r > r_c$. This leads to a necessary condition for self-sustained propagation [32],

$$w_f \leq -\sigma h_f. \quad (3.11)$$

Note that the work per unit area σh_f is negative, so that the right-hand side of Eq. 3.11 is positive. Eq. 3.11 expresses that more energy must be released by collapse than is required for fracture propagation. Otherwise, a saddle point does not exist. Provided that this condition is fulfilled, the energy barrier for the nucleation of a propagating crack can be expressed as

$$r_c^4 = \frac{3}{4} \frac{w_f}{|\sigma| h_f} l_0^4, \quad V_c = \frac{8}{5} w_f r_c. \quad (3.12)$$

Any perturbation must overcome this energy barrier to initiate a propagating crack. In summary:

1. This model outlines the basic ideas and methods by which the problem of fracture nucleation in collapsible snowpack layers can be approached.
2. The basic ideas are presented in the simplest possible setting of a shallow weak layer in horizontal terrain. Mathematical difficulties arising from a complete and accurate analytical treatment are thus avoided. This work was the foundation of the further investigations presented here.

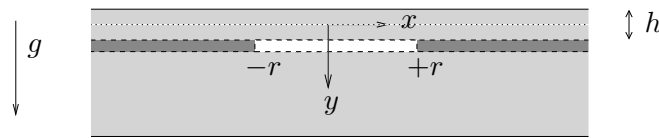


Figure 3.5: The volumetric collapse of a portion of weak layer implies loss of support for the overlying slab, which bends (not shown) and increases the strain on the crack tips.

3.3 Statistical physics approach

Following a line of reasoning that is entirely different from fracture mechanics, Louchet and Faillettaz suggested that slab avalanche release may be a manifestation of a critical phenomenon related to the failure of a multi-cracked weak layer. The statement is based upon statistical field data that indicate a power-law distribution of the measured size of the release zone of slab avalanches, above a certain lower cut-off size [17, 50]. A partially scale-invariant frequency distribution is not incompatible with a critical phenomenon as a cause of slab failure, but no proof for it either. If slab failure were indeed a critical phenomenon, the idea of the nucleation of a single critical crack and subsequent propagation of fracture would be meaningless. It would have to be replaced by an accumulation of many coalescing damage areas, which at some point becomes a random fractal set.

Multiple cracking as a cause for slab avalanche release was investigated by Zaiser and Fyffe [21, 22, 86]. In their model, slab avalanche formation is viewed as global failure of a weak layer of random local strength. The fracture-mechanical concept of pre-cracked areas is abandoned. Instead, the weak layer is modelled as a lattice in which each site is assigned a random, Weibull-distributed strength, independent of all other sites. The system is controlled by a slow increase of loading. Failure is envisaged as an accumulation of damage in terms of failed sites. The model is designed to understand the nucleation of failure by uniformly overloading the weak layer. It is implemented as a cellular automaton in which, as in the classical models of avalanche formation, the loading of the weak layer is assumed to be purely in shear.

Investigation of the computer simulation prior to global failure suggests that slab release is not related to a critical phenomenon, but to a first-order transition. In general, the spatial pattern of failed sites does not show sharp line-like or surface-like clusters interpretable as classical cracks (classical in the sense of the fracture mechanical concept of a crack). Instead it becomes a distributed set of failed sites, which altogether are not connected, but appear as many clusters of irregular size and spacing. At small scales, up to a characteristic length, the pattern of failed sites looks scale-invariant, but above the characteristic length it is no more (the autocorrelation function of damaged sites is a power-law below the characteristic length and tends in average towards a constant above). Consequently there is a typical largest damage cluster which acts in a similar manner as the critical crack of fracture mechanics.

Chapter 4

Anticrack nucleation

In this chapter a model of slab avalanche release is developed¹. The model describes the failure of a weak snowpack layer subjected to compression and shear and takes into account the volume change of the weak layer undergoing failure. The model also takes into account that the volume reduction is limited: The volume cannot reduce further when the densest (accessible) packing order of the weak layer debris is reached. Physical examples of weak layers with such behaviour were shown in Figs. 1.2 and 2.2.

4.1 Energy of formation of a mixed-mode anticrack

Consider the situation shown in Fig. 4.1. The collapsible layer (weak layer) in the snowpack is embedded between an elastic surface layer (the slab) and a rigid basal layer (the substrate). The coordinate system \mathcal{C} is chosen with the x -axis on the centre-line of the slab, pointing in downhill direction. The y -axis points into the slope and passes through the crack centre (\mathcal{C} is shown translated on the figure for clarity). The system is assumed to deform in plane strain relative to the z -direction. All extensive quantities are therefore given per unit length in z . The slope angle, measured from the horizontal to the x -axis is denoted by θ .

Due to the weight of the overlying slab, the weak layer is initially loaded both in compression and in shear. Within the weak layer a crack of length $2r$ is assumed. The crack consists of crumbled material that occupies less volume than the intact weak layer. As a consequence, the material surrounding the crack is pushed into the unoccupied space, resulting in inward displacement of the crack boundary, inverse to a mode I situation. Additionally, under shear, there is a parallel displacement of one crack face relative to the other, characteristic of a mode II situation. Due to the combination of inverse mode I and mode II loading, one speaks of a mixed-mode anticrack, or simply anticrack, implicitly including the presence of both modes [18].

The slab of thickness h is homogeneous with density ϱ , plane-strain Young's modulus E , shear

¹The model presented in this chapter has been introduced in [31].

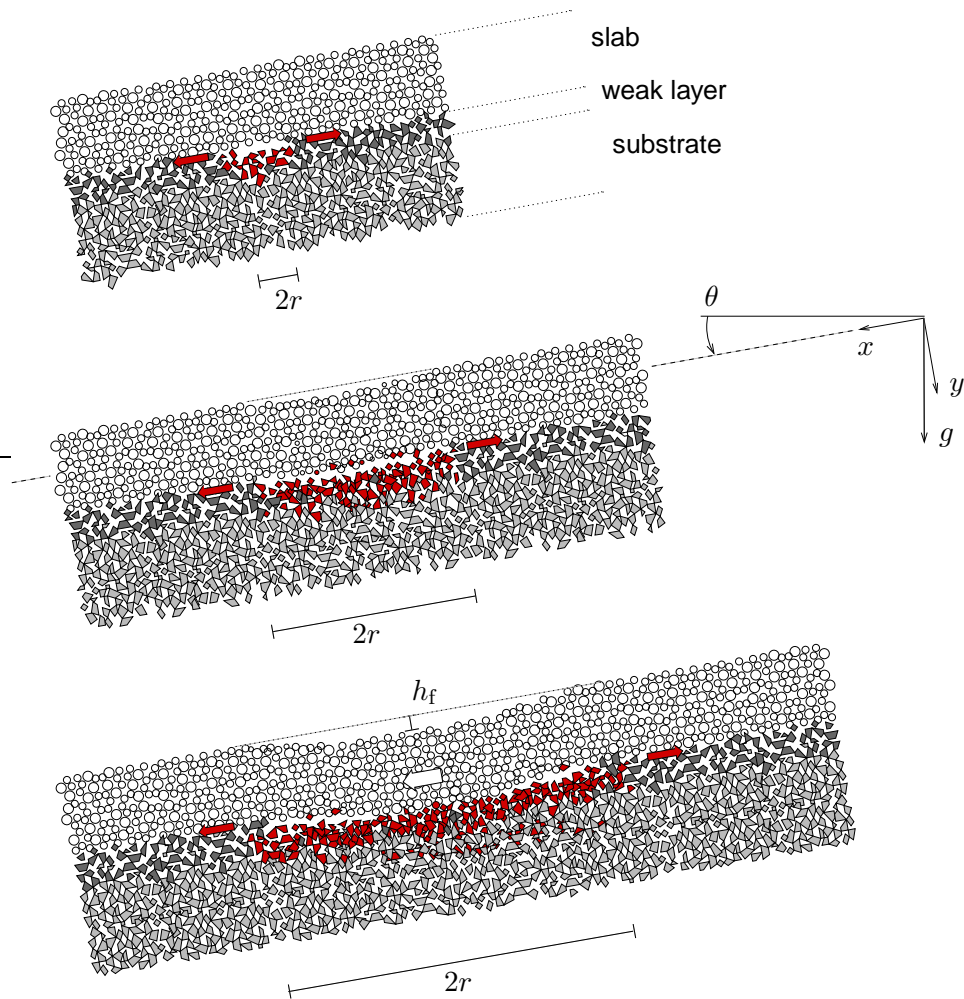


Figure 4.1: Mixed-mode anticrack in a weak subsurface layer. **a**: Anticrack nucleus of small length in comparison with slab thickness and substrate thickness. **b**: Anticrack with free, non-contacting faces. **c**: Anticrack with partly contacting faces. The slab may or may not slip (white arrow), depending on the amount of friction between slab and substrate. Legend: spherical grains: slab material; polyhedral grains: weak layer/substrate (faceted grains, depth hoar); red: collapsed debris.

modulus G , and Poisson's ratio ν . The plane strain Young's modulus is obtained by dividing the bulk elastic modulus by $1 - \nu^2$. The load acting on the undisturbed weak layer is composed of a compressive (negative) stress $\sigma = -\rho gh \cos \theta$ and a shear stress $\tau = \rho gh \sin \theta$, where g is the acceleration of gravity. The volume loss reduces the thickness of the weak layer by h_f . As a consequence, the slab experiences both slope-parallel and slope-perpendicular displacements, u_x and u_y respectively. As the crack expands and reaches a certain size, denoted by $r = l_0$,

contact between the opposing faces is established at a single point where $u_y = h_f$. This event is referred to as *tangency* (Fig. 4.2a). As the crack expands beyond $r = l_0$, the contact locus becomes an interval centered around $x = 0$. The positions on the x -axis of the two dividing points are denoted by \tilde{r} and $-\tilde{r}$ (Fig. 4.2b). Deformation is then constrained by contact forces. The slope parallel contact forces are modelled as Coulomb friction $\tau_T = \min(|\tau|, \mu|\sigma|)$ in $[-\tilde{r}, \tilde{r}]$ and $\tau_T = 0$ in $[-r, -\tilde{r}] \cup [\tilde{r}, r]$. The slope-normal contact forces are modelled as rigid confinement in y -direction:

$$u_y(x) \leq h_f. \quad (4.1)$$

The purpose is now to compute the energy of formation of a crack of arbitrary size r . To this end, the crack energy $V(r)$ is partitioned into fracture energy and mechanical energy [47]:

$$V(r) = V_f(r) + V_m(r), \quad (4.2)$$

where $V_f(r)$ is the fracture energy that must be expended to destroy cohesion along the crack faces. For a crack of length $2r$, $V_f(r) = 2w_f r$ where w_f is the specific fracture energy per unit crack surface. For a notch of length r , $V_f(r) = w_f r$. The mechanical energy $V_m(r)$ comprises changes in strain energy and gravitational potential energy of the slab. The contributions from the weak layer and the substrate are neglected as both are considered rigid for the time being. In the remainder of this section the aim is to evaluate the mechanical energy in the three situations shown in Fig. 4.1.

For anticrack nuclei of length significantly smaller than h (Fig. 4.1a), the problem is analogous to the opening of an interface crack between remotely stressed semi-infinite elastic blocks as considered by Hutchinson and Suo [35]. One difference is that the tensile stress is replaced by the compressive stress exerted by the weight of the overlying snow. Mathematically the problem is thus treated as if the weak layer were infinitely thin and the crack faces were freely penetrating

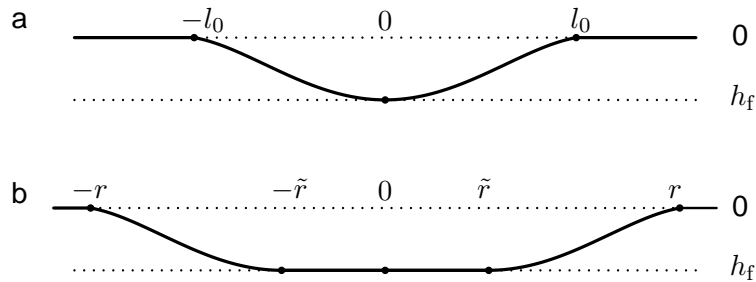


Figure 4.2: Crack-face contact, or tangency. **a:** For $r = l_0$ the crack faces make contact at a single point. **b:** For $r > l_0$, the crack faces are in contact in the interval $[-\tilde{r}, \tilde{r}]$.

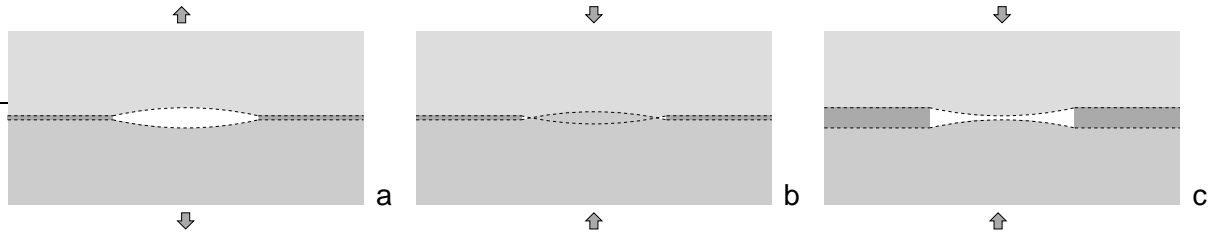


Figure 4.3: Mode equivalence. **a:** Mathematical model for tensile mode I interface crack. **b:** Mathematical model for interface anticrack (crack faces penetrate freely). **c:** Physical model of anticrack with weak layer of finite but small thickness and volumetric collapse of fracture debris.

each other (Fig. 4.3ab). Physically, the weak layer has a small but finite thickness and there is no interpenetration but a volume reduction of the fracture debris. The volume reduction allows the crack faces to bend towards each other (Fig. 4.3c). The situations a, b and c are equivalent for $r \gg h_f$ and until crack-face contact is established. The other difference resides in the non-remote loading by gravity. This results in a gradient in the stress field that has to be taken into account when the nucleus grows substantially. Applying established results for interface cracks [35], the mechanical energy $V_{m,0}(r)$ of a mixed-mode anticrack nucleus is obtained:

$$V_{m,0}(r) = -\frac{\pi\gamma r^2}{2E} (\tau^2 + \sigma^2), \quad r \ll h, \quad (4.3)$$

where γ is a constant of about one. The subscript 0 in $V_{m,0}$ indicates the nucleus situation $r \ll h$. A generalisation of Eq. 4.3 for non-rigid substrates is given later in section 4.4. The detailed derivation follows in section 4.7.1.

The longer the crack the less accurate is the crack energy expressed by Eq. 4.3. The main reason for this is the presence of the free boundary at the outer surface of the snow, which affects the stress field and therefore the mechanical energy. This new situation is approached by noting that the slab can be considered with reasonable accuracy as a Timoshenko beam if the crack is sufficiently long. The state of deformation in the slab is then described by the three displacement fields $u_x(x)$, $u_y(x)$ and $\psi(x)$ as shown in Fig. 4.4. The two situations shown in Fig. 4.1 b and c need to be distinguished.

Before tangency, the unilateral constraint Eq. 4.1 is not active. The displacement fields u_x , u_y and ψ are free in the anticrack interval $[-\tilde{r}, \tilde{r}]$. Outside the anticrack, in the intact portion $[-\infty, -\tilde{r}] \cup [\tilde{r}, +\infty]$, the fields are constrained by the conditions $u_y = 0$ and $u_x = h\psi/2$ (rigid support of the slab). The energy functional V of the Timoshenko beam subjected to gravity can be written as

$$V_m[u_x, u_y, \psi] = \int \left\{ \frac{Eh}{2} (\partial_x u_x)^2 + \frac{Eh^3}{24} (\partial_x \psi)^2 + \frac{kGh}{2} (\partial_x u_y - \psi)^2 - \tau u_x + \sigma u_y \right\} dx. \quad (4.4)$$

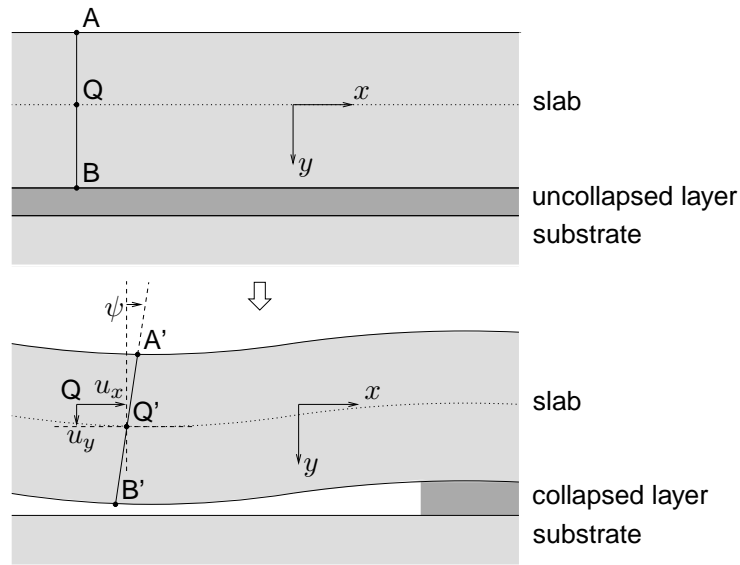


Figure 4.4: Field variables $u_x(x)$, $u_y(x)$ and $\psi(x)$ according to Timoshenko beam theory. Q is a point on the centre-line and moved to Q' after deformation.

By minimisation of this functional under the given constraints, the fields u_x , u_y and ψ are obtained. Substitution of these solutions back into Eq. 4.4 gives the mechanical energy of a crack $V_{m,1}(r)$ in terms of crack size:

$$V_{m,1}(r) = -\frac{r^3}{3Eh} [\lambda_\tau(r) \tau^2 + \lambda_\sigma(r) \sigma^2], \quad h \lesssim r \leq l_0, \quad (4.5)$$

where

$$\lambda_\tau(r) = 1 + \frac{9\eta^2}{3\eta^2 + 4(r/h)^2}, \quad \lambda_\sigma(r) = 3\eta^2 + \frac{4}{5}(r/h)^2 \frac{r/h + 9\eta/4}{r/h + \eta}. \quad (4.6)$$

Eq. 4.5 gives the mechanical energy of the crack for $r \gtrsim h$ but before tangency. The subscript 1 in $V_{m,1}$ indicates that this energy contribution stems from the Timoshenko beam. The derivation of Eqs. 4.5 and 4.6 is quite lengthy and given in section 4.7.2. The constant η appearing in Eq. 4.6 will resurface throughout the remainder of this text. It is given by

$$\eta = \left(\frac{E}{3kG} \right)^{1/2}, \quad (4.7)$$

where $k = 5/6$ is the Timoshenko correction factor for a rectangular beam section. It is observed that $\eta = 1$ for a Poisson solid (an elastic body with equal Lamé constants).

Until now, expressions for the crack energy for $r \ll h$ and $h \lesssim r \leq l_0$ have been obtained. Eq. 4.3 gives the energy contribution from the crack tip singularities, while Eq. 4.5 gives the

energy contribution from the Timoshenko deformation field, which replaces the far-field situation of remotely loaded bodies. An expression for V_m that is found remarkably accurate over the entire range $r < l_0$ is obtained by simply adding 4.3 and 4.5:

$$V_m(r) \cong V_{m,0}(r) + V_{m,1}(r), \quad r \leq l_0. \quad (4.8)$$

The validation of this equation is empirical. Comparison with results using finite element modelling (FEM) shows very satisfying agreement. These calculations and the comparison are detailed later in section 4.8.

The last case to consider is $r > l_0$, in which the unilateral constraint Eq. 4.1 imposes an upper limit to the subsidence of the slab (see Figs. 4.1c and 4.2b). The length of the unsupported portion of slab is $l = r - \tilde{r}$ on the positive half of the x -axis. The length l depends on r and tends to asymptotic values as $r \rightarrow \infty$. Heierli and Zaiser have shown that the dependency of the mechanical energy on the exact values of l is rather weak [33]. Given the usually large uncertainties in snow, there is not much point in developing the cumbersome equations which result from a rigorous treatment. The approximation $l \approx l_0$ is used instead. As a result, the displacement field near the crack tip of a long crack is approximated as a translation of the displacement field for a crack with half-length $r = l_0$. On the positive half of the x -axis the offset of the translation is $r - l_0$. On the negative half the offset is $-(r - l_0)$. Along the intervening interval $x \in [-\tilde{r}, \tilde{r}]$ the displacement field is constant and equal to h_f (see Fig. 4.1c). The mechanical energy is thus approximated by

$$V_m(r) \cong V_m(l_0) + 2\sigma h_f(r - l_0) - \frac{\tau_f^2}{3Eh} [r^3 \lambda_\tau(r) - l_0^3 \lambda_\tau(l_0)], \quad r > l_0, \quad (4.9)$$

where $V_m(l_0)$ is evaluated according to Eq. 4.8 and τ_f is the shear stress reduced by friction, $\tau_f = \tau + \mu\sigma$ if $\tau_f \geq 0$ and 0 if not.

Collecting the previous results Eqs. 4.3, 4.5, 4.8 and Eq. 4.9, and substituting them into Eq. 4.2, the final expression for the energy of a crack in the weak layer is

$$V(r) = \begin{cases} 2w_f r - \frac{\pi\gamma r^2}{2E} (\tau^2 + \sigma^2) - \frac{r^3}{3Eh} [\lambda_\tau(r) \tau^2 + \lambda_\sigma(r) \sigma^2], & r \leq l_0, \\ V(l_0) + 2(w_f + \sigma h_f)(r - l_0) - \frac{\tau_f^2}{3Eh} [r^3 \lambda_\tau(r) - l_0^3 \lambda_\tau(l_0)], & r > l_0, \end{cases} \quad (4.10)$$

where $V(l_0)$ is evaluated according to first case $r \leq l_0$. For $r > l_0$, crack energy can be interpreted as the energy of a shear crack with a fracture energy that is reduced by the energy σh_f recovered from gravitational collapse. Eq. 4.10 gives the energy for crack lengths from a few centimeters to virtually infinity and, hence, covers all scales from that of the incipient anticrack nucleus to that of the avalanche. The size of a critical crack follows from the crack length

that maximises $V(r)$, called the *critical* crack length. The corresponding value $V_c = V(r_c)$ is the magnitude of the energy barrier. The pair r_c, V_c indicates the energy barrier a crack must overcome to turn unstable. Three cases can be distinguished:

1. For $\mu \leq \tan \theta$, the crack energy function $V(r)$ has a unique maximum at r_c . The necessary condition $\partial_r V(r) < 0$ for crack propagation is met for $r > r_c$. This implies release of a slab avalanche, as the residual crack-face friction cannot support the slab.
2. For $\mu > \tan \theta$ and $w_f + \sigma h_f < 0$, there exists again a unique maximum r_c . The supercritical crack propagates but both slope-perpendicular and slope-parallel displacements cease as the crack faces make contact. This is the case of a whumpf.
3. For $\mu > \tan \theta$ and $w_f + \sigma h_f > 0$, the crack energy increases monotonically and the crack cannot become critical.

The preferred way to test the theory, designated here as method A, is to isolate a long cuboid of snow containing a weak layer. The weak layer is perforated with a snow saw near the middle, and a marker is set at this point, as shown in Fig. 4.5 a. An artificial crack is then sawed along the weak layer until the system becomes unstable (the direction of the cut does not matter). As soon as the crack starts propagating, the hand is taken off the snow saw. The critical length is the distance between the blade of the snow saw and the marker and can be compared with $2r_c$ resulting from Eq. 4.10.

Another possibility, designated as method B, is to notch the weak layer from an edge. The schematic of the experimental set-up is shown in Fig. 4.5 b and c. Similar experiments have already been carried out [25, 69] and the results are available in the literature. Because the topology is different from the previously calculated case, the expressions for crack energy are affected. It is noted that in Fig. 4.5 b the direction of the x -axis is inverted, affecting the sign of τ . Following the same steps as previously for the embedded crack, the following expression for the mechanical energy of a notch is obtained:

$$V_{m,1}(r) = -\frac{r^3}{6Eh} [\lambda_{\tau\tau}(r) \tau^2 + \lambda_{\sigma\tau}(r) \sigma\tau + \lambda_{\sigma\sigma}(r) \sigma^2], \quad (4.11)$$

where

$$\begin{aligned} \lambda_{\tau\tau}(r) &= 1 + \frac{9}{4}\eta \left(\frac{r}{h}\right)^{-1} + \frac{9}{4}\eta^2 \left(\frac{r}{h}\right)^{-2}, \\ \lambda_{\sigma\tau}(r) &= \frac{9}{2}\eta + \frac{9}{2}\eta^2 \left(\frac{r}{h}\right)^{-1}, \\ \lambda_{\sigma\sigma}(r) &= 3\eta^2 + \frac{9}{4}\eta \left(\frac{r}{h}\right) + \frac{9}{5} \left(\frac{r}{h}\right)^2. \end{aligned} \quad (4.12)$$

The cross-term in $\sigma\tau$ can contribute positively or negatively to the crack energy, depending on the sign of the product. A negative value of τ corresponds to a notch from the lower end of the

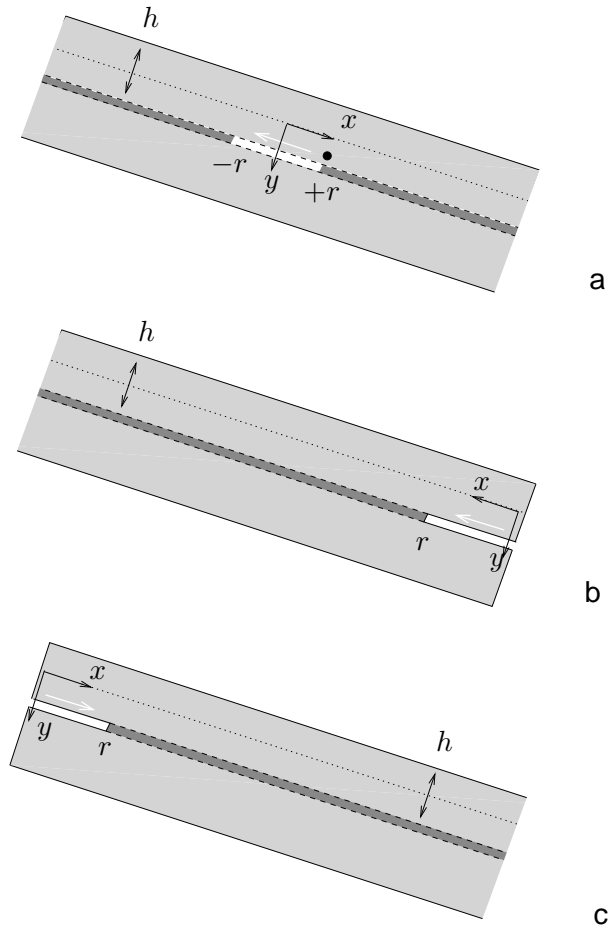


Figure 4.5: Configurations for field experimentation. **a**: Artificial crack embedded in weak layer. The black dot represents a marker set to show the initial position of the snow saw. **b**: Artificial notch on the lower end of sample. **c**: As previous, but notch on upper end. In b and c, the end face of the specimen is slope-perpendicular. The saw cut direction is indicated by a white arrow.

specimen (as shown in Fig. 4.5 b). A positive value of τ corresponds to a notch from the upper end (Fig. 4.5 c). The derivation of the above equations is given in section 4.7.3. Combining Eqs. 4.2, 4.3 (with a factor 1/2) and 4.11, the final expression for the energy of a notch in a weak layer can be written as

$$V(r) = w_f r - \frac{\pi \gamma r^2}{4E} (\tau^2 + \sigma^2) - \frac{r^3}{6Eh} [\lambda_{\tau\tau}(r) \tau^2 + \lambda_{\sigma\tau}(r) \sigma\tau + \lambda_{\sigma\sigma}(r) \sigma^2]. \quad (4.13)$$

In experiments with vertical instead of slope-normal end faces, a correction to the critical notch lengths resulting from Eq. 4.13 must be applied (see Fig. 4.6).

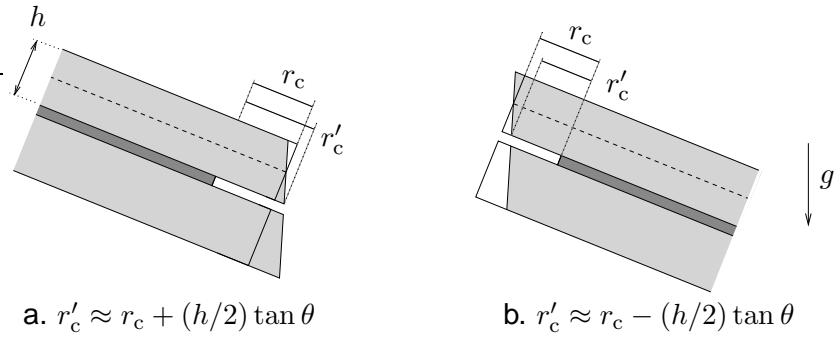


Figure 4.6: Correction of critical lengths in experiments with vertical instead of slope-normal end faces. **a:** Notch location at low end of specimen. **b:** Notch at top end of specimen.

4.2 Generalisation to arbitrary elastic mismatch

In the previous section the model was developed under the assumption of a rigid substrate. This condition can be relaxed only at the expense of mathematical complications. In one case however, a general analytical solution is straightforward. Given cracks that are short compared with slab thickness ($r \ll h$) and a finite Young's modulus of the substrate, the problem can be solved using results from Hutchinson [35] and Dundurs [15]. The calculation, which is presented in section 4.7.1, assumes the situation shown in Fig. 4.7, in which the moduli E and G and Poisson's ratio ν characterise the layer above the interface and E_0 , G_0 and ν_0 the layer below the interface. In this case the strain energy of an anticrack nucleus is given by

$$V_{m,0}(r) = -\frac{\pi\gamma r^2}{E(1-\alpha)} (\tau^2 + \sigma^2), \quad (4.14)$$

where

$$\alpha = \frac{E - E_0}{E + E_0}, \quad (4.15)$$

$$\gamma = (1 - \beta^2) \left(1 + \pi^{-2} \ln^2 \frac{1 - \beta}{1 + \beta} \right). \quad (4.16)$$

Here, α and β are Dundurs' elastic mismatch parameters [15]. The parameter α takes values between -1 when $E \ll E_0$ and $+1$ when $E \gg E_0$. The parameter γ , which depends on β but not on α , takes a value of about one (physically admissible values are between 0.84 and 1, which follows from restrictions on β [35]). To compute γ precisely if necessary, Dundurs' definition of β can be used, i.e. $\beta = [G(\kappa_0 - 1) - G_0(\kappa - 1)]/[G(\kappa_0 + 1) + G_0(\kappa + 1)]$, with $\kappa = 3 - 4\nu$ in plane strain and $\kappa = (3 - \nu)/(1 + \nu)$ in plane stress (and accordingly for κ_0), see [15]. Eq. 4.3 is obtained by substitution of $\alpha = -1$ into Eq. 4.14, which corresponds to the limiting case of a rigid substrate.

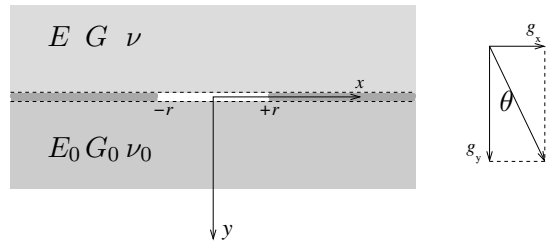


Figure 4.7: Interface crack between mismatching elastic layers. ν , E and G are respectively the Poisson's ratio, the Young's modulus and the shear modulus of the slab. ν_0 , E_0 and G_0 are the corresponding values of the substrate.

4.3 Limiting cases

By imposing additional conditions and constraints, a number of limiting cases can be obtained from the mixed-mode anticrack model. In particular, the simple shear models [50, 53] and previous collapse models [32, 33] can be recovered.

McClung's simple shear model for long cracks [53] (see section 3.1.2) imposes the constraint that the slab can only slide in the x -direction, but cannot move in y -direction (i.e. the slab can neither lift nor subside). In the anticrack model, this constraint is expressed by $h_f = 0$ and therefore tangency is immediately fulfilled (for $r = 0$). Consequently $l_0 = 0$ and the second case of Eq. 4.10 applies. Making these substitutions and observing that $V(l_0) = 0$ when $l_0 = 0$ and that $\lambda_\tau(r) \rightarrow 1$ for long cracks (Eq. 4.6), indeed recovers Eq. 3.6. This limit of the anticrack model is therefore equivalent to the model of McClung for long shear cracks.

In order to recover Louchet's simple shear model for short cracks [50] (see section 3.1.1), it is observed that in the case of $r \ll h$ the crack energy is given by $V(r) = 2w_f r + V_{m,0}(r)$, where the second term on the right-hand side stems from Eq. 4.14. In Louchet's model, identical elastic properties above and below the weak layer are considered. This case is obtained by setting $\alpha = 0$. Moreover, as no work is done by the compressive forces in the case of a simple shear crack, this contribution to the crack energy must be removed. This is formally equivalent to setting $\sigma = 0$ in $V_{m,0}(r)$. Finally, as the crack faces are always in contact, the work done by the shear stress τ is reduced by crack-face friction. This is formally equivalent to replacing τ by $\tau_f = \tau - \tau_r$ in $V_{m,0}(r)$. Making these substitutions, recovers Eq. 3.5. This limit of the anticrack model is therefore equivalent to the model of Louchet for short shear cracks.

The collapse model for horizontal configurations proposed by Heierli and Zaiser [32] (see section 3.2.3) considers a sufficiently stiff slab, so that the use of the Euler-Bernoulli beam equation is justified. Because of horizontality, $\tau = \tau_f = 0$ and $\sigma = \rho g h$ (the weight per unit area above the weak layer). In order to recover this model from the anticrack model presented here, it is observed that $\lambda_\tau(r)$ and $\lambda_\sigma(r)$ (Eq. 4.6) tend to 1 and $\frac{4}{5}(r/h)^2$ respectively, when $r \rightarrow +\infty$. Substituting $\lambda_\tau(r) = 1$ and $\lambda_\sigma(r) = \frac{4}{5}(r/h)^2$ into Eq. 4.5 indeed recovers Eq. 3.10.

The collapse model for slopes proposed by Heierli and Zaiser [33] uses the more accurate Timoshenko beam model instead of the Euler-Bernoulli model to calculate the strain field. In the Timoshenko beam model, r is assumed larger but not necessarily much larger than h , and the more accurate approximation $\lambda_\sigma(r) = 3\eta^2 + \frac{4}{5}(r/h)^2$ must be used. Substituting this and $\lambda_\tau(r) = 1$ into Eq. 4.5 recovers indeed Eqs. 10 and 14 of [33].

4.4 Nucleus instability

In this section an anticrack nucleus of finite size is considered (i.e. $0 < r \ll h$ and $r < l_0$ are assumed). In this case the crack energy of a nucleus is given by $V(r) = 2w_f r - V_{m,0}(r)$, where $V_{m,0}(r)$ stems from Eq. 4.14, which is more general than Eq. 4.3 and accounts for elastic mismatch between slab and substrate.

Excluding any external loads on the snowpack for the moment, the load on the undisturbed weak layer can be expressed in terms of the weight of the overlying snow. In the coordinate system introduced at the beginning of the chapter, the shear stress is given by $\tau = \pm \rho h g \sin \theta$ and the compressive stress is given by $\sigma = -\rho h g \cos \theta$. Here, ρ is the density of the slab, h its thickness and g is the acceleration of gravity. The sum $\tau^2 + \sigma^2$ appearing in Eq. 4.14 is independent of slope angle. Using $\partial_r V(r) = 0$ to find the saddle point of the energy function, the following condition for instability is obtained:

$$\text{Nucleus instability} \Leftrightarrow r \geq r_c, \quad r_c = \frac{1 - \alpha}{\gamma} r_0, \quad (4.17)$$

where $r_0 = w_f E / (\pi \sigma_0^2)$ and $\sigma_0 = -\rho g h$. This relation is interesting for several reasons. Firstly, it expresses that the critical length for a porosity fluctuation or small crack is independent of slope angle. Slope angle thus plays no role in fracture nucleation in absence of loads other than the own weight of the snow. Secondly, the condition shows how the stability of a crack nucleus is affected by the substrate. Assume two situations with identical slab and weak layer, but different substrates. In both situations, w_f , E and σ_0 are equal. The only variable parameters are α and γ . As the variations of γ are small, the situations compare mainly on the basis of α . The expression for r_c shows that, the closer α is to +1, i.e. the 'softer' the substrate with respect to the slab, the smaller the critical crack length. Conversely, the closer α is to -1, i.e. the 'harder' the substrate with respect to the slab, the larger the critical crack length. Given identical weak layer and slab with fixed elastic modulus, situations involving soft bed surface appear to be more dangerous than situations involving hard bed surface. Thirdly, the critical crack length r_c can also decrease when a subsurface layer with very low Young's modulus forms by sintering within the snowpack, as is possibly the case for a layer of faceted crystals forming under a dense slab. In this case α increases and thus r_c decreases.

4.5 Skier instability

The influence of a local line force on the stability of a slope is investigated in this section. The aim is to describe the conditions under which loads such as those exerted by a skier may cause extended failure in the weak layer. Consider a crack in an otherwise intact snow stratification under the action of a line load as shown in Fig. 4.8. To account for the work done by the line force $p = (p_x, p_y)$ acting on the middle of the unsupported slab, the following term ΔV must be added to the energy functional Eq. 4.4:

$$\Delta V[u_x, u_y] = -p_x u_x(0) - p_y u_y(0). \quad (4.18)$$

The calculation of this perturbation is developed later in section 4.7.4. Here, the essential result is given: The introduction of a line force p at the center of the unsupported slab results in a crack energy of the form

$$V(r) = 2w_f r - \frac{r}{4Eh} (p_x^2 + 3\eta^2 p_y^2) + \mathcal{O}(r^2) \quad (4.19)$$

as long as tangency is not established. In order to describe the action of a skier in absence of cracks, the limit $r \rightarrow 0$ is taken. Neglecting the term in $\mathcal{O}(r^2)$ and imposing the condition $\partial_r V(0) \leq 0$, the instability criterion can be expressed in the following, simple form:

$$\text{Skier instability} \Leftrightarrow w_p \geq w_f, \quad w_p = \frac{1}{8Eh} (p_x^2 + 3\eta^2 p_y^2). \quad (4.20)$$

If $w_p \geq w_f$, the slope is unstable under the action of the skier. Regarding this condition, a few observations can be made. Firstly, the line force p which annihilates, according to Eq. 4.20, the energy barrier for crack nucleation is indeed of the order of the weight of a skier. An example of this will be given in section 4.9. Secondly, the factor $3\eta^2 \approx 3$ favors the compressive component

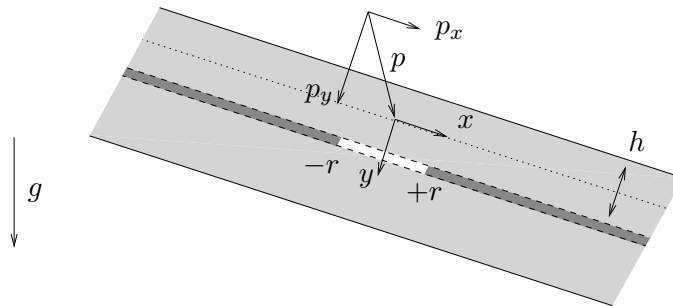


Figure 4.8: A skier acting as a line force on the center line of slab, which bends (not shown) and increases the strain on the crack tips.

p_y over the shear component p_x in the reduction the energy barrier. Thirdly, because $w_p \propto p^2$, the odds of triggering a slab avalanche may significantly increase as the line load p increases. Hence, according to the model, skiing dynamically or falling (involving loads p which are larger than the weight of the skier) considerably increases the chances of triggering a slab.

4.6 Gap instability

The situation of a notch described by Eq. 4.11 can also be encountered in a natural snowpack. Consider the situation shown schematically in Fig. 4.9, in which a transverse opening in the snowpack extends across the slab. In skier jargon such openings of the snowpack, if natural, are known as 'cracks', but obviously this term may lead to some confusion within the scope of this work. For this reason such an opening in the snowpack will be referred to as a *gap*. It is now asked under which conditions this configuration is unstable and leads spontaneously to failure.

Recalling Eqs. 4.12 and 4.13, and collecting the terms of second and higher orders in r , the crack energy for each side of the gap can be rewritten as

$$V(r) = w_f r - \frac{3}{8} \frac{\tau^2}{E} h \eta^2 r + \mathcal{O}(r^2) \quad (4.21)$$

As in the previous section, the particular interest lays in the limit $r \rightarrow 0$. Neglecting the term $\mathcal{O}(r^2)$ and imposing $\partial_r V(0) < 0$ as previously, the instability criterion can be expressed in the following, simple form:

$$\text{Gap instability} \Leftrightarrow w_\tau \geq w_f, \quad w_\tau = \frac{3}{8} \frac{\tau^2}{E} h \eta^2, \quad (4.22)$$

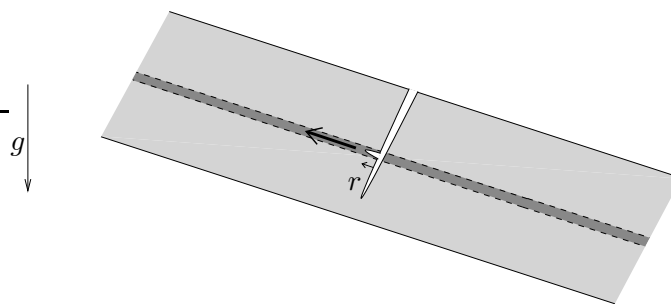


Figure 4.9: An open gap in a slope, due to a transverse fault. A crack nucleus in the weak layer is shown on the upper half, but can equally occur in the lower half. The arrow indicates the propagation direction. Physically, the situations on each side of the gap, taken individually, are equivalent to those shown in Fig. 4.5b and c in the limit of $r \rightarrow 0$.

where $\tau = \rho gh \sin \theta$. If $w_\tau \geq w_f$, the slope is unstable in presence of a gap. Contrary to the two previous conditions of instability, this one reflects a pure shear instability involving τ but not σ . Gap instability is favoured by thick slabs (large h) and steep slopes (large τ).

4.7 Derivations

The detailed mathematical derivations of Eqs. 4.3, 4.5, 4.11, 4.14 and 4.19 are presented on the following pages.

4.7.1 Energy of an anticrack nucleus.

In order to derive Eq. 4.14, the problem of finding the formation energy of an anticrack nucleus is mapped onto a solved problem. Physically, it is clear that the repacking of the ice grains during fracture takes place in a finite volume. The mathematical difficulties which arise from dealing with the computation of the strain field for a finite separation of slab and substrate can nevertheless be avoided by considering the equivalence of the three situations a, b and c previously shown in Fig. 4.3. The situation in panel a has previously been solved by Malyshev and Salganik [52] and Hutchinson and Suo have reformulated their results in a modern notation [35]. This solution can be applied to the situation of a mixed-mode anticrack at the interface between two different elastic media. Using the notation introduced in section 4.4 and Fig. 4.7, the energy release rate $-\partial_r V_{m,0}(r)$ of an interface crack of length $2r$ can be expressed as [35, 52]:

$$-\frac{1}{2} \partial_r V_{m,0}(r) = (1 - \beta^2) \frac{K \overline{K}}{E_*} = \frac{1 - \beta^2}{1 - \alpha} \frac{K \overline{K}}{E}, \quad (4.23)$$

where $E_*^{-1} = \frac{1}{2}(E^{-1} + E_0^{-1})$, α and β are Dundurs' elastic mismatch parameters across the interface, and K is the interface stress intensity factor. The overline denotes the complex conjugate operator. It is observed that $E_* = E(1 - \alpha) = E_0(1 + \alpha)$. Next, an expression for the interface stress intensity factor in Eq. 4.23 is needed. An analytical expression for K has been given for an isolated interface crack of length $2r$ between remotely stressed semi-infinite elastic blocks [35]. For the right-hand tip of the crack:

$$K(r) = (\sigma + i\tau)(1 + 2i\epsilon)\sqrt{\pi r}(2r)^{-i\epsilon}, \quad (4.24)$$

where $\epsilon = \ln[(1 - \beta)/(1 + \beta)]/(2\pi)$. This expression is applicable to the present situation provided that the crack length is small with respect to the depth of the weak layer, $r \ll h$. Substitution of Eq. 4.24 into Eq. 4.23, integration over r and imposing $V_{m,0}(0) = 0$, proves Eq. 4.14. The constant γ is given by

$$\gamma = (1 - \beta^2) \left(1 + \frac{1}{\pi^2} \ln^2 \frac{1 - \beta}{1 + \beta} \right). \quad (4.25)$$

Physically admissible values of γ are comprised between 0.84 and 1. Three remarks can be made. Firstly, in the case of a stiff substrate, $\alpha = -1$. Substitution of this value in Eq. 4.14 recovers Eq. 4.3. Secondly, in absence of elastic mismatch, $\alpha = \beta = \gamma = 0$. Thirdly, in case of a stiff substrate, if values of ν are unavailable, a reasonable approximation should be to associate snow with a Poisson solid. In this case $\nu = 1/4$, $\beta = -1/3$ and $\gamma \approx 0.93$.

4.7.2 Energy of an anticrack with free faces

In the following Eq. 4.5 is derived. The problem was posed earlier in section 4.1. In order to handle the calculation more easily, non-dimensional variables and constants as defined in Table 4.1 are used.

The centre of the anticrack of length $2R$ is located at $X = 0$ (see Fig. 4.5a). The slab above the weak layer is treated as a Timoshenko beam. It is unsupported over the crack length (until tangency) and supported elsewhere. The variational problem can be stated as follows: Amongst the virtual displacement fields $U_1(X)$, $U_2(X)$ and $\psi(X)$ compatible with the conditions (i) $U_2(X) \leq 1$ for all $|X| < R$ (no interpenetration of the anticrack faces) and (ii) $U_2(X) = 0$ and $U_1(X) = \psi(X)/2$ for all $|X| > R$ (rigid support of the slab outwith the anticrack), find those which minimize the crack energy functional

$$\begin{aligned} \Phi[U_1, U_2, \psi] = & \int_{[-R, R]} \left\{ \frac{3\eta^2}{2} (\partial_X U_1)^2 + \frac{\eta^2}{8} (\partial_X \psi)^2 + \frac{1}{2} (\partial_X U_2 - \psi)^2 - T U_1 - \Sigma U_2 \right\} dX \\ & + \int_{[-\infty, -R] \cup [R, \infty]} \left\{ \frac{\eta^2}{2} (\partial_X \psi)^2 + \frac{1}{2} \psi^2 - \frac{T}{2} \psi \right\} dX. \end{aligned} \quad (4.26)$$

Table 4.1: Scaled variables (dimensionless numbers and fields).

	Variables:	Scaling:
Space coordinates:	X	$X = x/h$
-	Y	$Y = y/h$
Crack (half-) length:	R	$R = r/h$
Displacements:	U_1	$U_1 = u_x/h$
-	U_2	$U_2 = u_y/h$
Crack energy:	Φ	$\Phi = V/(kGh^2)$
Fracture energy:	W_f	$W_f = w_f/(kGh)$
Stress:	T	$T = \tau/(kG)$
-	Σ	$\Sigma = -\sigma/(kG)$

This expression of the crack energy is defined up to a constant which can be obtained by imposing $\Phi = 0$ for cracks of length zero. The Euler-Lagrange equations of the energy functional Eq. 4.26 are:

$$3\eta^2 \partial_{XX} U_1 = -T, \quad (4.27)$$

$$\partial_{XX} U_2 - \partial_X \psi = -\Sigma, \quad (4.28)$$

$$\frac{1}{4}\eta^2 \partial_{XX} \psi + \partial_X U_2 - \psi = 0, \quad (4.29)$$

in the cracked interval $[-R, R]$, and

$$\eta^2 \partial_{XX} \psi - \psi = -\frac{T}{2}, \quad (4.30)$$

$$U_1(X) = \frac{1}{2}\psi(X), \quad (4.31)$$

$$U_2(X) = 0, \quad (4.32)$$

in the uncracked interval $[-\infty, -R] \cup [R, \infty]$. A piecewise linear form is non-linear if the piecewise forms are not identical. The global non-linearity of the Euler-Lagrange equations therefore resides in their different forms inside and outside the cracked interval $[-R, R]$. Equations 4.27 to 4.32 can be solved by integrating them separately in $[-R, R]$ and in $[-\infty, -R] \cup [R, \infty]$ and subsequently matching the solution pairs at the pseudo-boundaries at $X = -R$ and $X = R$. To begin with, the Euler-Lagrange equations are solved in $[-R, R]$. The general solution is:

$$U_1(X) = C_6 + C_5 X - \frac{1}{6\eta^2} T X^2, \quad |X| \leq R, \quad (4.33)$$

$$U_2(X) = C_4 + C_3 X + \frac{1}{2} C_2 X^2 + \frac{1}{6} C_1 X^3 + \frac{1}{6\eta^2} \Sigma X^4, \quad |X| \leq R, \quad (4.34)$$

$$\psi(X) = C_3 + \frac{\eta^2}{4} C_1 + (C_2 + \Sigma) X + \frac{1}{2} C_1 X^2 + \frac{2}{3\eta^2} \Sigma X^3, \quad |X| \leq R. \quad (4.35)$$

Except for the coupling through the pseudo-boundaries, the first of these equations is independent of the second and third. In order to solve Eq. 4.33 independently, the rotations of the cross-sections at $X = -R$ and $X = R$ are designated by ψ^- and ψ^+ respectively. ψ^- and ψ^+ are to be determined later. In the following it is useful to define $\psi_s = (\psi^+ + \psi^-)/2$ and $\psi_a = (\psi^+ - \psi^-)/2$ (where 's' stands for symmetrical and 'a' for anti-symmetrical). The coefficients C_5 and C_6 are determined by the pseudo-boundary conditions $U_1(-R) = \psi^-/2$ and $U_1(R) = \psi^+/2$:

$$C_5 = \frac{1}{2} \frac{\psi_a}{R}, \quad (4.36)$$

$$C_6 = \frac{1}{2} \psi_s + \frac{1}{6} T \frac{R^2}{\eta^2}. \quad (4.37)$$

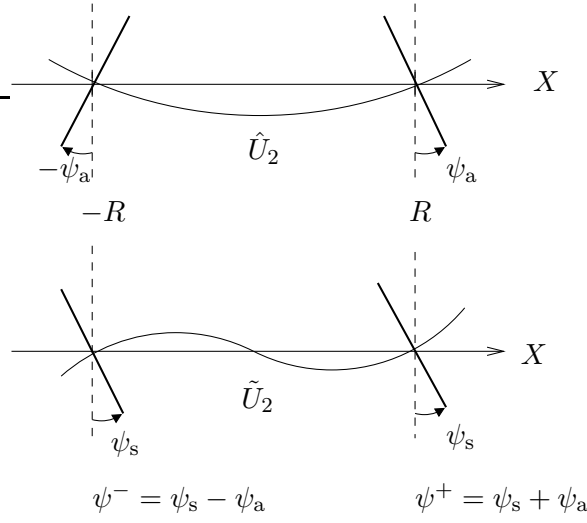


Figure 4.10: Deformation profiles \hat{U}_2 , \tilde{U}_2 and corresponding rotations $\psi(-R) = \psi^-$ and $\psi(R) = \psi^+$ at the pseudo-boundaries at $-R$ and $+R$. The symmetrical part \hat{U}_2 of U_2 is associated with the anti-symmetrical part $\tilde{\psi}$ of ψ . Conversely, the anti-symmetrical part \tilde{U}_2 of U_2 is associated with the symmetrical part $\hat{\psi}$ of ψ .

Attention is now turned to Eqs. 4.28 and 4.29. Inspection of these shows that their solutions can be decomposed into a sum of a symmetrical term and an anti-symmetrical term (odd derivatives of U_2 pair with even derivatives of ψ and inversely): $U_2 := \hat{U}_2 + \tilde{U}_2$ and $\psi := \hat{\psi} + \tilde{\psi}$, where the hat stands for the symmetrical part and the tilde for the anti-symmetrical part (Fig. 4.10). The coefficients C_2 and C_4 are determined by the pseudo-boundary conditions $\hat{U}_2(R) = 0$ and $\tilde{\psi}(R) = \psi_a$:

$$C_2 = -\Sigma \left(1 + \frac{2}{3} \frac{R^2}{\eta^2} \right) + \frac{\psi_a}{R}, \quad (4.38)$$

$$C_4 = \frac{1}{2} \Sigma R^2 \left(1 + \frac{1}{3} \frac{R^2}{\eta^2} \right) - \frac{1}{2} R \psi_a. \quad (4.39)$$

The coefficients C_1 and C_3 are determined by the pseudo-boundary conditions $\tilde{U}_2(R) = 0$ and $\hat{\psi}(R) = \psi_s$:

$$C_1 = \frac{12\psi_s}{3\eta^2 + 4R^2}, \quad C_3 = -\frac{2\psi_s R^2}{3\eta^2 + 4R^2}. \quad (4.40)$$

The functions U_2 and ψ thus satisfy the relations $U_2(-R) = U_2(R) = 0$, $\psi(-R) = \psi^-$ and $\psi(R) = \psi^+$ at the pseudo-boundaries.

Next the solutions in $[-\infty, -R] \cup [R, \infty]$ are considered. As equations for U_1 and U_2 are already known from Eqs. 4.31 and 4.32, the problem is reduced to finding $\psi(X)$ satisfying equation 4.30.

The general solution is of the form:

$$\psi(X) = C_1 e^{X/\eta} + C_2 e^{-X/\eta} + \frac{T}{2}, \quad |X| \geq R. \quad (4.41)$$

With the pseudo-boundary conditions $\psi(R) = \psi^+$ and $\psi(-R) = \psi^-$, the solutions are:

$$\psi(X) = \left(\psi^+ - \frac{T}{2} \right) e^{-(X-R)/\eta} + \frac{T}{2}, \quad X \geq R, \quad (4.42)$$

$$\psi(X) = \left(\psi^- - \frac{T}{2} \right) e^{+(X+R)/\eta} + \frac{T}{2}, \quad X \leq -R. \quad (4.43)$$

Except for the unknown rotations ψ^+ and ψ^- at the pseudo-boundaries, which are still to be specified, the solution in the entire domain of definition $[-\infty, \infty]$ has now been obtained. By substituting these results into the energy functional 4.26 for a crack of length $2R$ and a crack of length 0, and taking the difference, one obtains

$$\begin{aligned} \Phi = & \frac{1}{4}R \left(1 - \frac{4R^2}{9\eta^2} \right) T^2 - \psi_s R T - \frac{R^3}{3} \left(1 + \frac{4R^2}{15\eta^2} \right) \Sigma^2 + \frac{2}{3} \psi_a R^2 \Sigma \\ & + \frac{\eta^2}{R} \psi_a^2 + \frac{R}{1 + \frac{4R^2}{3\eta^2}} \psi_s^2 + \frac{\eta}{2} \left(\psi^+ - \frac{T}{2} \right)^2 + \frac{\eta}{2} \left(\psi^- - \frac{T}{2} \right)^2. \end{aligned} \quad (4.44)$$

The expressions for ψ^+ and ψ^- are determined by minimising the energy functional 4.26 with respect to ψ^+ and ψ^- . As simple analytical expressions for ψ^+ and ψ^- are unavailable, the problem is reduced to a single variable $\Delta\psi$ by imposing $\psi^+ \cong T/2 + \Delta\psi$ and $\psi^- \cong T/2 - \Delta\psi$ (N.B. as can be seen from Eq. 4.30, $\psi = T/2$ is the equilibrium rotation angle in the far-field). The energy function 4.44 is then minimised with respect to $\Delta\psi$, leading to

$$\Delta\psi = -\frac{1}{3} \frac{R^3}{\eta(\eta + R)} \Sigma. \quad (4.45)$$

An example of the resulting displacement profile is shown in Fig. 4.11. Combining the last two results, the integration of the energy functional leads to the final expression for the mechanical energy of an anticrack

$$\Phi = -\lambda_1 T^2 - \lambda_2 \Sigma^2, \quad (4.46)$$

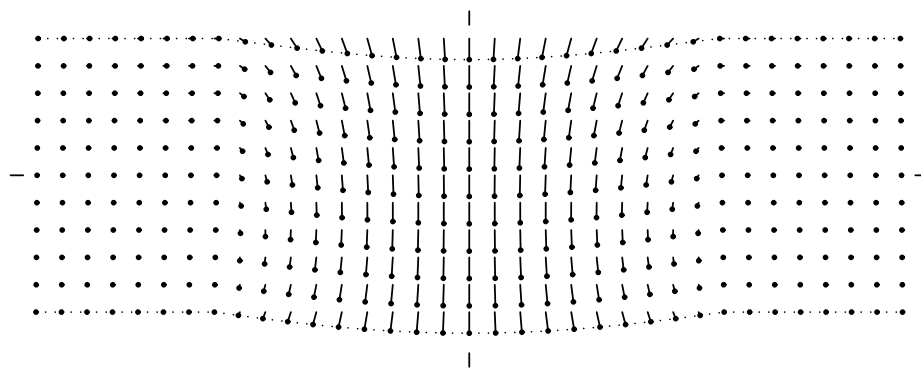
where

$$\lambda_1 = \frac{R^3}{9\eta^2} \left(1 + \frac{9\eta^2}{4R^2 + 3\eta^2} \right), \quad \lambda_2 = \frac{R^3}{9\eta^2} \left(3\eta^2 + \frac{4}{5}R^2 \frac{R + 9\eta/4}{R + \eta} \right). \quad (4.47)$$

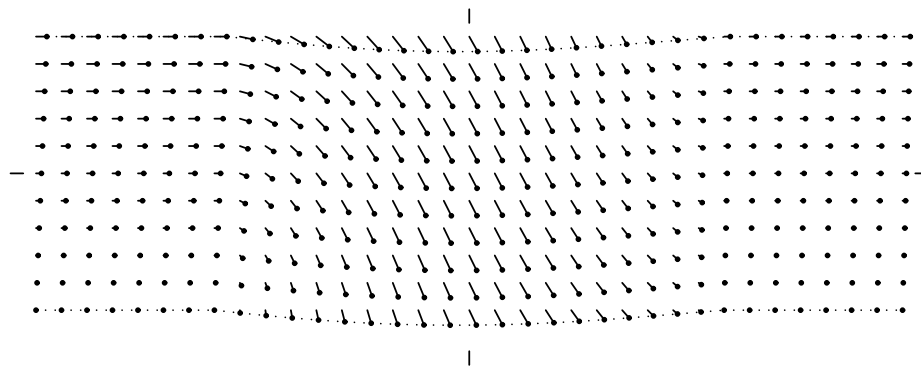
Reverting to dimensional variables yields equation 4.5.

The half-length $l_0 = L_0 h$ at which tangency between the opposing faces of the anticrack occurs can be obtained by observing that, except for nearly vertical slopes, $\hat{U}_2(X) \gg \tilde{U}_2(X)$ around $X = 0$ where contact is expected. Hence, the touch-down condition is approximately $U_2(0) = H_f$. The tangency length l_0 is determined by finding the positive real root L_0 of

$$L_0^2 \left(1 + \frac{L_0^2}{3\eta^2} \frac{L_0 + 2\eta}{L_0 + \eta} \right) = \frac{2H_f}{\Sigma}. \quad (4.48)$$



a



b

Figure 4.11: Example for displacement field in the slab, as given by Eqs 4.33 to 4.40, 4.42, 4.43 and 4.45. The four surrounding ticks show the location of the x and y axes. **a:** Slope angle $\theta = 0^\circ$. **b:** Slope angle $\theta = 45^\circ$. Data: $\rho = 200 \text{ kg/m}^3$, $E = 5.0 \text{ MPa}$, $r = h = 0.5 \text{ m}$. Magnification factor for displacement: 175, grid spacing: 5 cm.

4.7.3 Energy of a notch

In the following Eq. 4.11 is derived. The case of a notch into the weak layer is considered. Formally, by analogy with the notion of anticrack, one might speak of an antinotch but there is little reason to do so because notches of finite width can always be loaded in compression. In order to calculate the mechanical energy of a notch, two cases must be distinguished: The notch can be sawed into the weak layer from the lower end of the sample in uphill direction (Fig. 4.5b), or from the upper end in downhill direction (Fig. 4.5c). In horizontal terrain, both situations are equivalent, but on a slope the results are substantially different. For convenience, the coordinate system is chosen as shown in Fig. 4.5 b and c. This ensures that x and r are always positive. Analytically, the only difference between the two cases resides in the sign change of T .

The energy functional of a notch is similar to the case of an embedded anticrack, except for the integration domain, which now spans from 0 to $+\infty$, instead of $-\infty$ to $+\infty$:

$$\begin{aligned} \Phi[U_1, U_2, \psi] = & \int_0^R \left\{ \frac{3\eta^2}{2} (\partial_X U_1)^2 + \frac{\eta^2}{8} (\partial_X \psi)^2 + \frac{1}{2} (\partial_X U_2 - \psi)^2 - T U_1 - \Sigma U_2 \right\} dX \\ & + \int_R^{+\infty} \left\{ \frac{\eta^2}{2} (\partial_X \psi)^2 + \frac{1}{2} \psi^2 - \frac{T}{2} \psi \right\} dX. \end{aligned} \quad (4.49)$$

In the subdomain $[R, \infty]$, the conditions 4.31 and 4.32 apply to ensure rigid support of the slab. On the boundary at $X = 0$ and the pseudo-boundary at $X = R$, the conditions $\partial_X U_1(0) = 0$, $U_1(R) = \psi^+/2$, $\partial_X U_2(0) - \psi(0) = 0$, $U_2(R) = 0$, and $\partial_X \psi(0) = 0$, $\psi(R) = \psi^+$ are imposed. The solutions for U_1 , U_2 , and ψ are then given by Eqs. 4.33 to 4.35, with

$$C_1 = 0, \quad (4.50)$$

$$C_2 = -\Sigma, \quad (4.51)$$

$$C_3 = -\frac{2}{3} \frac{R^3}{\eta^2} \Sigma + \psi^+, \quad (4.52)$$

$$C_4 = \frac{1}{2} R^2 \left(1 + \frac{R^2}{\eta^2} \right) \Sigma - R\psi^+, \quad (4.53)$$

$$C_5 = 0, \quad (4.54)$$

$$C_6 = \frac{1}{6} \frac{R^2}{\eta^2} T + \frac{1}{2} \psi^+. \quad (4.55)$$

By substituting these results into the energy functional 4.49 for a notch of length R and a notch of length 0, and taking the difference, the following expression for the mechanical energy is

obtained:

$$\Phi = -\frac{R}{2} \left(\frac{1}{9} \frac{R^2}{\eta^2} - \frac{1}{4} \right) T^2 + \frac{1}{2} \psi^+ R (R\Sigma - T) - \frac{R^3}{6} \left(1 + \frac{3}{5} \frac{R^2}{\eta^2} \right) \Sigma^2 + \frac{\eta}{2} \left(\frac{T}{2} - \psi^+ \right)^2. \quad (4.56)$$

Minimising with respect to ψ^+ leads to

$$\psi^+ = \frac{T}{2} \left(1 + \frac{R}{\eta} \right) - \frac{\Sigma}{2\eta} R^2. \quad (4.57)$$

An example of the resulting displacement profile is shown in Fig. 4.12. Combining the last two results, the final expression for the mechanical energy of a notch of length R is

$$\Phi = -\lambda_1 T^2 + \lambda_{12} \Sigma T - \lambda_2 \Sigma^2, \quad (4.58)$$

where

$$\lambda_1 = \frac{R}{8} \left(1 + \frac{R}{\eta} + \frac{4}{9} \frac{R^2}{\eta^2} \right), \quad (4.59)$$

$$\lambda_{12} = \frac{R^2}{4} \left(1 + \frac{R}{\eta} \right), \quad (4.60)$$

$$\lambda_2 = \frac{R^3}{6} \left(1 + \frac{3}{4} \frac{R}{\eta} + \frac{3}{5} \frac{R^2}{\eta^2} \right). \quad (4.61)$$

Reverting to dimensional variables yields Eq. 4.11. Note that, unlike the energy of a crack, the energy of a notch depends on the sign of T .

Looking for an expression for the touch-down length is not necessary in this case. Contact between slab and substrate can always be avoided by making the notch sufficiently wide, e.g. by choosing a thicker snow saw or by using two saws in parallel.

4.7.4 Energy reduction by a line force

In the following a simple treatment of the influence of line loads such as those involved in skier triggering is given. The problem is posed in section 4.5 and reformulated using the non-dimensional variables defined in Table 4.1. In addition, non-dimensional loads are defined:

$$P_1 = \frac{p_x}{kGh}, \quad P_2 = \frac{p_y}{kGh}. \quad (4.62)$$

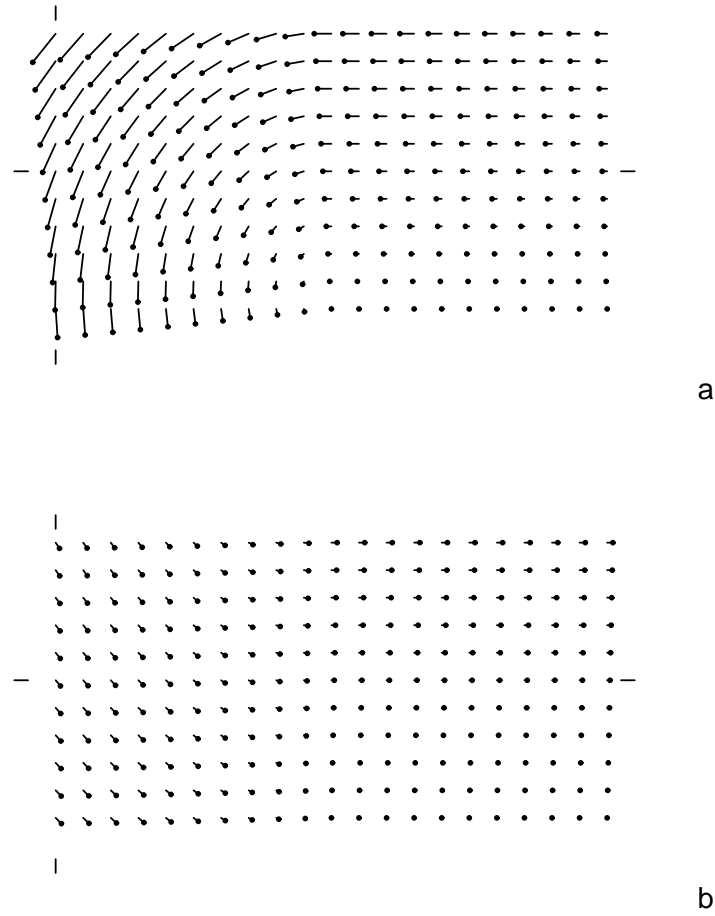


Figure 4.12: Example for displacement field in the slab, as given by Eqs 4.33 to 4.35, 4.42, 4.50 to 4.55 and 4.57. The four surrounding ticks show the location of the x and y axes. **a:** Notch on lower end. **b:** Notch on upper end. Data: $\rho = 200 \text{ kg/m}^3$, $E = 5.0 \text{ MPa}$, $\theta = 45^\circ$, $r = h = 0.5 \text{ m}$. Magnification factor for displacement: 100, grid spacing: 5 cm.

With these definitions, the energy functional for the configuration shown in Fig. 4.8 can be written as

$$\Phi[U_1, U_2, \psi] = \int \left\{ \frac{3\eta^2}{2} (\partial_X U_1)^2 + \frac{\eta^2}{8} (\partial_X \psi)^2 + \frac{1}{2} (\partial_X U_2 - \psi)^2 - T U_1 - \Sigma U_2 - P_1 U_1 \delta(X) - P_2 U_2 \delta(X) \right\} dX, \quad (4.63)$$

where $\delta(X)$ is Dirac's delta distribution. For the moment, T and Σ are set to nil. The linearity of the elasticity problem allows later superposition of the gravity-induced strain field. The Euler-

Lagrange equations of Eq. 4.63 are

$$3\eta^2 \partial_{XX} U_1 = -P_1 \delta(X), \quad (4.64)$$

$$\partial_{XX} U_2 - \partial_X \psi = -P_2 \delta(X), \quad (4.65)$$

$$\frac{1}{4}\eta^2 \partial_{XX} \psi + \partial_X U_2 - \psi = 0, \quad (4.66)$$

in the cracked interval $[-R, R]$. Neglecting the deformation field outwith the crack, the boundary conditions $U_1(\pm R) = 0$, $U_2(\pm R) = 0$ and $\psi(\pm R) = 0$ are used. The solutions of Eqs. 4.64 to 4.66 are:

$$U_1(X) = P_1 \frac{R - |X|}{6\eta^2}, \quad (4.67)$$

$$U_2(X) = P_2 \frac{3\eta^2(R - |X|) + (R + 2|X|)(R - |X|)^2}{6\eta^2}, \quad (4.68)$$

$$\psi(X) = -P_2 \frac{X(R - |X|)}{\eta^2}. \quad (4.69)$$

An example of the displacement profile is shown in Fig. 4.13. Using the superposition principle for linear elasticity, this solution can be combined with the solution for a crack loaded by $T, \Sigma \neq 0$ but not by P , which was calculated in section 4.7.2. Thus, redefining U_1 as the sum of Eqs. 4.67 and 4.33, U_2 as the sum of Eqs. 4.68 and 4.34, and ψ as the sum of Eqs. 4.69 and 4.35, substituting these into Eq. 4.63 and ordering the terms in powers of R , one obtains:

$$\Phi(R) = -\frac{1}{12\eta^2} (P_1^2 + 3\eta^2 P_2^2) R + \mathcal{O}(R^2). \quad (4.70)$$

Reverting to dimensional variables gives Eq. 4.19.

4.8 Numerical verification

In this section the equations derived in section 4.1 are compared with finite element model calculations (FEM). Each system shown in Fig. 4.5 is modelled with ANSYS 11.0 for various crack lengths r , various slope angles θ and various material properties. The system is gravitationally loaded using the ANSYS command ACEL. For structural modelling, the element SOLID45 is used. This standard but versatile structural element supports large strain capabilities, implements 8 nodes and 3 degrees of freedom per node. The degrees of freedom in width (z -direction) are removed in order to model a plane strain situation. An isotropic and linear-elastic material model is selected. The material properties used are given in Table 4.2. The substrate and the weak layer are modelled as rigid, resulting in strain energy being stored in the slab only.

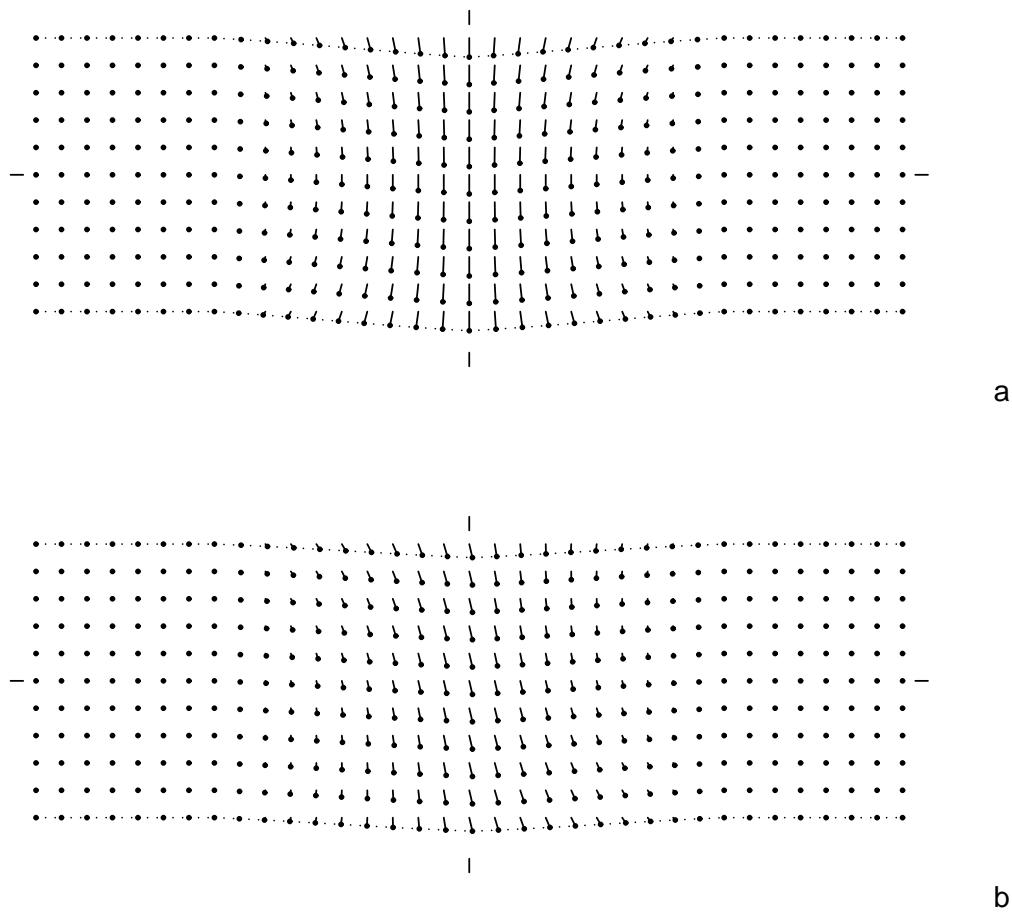


Figure 4.13: Example for displacement field in the slab, as given by Eqs 4.67 to 4.69. The four surrounding ticks show the location of the x and y axes. **a:** Slope angle $\theta = 0^\circ$. **b:** Slope angle $\theta = 45^\circ$. Data: $\rho = 200 \text{ kg/m}^3$, $E = 5.0 \text{ MPa}$, $r = h = 0.5 \text{ m}$, $p = 500 \text{ N/m}$. Magnification factor for displacement: 175, grid spacing: 5 cm.

A denser mesh is imposed at the crack tips. Mesh size was varied to ensure that significant digits of the calculation are not affected. The strain energy (ANSYS keyword SENE) is summed over all elements (using the command ETABLE), resulting in total strain energy. This value is converted to energy per unit width in z and its sign is inverted, thus representing the mechanical energy of the system per unit width (see Lawn [47], section 1.3). The calculation is run once for a system with a crack or notch of characteristic size r , and once without a crack or notch. The difference in mechanical energy between these two states is finally compared to Eqs. 4.10 and 4.13 (in which w_f is set to zero to let the crack energy become the mechanical energy).

The results are presented in Tables B.1 and B.2 in Appendix B and Figs. 4.14 to 4.16. The

Figs. 4.14 and 4.16a show that the agreement between the analytical solution and the FEM solution is very satisfactory for embedded cracks (configuration as in Fig. 4.5 a). The Figs. 4.15 and 4.16 b show that the agreement is satisfactory for notches of length $r > h$, but in general unsatisfactory for notches of length $r < h$, especially for those on the uphill side of the specimen (configuration as in Fig. 4.5 c).

Regarding experimental methods (see methods A and B, section 4.1), the comparison implies that the crack energy is more accurately estimated when applying method A (artificial crack, Eq. 4.10) than when applying method B (artificial notch, Eq. 4.13). For this reason, and because method A reflects more directly the natural situation of an embedded crack and requires no corrections to be applied for end-face orientation (such as shown in Fig. 4.6), method A is in general to be preferred to method B when the choice is available.

Table 4.2: Stratification data for examples and graphs. Poisson's ratio is $\nu = 0.2$, and $\eta = 0.98$.

Case	Figures	ρ [kg/m ³]	E [MPa]	h [m]	h_f [m]	w_f [J/m ²]	θ [deg]
a.	4.18	200	5	0.50	0.01	0.07	-
b.	4.14, 4.15	200	2	0.35	0.01	0.04	-
c.	4.17	200	5	0.50	0.001	0.07	40
d.	4.16	200	5	0.35	0.01	0.04	-

4.9 Examples

In this section the structure of the crack energy function is illustrated by a number of examples. Fig. 4.17 demonstrates the global structure of Eq. 4.10 for various fracture energies. The graph shows the variation of the critical crack length (abscissa of the maximum) and energy barrier (ordinate of the maximum) with increasing fracture energy w_f . For small values of w_f the energy barrier is reached before the crack faces make contact and the critical length remains relatively small ($r < 1.5 h$ in the example in Fig. 4.17a). For larger w_f , the crack faces make contact before the critical point of the energy barrier is reached. In this case, the critical crack lengths grow fast as w_f increases. This is indicated in Fig. 4.17a by the large increase of r_c when passing from $w_f = 0.7 \text{ J/m}^2$ to $w_f = 0.9 \text{ J/m}^2$, and from $w_f = 0.9 \text{ J/m}^2$ to $w_f = 1.1 \text{ J/m}^2$, compared to the increase of r_c when passing from $w_f = 0.5 \text{ J/m}^2$ to $w_f = 0.7 \text{ J/m}^2$ for instance.

The following numerical applications illustrate the model:

Example 1, nucleus instability: Consider a snow slope with characteristics given in Table 4.2, case a, and a substrate which is identical with the slab. Dundurs' elastic mismatch parameter α and β are then 0, and γ is 1. Applying Eq. 4.17, a pre-cracked section in the weak layer is expected to become critical if its length exceeds 23 cm. If the slab thickness were 1.5 m

instead of 0.5 m (but other parameters unchanged), the critical length would be as small as 2.5 cm. Porosity fluctuations of this size may exist in the weak layer, in which case the slope would release spontaneously. If the substrate is softer than the slab, i.e. $\alpha > 0$, the critical lengths are even smaller.

Example 2, skier instability: Consider a skier of mass 70 kg on skies of length 1.70 m, which results in a line load p of 400 N/m when the skier is moving uniformly. He/she skies a hillside sloping 40° with the horizontal. The characteristics of the slope are given in Table 4.2, case a. For simplicity the load p is assumed to act in vertical direction, i.e. $p_x = p \sin(\theta)$ and $p_y = p \cos(\theta)$. Applying Eq. 4.20, the slope is expected to be stable for skiing as long as p does not exceed 800 N/m, which represents twice the weight of the skier. If this load is exceeded, the energy barrier disappears altogether and spontaneous cracks can nucleate and propagate in the weak layer.

Example 3, gap instability: Consider the same snow slope as in the previous examples with characteristics given in Table 4.2, case a. Applying Eq. 4.22, the slope is expected to be stable against gap instability, regardless of how steep it is, because mathematically w_τ cannot exceed w_f . If however, the fracture energy of weak layer were lower by a factor of 4, reapplying Eq. 4.22 results in instability for slope angles above 44° . A similar instability would also occur if the slab thickness were 1.6-times thicker, i.e. $h = 80$ cm instead of half a metre.

Example 4, notch experiment: Consider Sigrist's experiment presented in section 2.4. Substituting the data given in Table 2.4 into Eq. 4.13 (N.B τ is positive in this case), a polynomial of degree 5 in r is obtained: $V(r) = -0.416r^5 - 0.135r^4 - 0.0115r^3 - 0.0180r^2 + 0.0692r$. The maximum of $V(r)$ is found by finding the positive real root of $\partial_r V(r) = 0$ and verifying that $\partial_{rr} V(r) < 0$. The root with the required properties is obtained for $r = 0.35$ m.

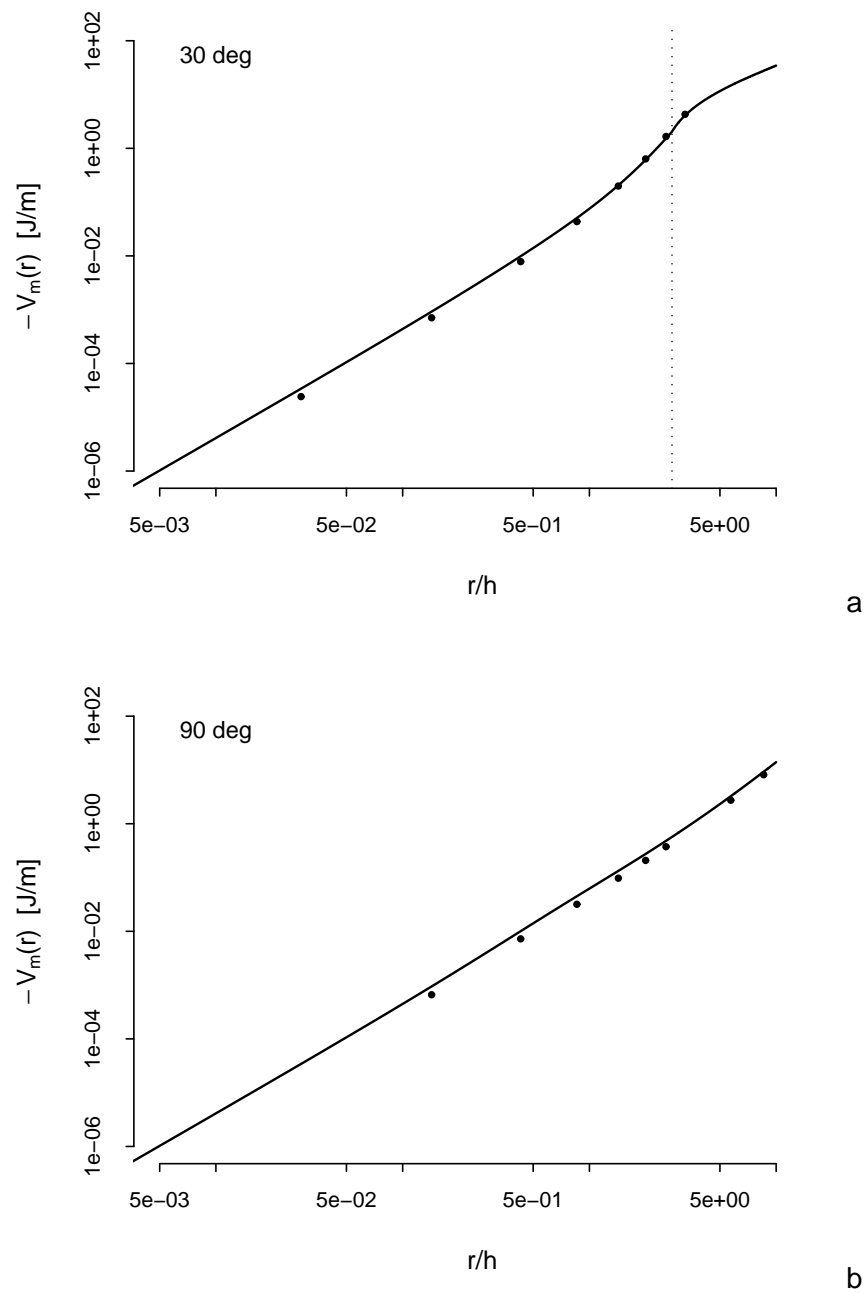


Figure 4.14: Verification of the calculation of the mechanical energy $V_m(r)$ for the case of a crack (configuration as in Fig. 4.5a). **a:** 30° slope; **b:** 90° slope (i.e. vertical). Dots: Finite element calculation (ANSYS 11.0). Full line: Eq. 4.10 with $w_f = 0$. The vertical line depicts the length of first contact. Stratification data according to Table 4.2b.

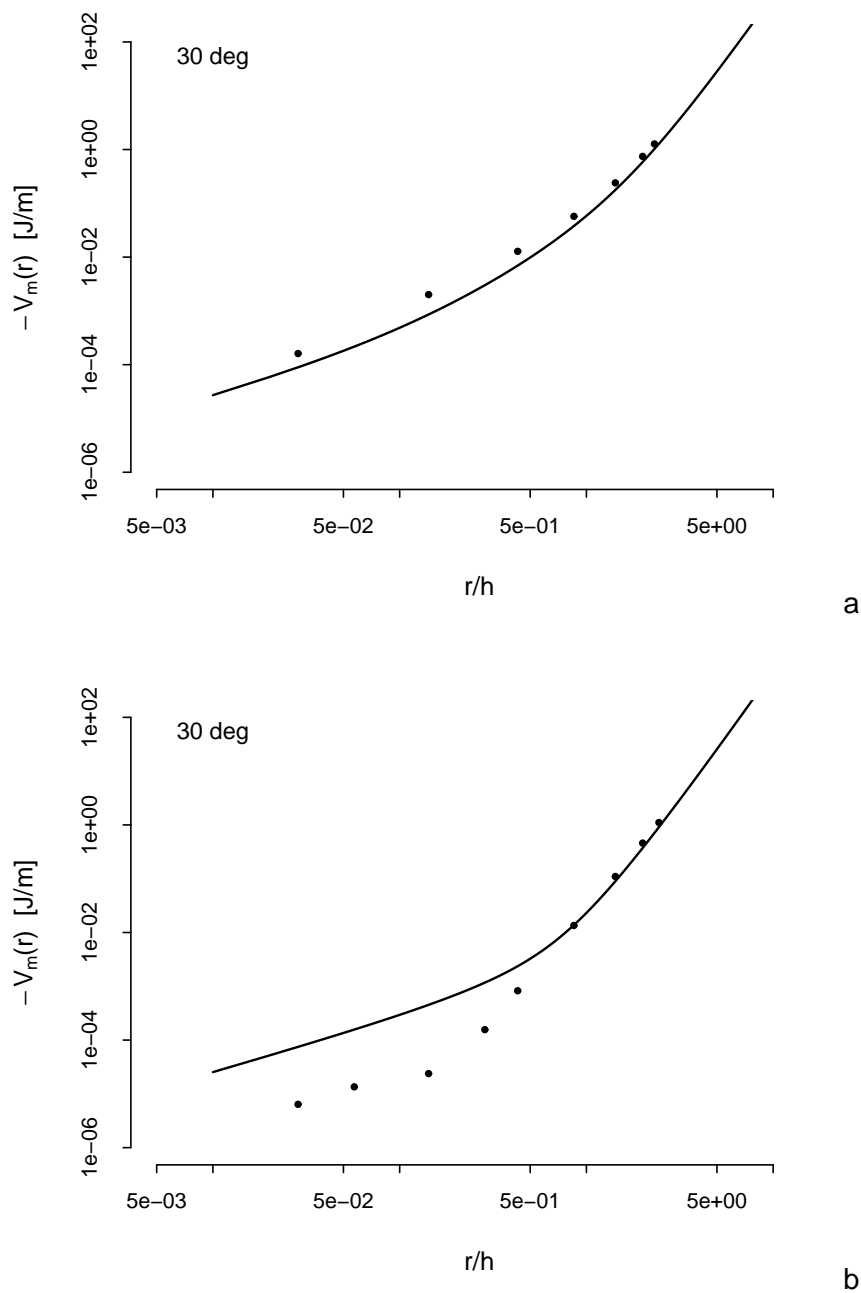


Figure 4.15: Verification of the calculation of the mechanical energy $V_m(r)$ for the case of a notch (configuration as in Fig. 4.5b and c). **a**: saw cut from lower end in uphill direction, accurate for $r \geq h$. **b**: saw cut from upper end in downhill direction, accurate for $r \geq h$ but inaccurate for $r < h$. Dots: Finite element calculation (ANSYS 11.0). Full line: Eq. 4.13 with $w_f = 0$. Stratification data according to Table 4.2b.

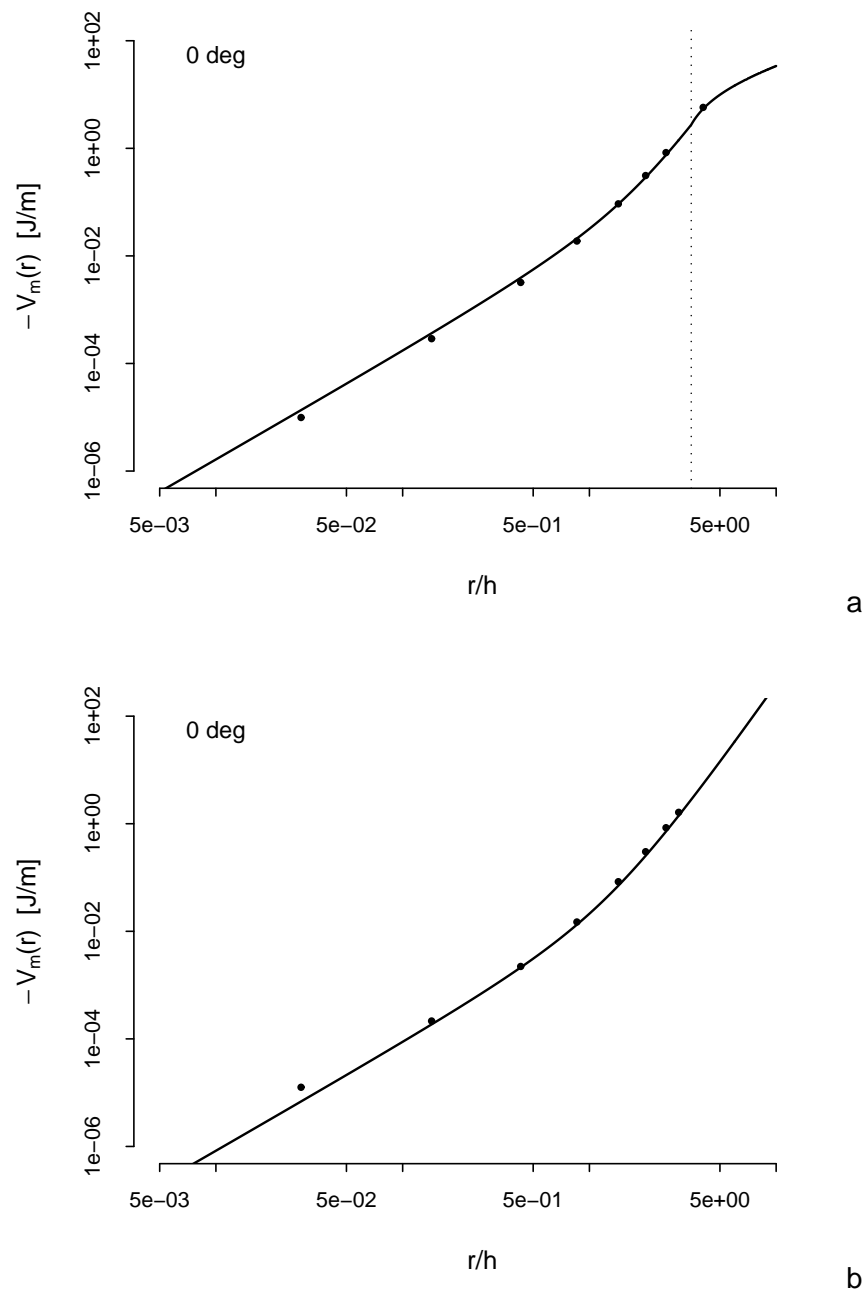


Figure 4.16: Verification of the calculation of the mechanical energy $V_m(r)$ in a horizontal snowpack. **a**: case of a crack (configuration as in Fig. 4.5a); **b**: case of a notch. Dots: Finite element calculation (ANSYS 11.0). Full line: anticrack model. The vertical line depicts the length of first contact. Stratification data according to Table 4.2d.

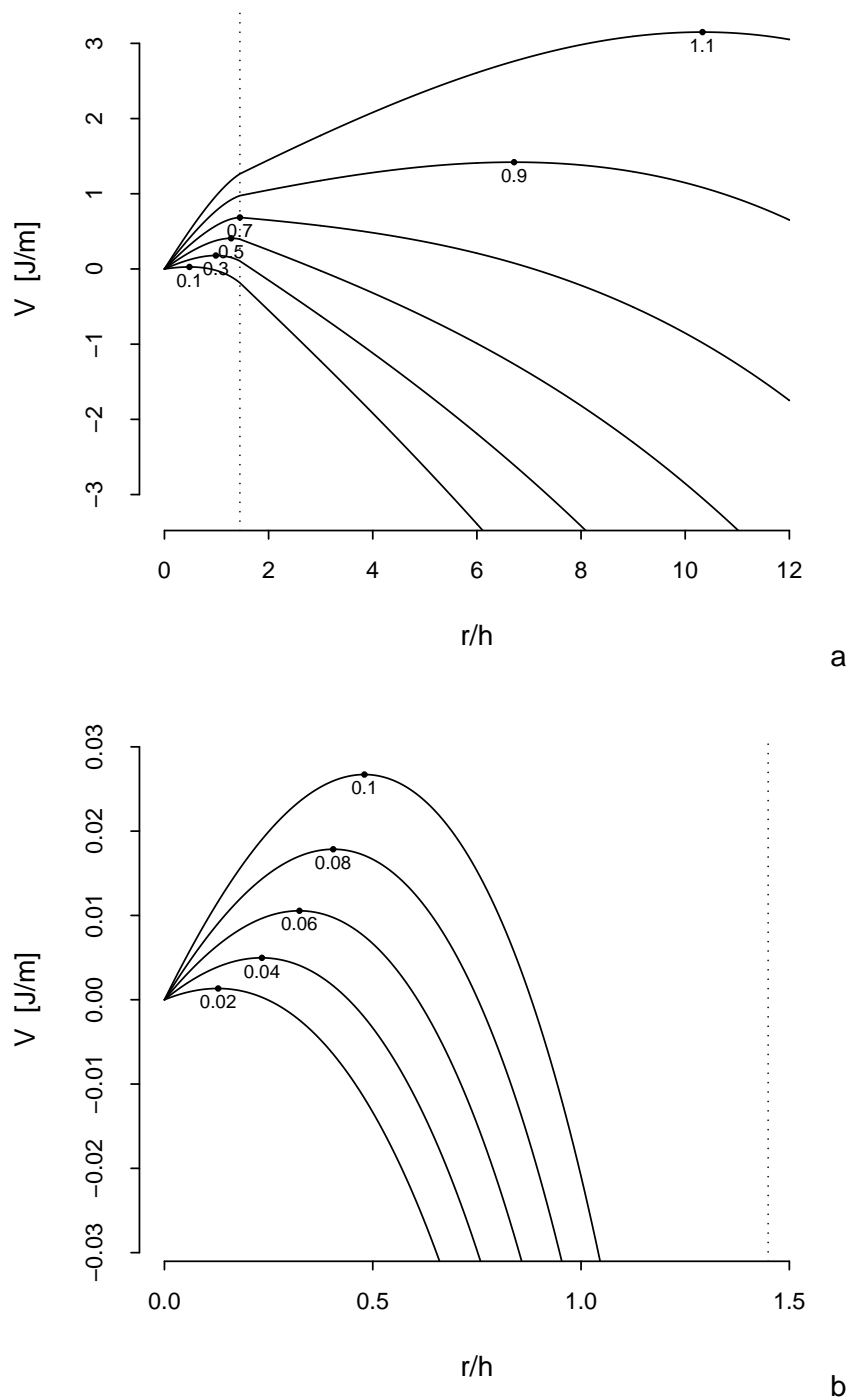


Figure 4.17: Structure of the crack energy function Eq. 4.10. Data according to Table 4.2c, with 40° slope angle. **a**: Wide range of fracture energies. **b**: Fracture energies typical of weak layers. Parameterisation: specific fracture energies w_f , shown in J/m^2 . Vertical line: tangency length, $r = l_0$. Crack-face friction coefficient after tangency: $\mu = 0.5$.

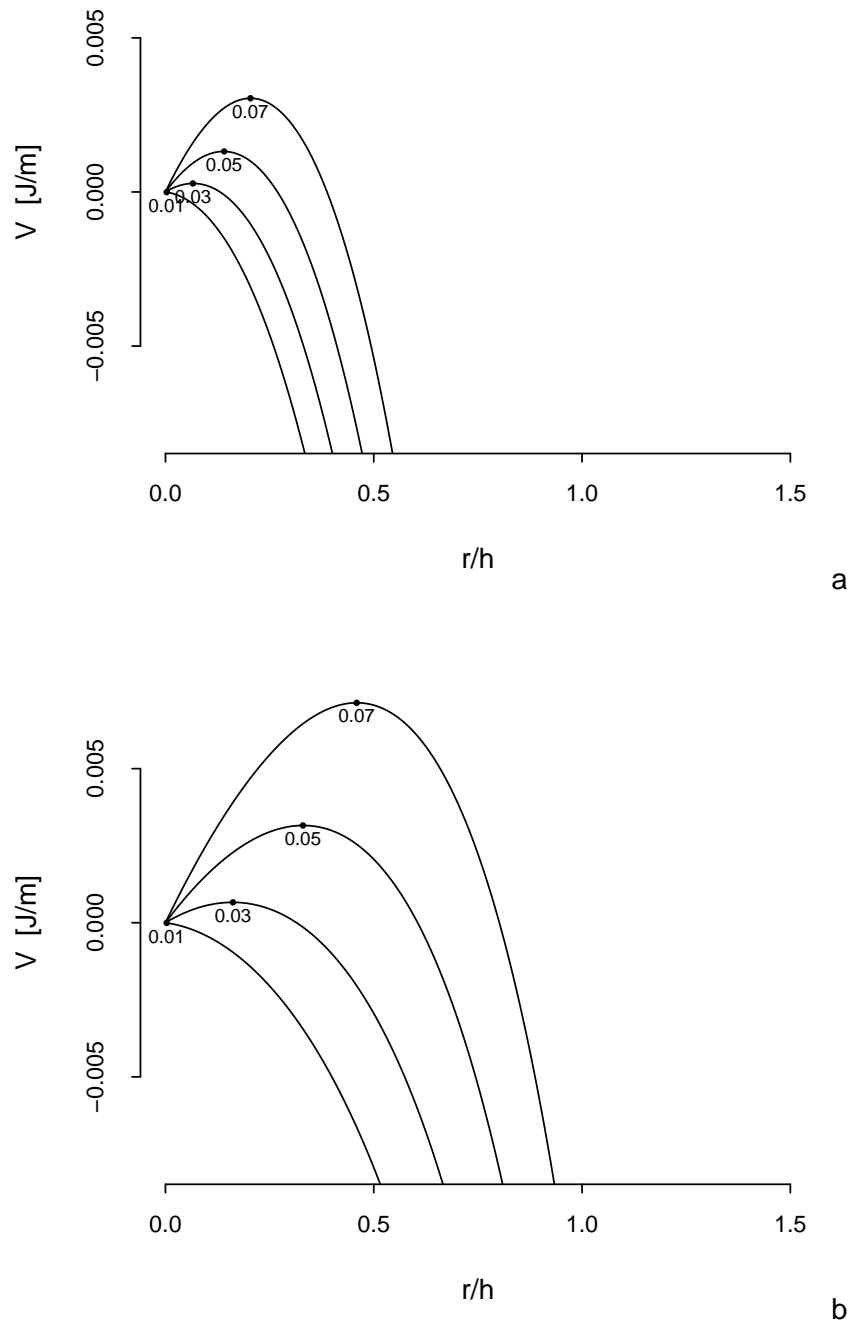


Figure 4.18: Example of the notch energy function Eq. 4.13. **a**: case of a notch sawed into the lower end. **b**: notch sawed into the upper end. Parameterisation: Fracture energies w_f typical for weak layers are shown in J/m² at the critical point of the energy barrier. Stratification data according to Table 4.2a, with 40° slope angle. Note that the energy barrier disappears for $w_f = 0.01$ J/m² (gap instability).

Chapter 5

Anticrack propagation

Once an anticrack becomes critical by crossing the energy barrier, it starts expanding and accordingly, the slab debonds and subsides. While the volume loss of the weak layer can be considered to be more or less instantaneous, the subsidence of the slab is progressive and results in a particular, time-dependent deformation field that transports the collapse event along the weak layer. This *collapse wave* is inherently non-linear and triggers the transition from a metastable state of higher energy to a state of lower energy. The volume difference between the intact weak layer and the packed debris not only determines the amplitude of the collapse, but also conditions the velocity and wavelength of the collapse wave.

5.1 Action functional for collapse waves

Unlike the nucleation of an anticrack which is essentially static before becoming critical, the propagation of a collapse wave is a dynamical process. To solve the problem according to Hamilton's principle, the saddle points of the action functional for the collapse wave must be found. As previously in chapter 4, the system is assumed to deform homogeneously in the z -direction and extensive quantities are therefore given per unit length in z . Assuming that the slab deflects as a Timoshenko beam, the action functional S can be written as follows:

$$\begin{aligned} \mathcal{S}[u_x, u_y, \psi] = \int \int \left\{ \frac{\rho h}{2} (\partial_t u_x)^2 + \frac{\rho h}{2} (\partial_t u_y)^2 + \frac{\rho h^3}{24} (\partial_t \psi)^2 \right. \\ \left. - \frac{Eh}{2} (\partial_x u_x)^2 - \frac{Eh^3}{24} (\partial_x \psi)^2 - \frac{kGh}{2} (\partial_x u_y - \psi)^2 + \tau u_x - \sigma u_y \right\} dx dt. \end{aligned} \quad (5.1)$$

In this expression, the rotational inertia is taken with respect to a neutral plane in the middle of the slab. Compared with Eq. 4.4, there are two differences. Firstly, the integration now spans

over x and t , and the field variables u_x , u_y and ψ are functions of both x and of t . Secondly, the translational and rotational kinetic energies appear in the functional (the first two terms and the third term respectively).

5.2 General asymptotic solution

In this section the differential equations for the collapse wave are established and solved. In the following h_f is assumed constant, in which case the collapse wave tends to a stationary¹ asymptotic state propagating with constant velocity c and wavelength l . There is a clear advantage in performing the calculations in dimensionless variables. In addition to those defined in Table 4.1, it is convenient to define the dimensionless wave velocity, wavelength, amplitude of the collapse wave and time:

$$C = \frac{c}{\sqrt{kG/\rho}}, \quad L = \frac{l}{h}, \quad H_f = \frac{h_f}{h}, \quad T = t \frac{\sqrt{kG/\rho}}{h}. \quad (5.2)$$

The value $C = 1$ represents a collapse wave travelling with shear wave velocity $c_s = (kG/\rho)^{1/2}$. The value $C = \sqrt{3}\eta$, where η is recalled from Eq. 4.7, represents a collapse wave travelling with longitudinal wave velocity $c_p = (E/\rho)^{1/2}$. The dimensionless wavelength L and collapse amplitude H_f are simply measured in units of slab thickness h .

The asymptotic state is searched with the Ansatz $u_x(x, t) = u_x(x')$, $u_y(x, t) = u_y(x')$ and $\psi(x, t) = \psi(x')$, where $x' = x - ct$. The operators ∂_x and ∂_t can then be replaced by $\partial_x = \partial_{x'}$ and $\partial_t = -c\partial_{x'}$. The origin of the x' -axis is chosen at the point where tangency occurs (i.e. where the crack faces make contact), and the crack front is at $x = l$ (as in Fig. 3.4). As the asymptotic state is stationary, there is no need to carry out the integration over time. The action functional in the stationary state can thus be replaced by the energy functional:

$$\begin{aligned} -\Phi[U_1, U_2, \psi] = \int \left\{ \frac{1}{2}(C^2 - 3\eta^2) (\partial_{X'} U_1(X'))^2 + \frac{1}{2}C^2 (\partial_{X'} U_2(X'))^2 \right. \\ \left. + \frac{1}{24}(C^2 - 3\eta^2) (\partial_{X'} \psi(X'))^2 - \frac{1}{2}(\partial_{X'} U_2(X') - \psi(X'))^2 \right. \\ \left. + T U_1(X') + \Sigma U_2(X') \right\} dX'. \quad (5.3) \end{aligned}$$

In the interval $[0, L]$, where no constraints apply, the Euler-Lagrange equations of the above functional are:

$$(3\eta^2 - C^2) \partial_{X'X'} U_1 = -T, \quad (5.4)$$

$$(1 - C^2) \partial_{X'X'} U_2 - \partial_{X'} \psi = -\Sigma, \quad (5.5)$$

¹Stationary in the sense of all time-derivatives becoming zero.

$$\frac{1}{12}(3\eta^2 - C^2) \partial_{X'X'}\psi + \partial_{X'}U_2 - \psi = 0. \quad (5.6)$$

For $C = 0$, X equals X' and the Euler-Lagrange Eqs. 4.27, 4.28 and 4.29 for the static case of an anticrack are recovered. For $C \neq 0$, the general solutions of Eqs. 5.4 to 5.6 in $[0, L]$ are:

$$U_1(X') = \frac{\mathbb{T}X'^2}{2(C^2 - 3\eta^2)} + C_3X' + C_4, \quad (5.7)$$

$$U_2(X') = -\frac{C_5}{\mathcal{K}^2} \cos(\mathcal{K}X') - \frac{C_6}{\mathcal{K}^2} \sin(\mathcal{K}X') + \frac{\Sigma X'^2}{2C^2} + C_7X' + C_8, \quad (5.8)$$

$$\psi(X') = \frac{1 - C^2}{\mathcal{K}} C_5 \sin(\mathcal{K}X') - \frac{1 - C^2}{\mathcal{K}} C_6 \cos(\mathcal{K}X') + \frac{\Sigma X'}{C^2} + C_7, \quad (5.9)$$

where \mathcal{K} is given by

$$\mathcal{K} = \frac{2\sqrt{3}C}{\sqrt{(1 - C^2)(3\eta^2 - C^2)}}. \quad (5.10)$$

The equation for \mathcal{K} manifests four singularities: two for $C = \pm 1$, the other two for $C = \pm\sqrt{3}\eta$. These singularities delimit three solution regimes: collapse waves with propagation velocity below shear wave speed, $|C| < 1$, between shear wave speed and longitudinal wave speed, $1 < |C| < \sqrt{3}\eta$, and above longitudinal wave speed, $|C| > \sqrt{3}\eta$. In the first and third regime, \mathcal{K} is real. In the intermediate regime \mathcal{K} is imaginary. In this case the equalities in Eqs. 5.8 and 5.9 apply to the real parts of the right hand sides, in which C_5 and C_6 are considered complex.

Ahead of the crack front, in $[L, +\infty]$, where the constraints $U_2 = 0$ and $U_1 = \psi/2$ apply, the single remaining Euler-Lagrange equations of the energy functional is:

$$\frac{1}{3}(3\eta^2 - C^2) \partial_{X'X'}\psi - \psi = -\frac{\mathbb{T}}{2}. \quad (5.11)$$

For $C = 0$, Eq. 4.30 is recovered. Denoting $\psi(L)$ by ψ^+ , the integration of Eq. 5.11 in $[L, +\infty]$ gives

$$\psi(X) = \left(\psi^+ - \frac{\mathbb{T}}{2} \right) \exp \left(-\frac{\sqrt{3}(X - L)}{\sqrt{3\eta^2 - C^2}} \right) + \frac{\mathbb{T}}{2}. \quad (5.12)$$

An analogous result is obtained in $[-\infty, 0]$ by replacing X by $-X$, L by 0 and ψ^+ by $\psi_0 = \psi(0)$. Joining the piecewise solutions in $[-\infty, 0]$, $[0, L]$ and $[L, +\infty]$, and substituting these into Eq. 5.3, results in the expression for the mechanical energy of the collapse wave. As the analytical result is very cumbersome, this step needs to be carried out numerically.

5.3 Approximate asymptotic solution

In this section, an approximate asymptotic solution for the equations derived in the previous section will be given. The solution is approximate because a few assumptions have to be made in order to obtain an analytical result. The mathematical difficulties reside in the unilateral constraint Eq. 4.1, in the singularities appearing in Eq. 5.10 and in the yet unknown rotation $\psi(L) = \psi^+$ at the crack front, and $\psi(0) = \psi_0$ at the tangency point.

The first assumption is that the collapse wave is slow compared with the velocity of a shear wave through the slab, which will later be proven self-consistently. In this case \mathcal{K} can be approximated up to a term in $\mathcal{O}(C^2)$ by

$$\mathcal{K} \approx \mathcal{K}_0 = \frac{2C}{\eta}. \quad (5.13)$$

This linearisation proves reasonably precise for values of $|C|$ up to about 1/2. Next, it is observed that the values for $|\Sigma|$ and $|T|$ are of the order of 10^{-3} or smaller in snow. This results in small rotations ψ^+ and ψ_0 , of the order of 1° or smaller. The second assumption is therefore $\psi^+ = \psi_0 = 0$. The third assumption is $\partial_X U_2(0) = 0$. This assumption is similar to the one used to obtain Eq. 4.9, with the difference that the collapse wave is not a simple translation of the tangency state, due to the inertial effects associated with propagation. The integration constants in Eqs. 5.7 to 5.9 can now be obtained:

$$C_3 = 0, \quad C_4 = \frac{1}{2} \frac{TL^2}{3\eta^2 - C^2}, \quad (5.14)$$

$$C_6 = 0, \quad C_5 = -\frac{2\Sigma L}{\eta C(1 - C^2)} \frac{1}{\sin\left(\frac{2}{\eta} CL\right)}, \quad (5.15)$$

$$C_7 = 0, \quad C_8 = -\frac{1}{2} \frac{\Sigma L}{C^3(1 - C^2)} \left[CL(1 - C^2) + \frac{\eta}{\tan\left(\frac{2}{\eta} CL\right)} \right]. \quad (5.16)$$

The boundary condition $U_2(0) = H_f$ yields the equation for the dispersion of the collapse wave. Under the condition that $\Sigma \neq 0$:

$$\frac{L^2}{C^2} \left[\frac{\eta}{L} \frac{1}{C(1 - C^2)} \Omega\left(\frac{2}{\eta} CL\right) - 1 \right] = \frac{2H_f}{\Sigma}, \quad (5.17)$$

where Ω is the function $x \mapsto 1/\sin x - 1/\tan x$. It is observed that ignoring the square bracket recovers the second relation in Eq. 3.9 up to a multiplicative constant. The right hand side $2H_f/\Sigma$ represents the square of the time for slope-perpendicular free fall (in dimensionless units).

The dispersion equation gives an implicit relation linking L with C . This implicit equation cannot be solved in closed form, but matching (C, L) -pairs can be determined with numerical methods. The structure of Eq. 5.17 is convenient in the sense that it depends only on two system properties: η and $2H_f/\Sigma$, and only one of these appears on the left hand side. The structure of the dispersion equation is shown in Fig. 5.1 for $\eta = 1$ and for a wide range of $2H_f/\Sigma$ -values. An important aspect of the dispersion equation is the convergence of the static anticrack solution and the collapse wave solution for $C \rightarrow 0$. This resolves the earlier problem of Eq. 3.9, encountered in section 3.2.2, which did not contain this limit.

The remaining step is to find the (C, L) -pair(s) for which the energy functional Φ is in a saddle point. This is obtained by substituting the expressions for U_1, U_2 and ψ into Eq. 5.3 and carrying out the integration numerically. The procedure is then as follows: Choose a value of C between $-1/2$ and $1/2$, and find the associated value L by solving the dispersion equation Eq. 5.17. With L and C known, compute Φ by numerical integration of Eq. 5.3. Repeat the procedure for other values of C and find the (C, L) -pair(s) for which $\Phi(L, C)$ is stationary. Formally, the procedure

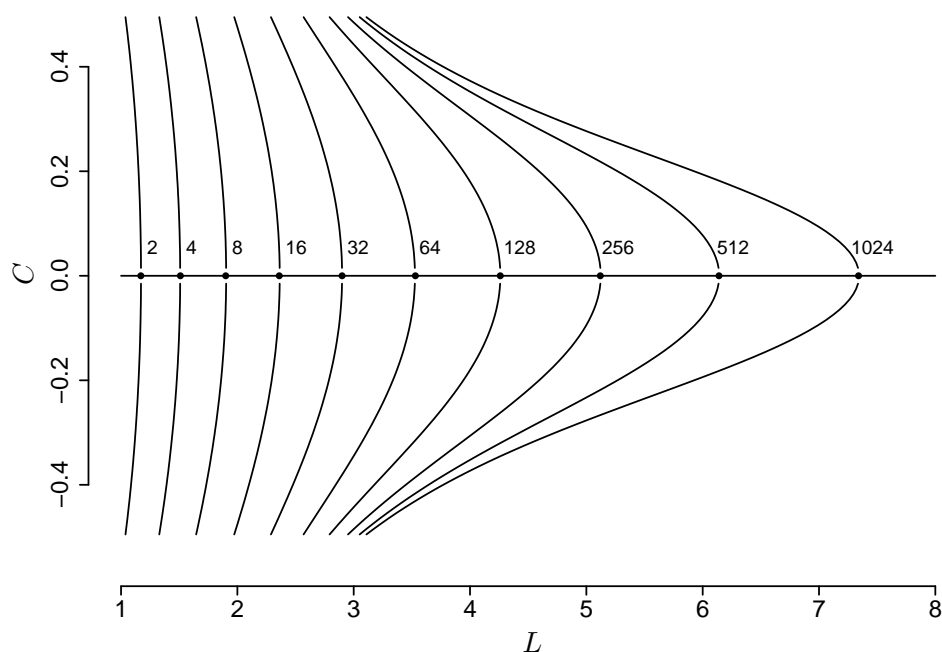


Figure 5.1: Dispersion of slow collapse waves for $\eta = 1$ (equivalent to a Poisson solid) and values for $2H_f/\Sigma$ ranging from 2 to 1024, all possible in snow. The dots on the L -axis represent the tangency lengths L_0 of the static anticrack solution, root of $L_0^2[1 + \frac{1}{3}L_0^2/\eta^2] = 2H_f/\Sigma$. (N.B. this equation is different from Eq. 4.48, because $\psi^+ = \psi_0 = 0$ are imposed.)

can be written:

$$\text{find } C \in \left[-\frac{1}{2}, +\frac{1}{2}\right] \quad \text{such as} \quad \frac{d}{dC} \Phi(L(C), C) = 0, \quad (5.18)$$

where the $L(C)$ is obtained from solving Eq. 5.17. The restriction $|C| \lesssim \frac{1}{2}$ is necessary because \mathcal{K}_0 was used instead of \mathcal{K} to determine the integration constants C_5 to C_8 .

5.4 Example

Fig. 5.2 gives an example of the procedure 5.18. The data is taken from an experiment that will be encountered later in section 6.1.1. The graph shows three saddle points of Φ , each representing a physically admissible solution. The first saddle point occurs for $C = 0$. The associated wavelength is $L = 3.94$ and this solution corresponds to the static case of an anticrack. The other two saddle points occurs for $C = \pm 0.25$. The associated wavelength is $L = 3.55$ and these solutions corresponds to the dynamic case of a propagating collapse wave. Note that the $C = 0$ solution, which represents a supercritical (i.e. unstable) crack, corresponds to a maximum of the dynamic action functional whereas the propagating solutions at $C = \pm 0.25$ minimise the action functional. Note also that the result $C = \pm 0.25$ for stationary propagation justifies the neglecting of $\mathcal{O}(C^2)$ terms in Eq. 5.13.

Reverting to dimensional quantities using Eq. 5.2 and Table 4.1, the collapse wave travels with a propagation velocity c of 26 m/s and with a wavelength l of 1.6 m.

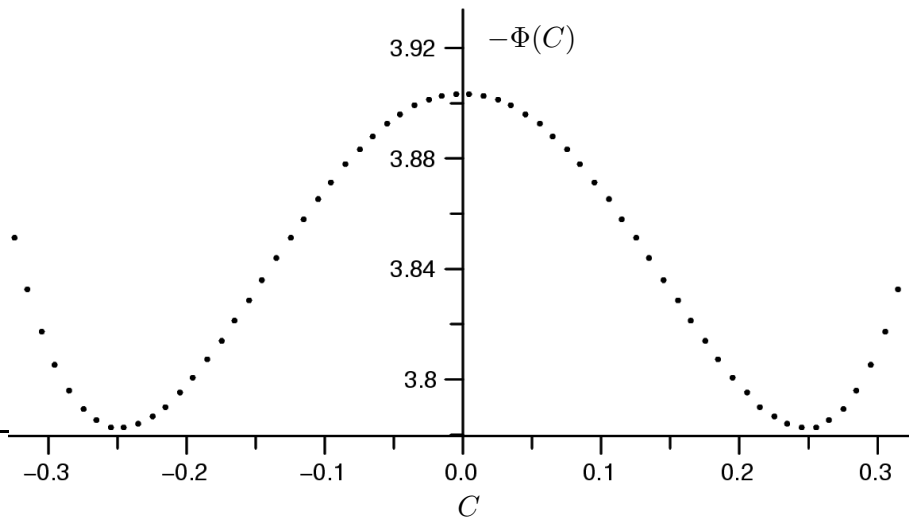


Figure 5.2: Example of numerical determination of the saddle points of Eq. 5.3. Data: $\rho = 247$ kg/m³, $E = 8.0$ MPa, $\nu = 0.25$, $h = 0.44$ m, $h_f = 0.8$ cm and $\theta = 19^\circ$. The $2H_f/\Sigma$ -value is 96.

Chapter 6

Discussion

In chapters 4 and 5 the formation and propagation of mixed-mode anticracks in weak subsurface layers was examined. Physically, for an anticrack to materialise the weak layer must be composed of a sparse aggregate of ice grains. As this aggregate fails, the fracture debris packs more tightly and the weak layer undergoes a reduction in volume. Consequently the support of the slab is lost over the length of the anticrack and the stress field vanishes on its boundary. The momentary absence of compressive stress in the fracture debris reduces Coulomb-type friction to nil. As the opposing anticrack faces make contact, Coulomb-type friction reappears. Mathematically, the granular structure of the weak layer was neglected. The fracture region was modelled in the continuum as a mixed-mode anticrack, that is, as two free surfaces in the interface. Using different approaches for short, intermediate and long cracks, the crack energy function $V(r)$ was obtained for cracks length from the order of centimetres to virtually infinity.

6.1 Model validation

6.1.1 Experiments

In order to investigate whether or not fracture in weak snowpack layers displays the characteristics predicted by the anticrack model, van Herwijnen recorded a number of PST-type notch experiments at two sites in Davos, Switzerland using a high-speed video camera [81, 82]. One site was located in Davos Stilli, altitude 1560 m, the other in Davos Wannengrat, altitude 2400 m. The snow blocks for the experiment were made between 3 m and 4 m long. On the surface facing the video camera, black markers were applied at regular intervals, both above and below the weak layer (Fig. 6.1). The slab thickness was doubled by shoveling loose snow on top of the natural slab a few hours before isolating the block. The weak layer was then notched with a snow saw from the lower end. The trajectory of the markers during the fracture process show the displacement field of the snow around the fracture area. Fig. 6.2 shows the superposition

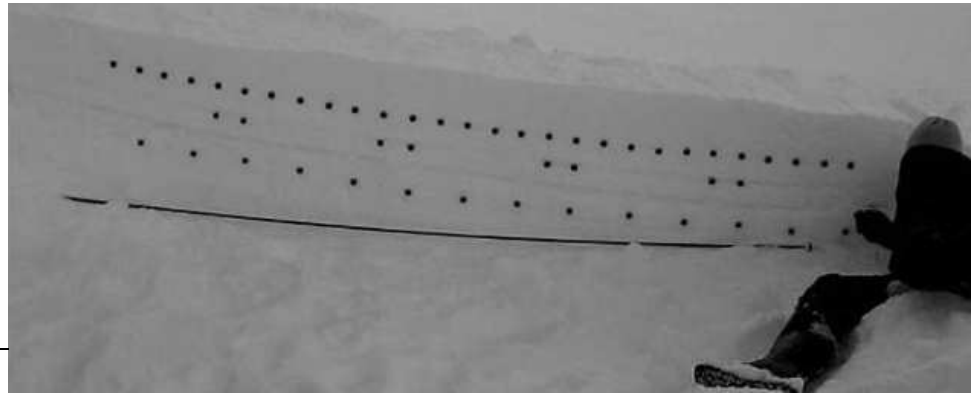


Figure 6.1: Davos-Stilli experiment: Single video frame taken immediately before the notch length r became critical. The operator is notching into the weak layer with a snow saw ($r_c = 19(2)$ cm). The weak layer is between the lower two rows of markers. Video: van Herwijnen.

of successive video frames from the Davos Stilli experiment and details are shown in Fig. 6.3. The progressive subsidence due to the failure of the weak layer is visible on the superpositions. The sequence of images indicates that the slab subsides first, then slips and finally comes to a rest. This is confirmed in more detail in [82]. The observed failure sequence is not a simple mode II fracture, but an anticrack with -in this case- a very small mode II component. Notably, substantial slip occurs only after the collapse wave has crossed the entire sample (i.e. when it is entirely detached from its support). The markers below the weak layer (row C in Fig. 6.2) do not move, or move by less than 0.1 mm during the entire fracture process. This shows that the substrate remains essentially unaffected by the events. The weak layer in this experiment consisted of buried surface hoar and one might think that the observed sequence of events is restricted to this type of weak layer. In fact, this is not the case: the same qualitative results have been observed on weak layers composed of faceted snow [81, 82].

Experimental evidence distinguishing between the anticrack model and the simple shear model has been provided by Gauthier and Jamieson [25]. Using notch experiments of the PST-type (see section 2.4), they show that the critical notch length depends weakly on slope angle. These experiments were discussed in section 2.4 and the results listed in Table 2.3. Using this data, the Young's modulus E is estimated using Eq. 2.1. The fracture energy w_f is estimated by taking the mode of the fracture energy distribution shown in Fig. 2.3, resulting in a value of $w_f = 0.03$ J/m². In the 24-01-2006 experiment, the critical notch lengths were found to increase slightly with increasing slope angle (0° , 30° and 38°). The dependence is shown in Fig. 6.4. The two model curves on the same graph show the theoretical results predicted by the simple shear model [53] and the anticrack model. The results for the shear model are obtained by applying Eq. 3.2. The results for the anticrack model are obtained by applying Eq. 4.13. This is done as follows: By substitution of the values of τ , σ , E , η , w_f and h into Eq. 4.13, a polynomial $V(r)$

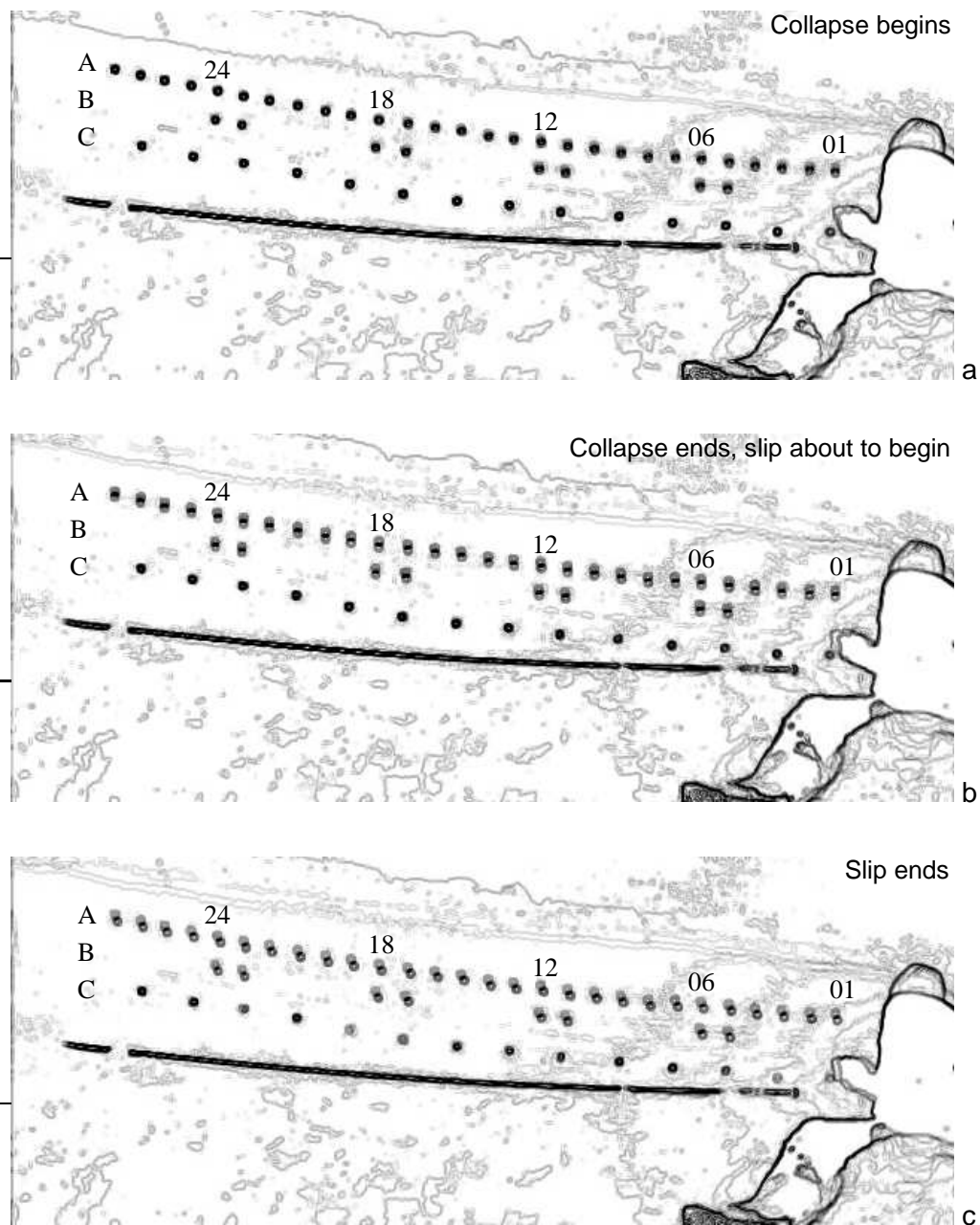


Figure 6.2: Davos-Stilli experiment: Superposed contour plots extracted from successive video frames. **a**: superposition of frames at $t = 0.00$ s and $t = 0.08$ s. **b**: $t = 0.00$ s and $t = 0.16$ s. **c**: $t = 0.00$ s and $t = 0.24$ s. N.B. $t = 0$ is the time of the last frame before the crack turns critical.

of degree 5 and real coefficients is obtained. The saddle point is determined by finding the positive real root of its derivative. This root is the critical crack half-length r_c . Fig. 6.4 shows that the simple shear model presents a singularity for $\theta \rightarrow 0$ and that the general trend of the measurements is not reproduced by this model. The anticrack model, by contrast, reproduces

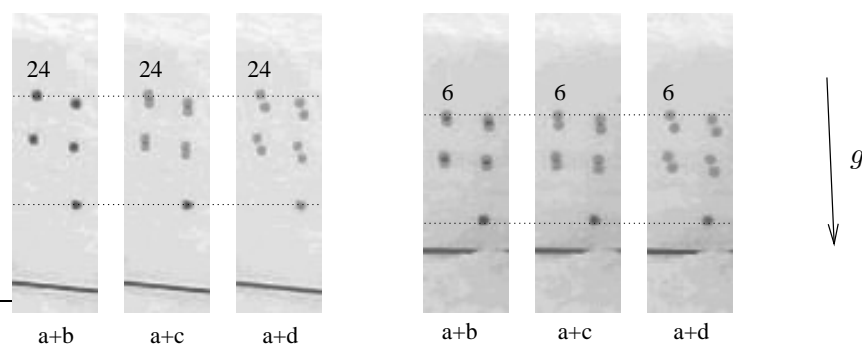


Figure 6.3: Davos-Stilli experiment: Details of the superposition of video frames, at markers 6 and 24 (see Figs. 6.1 and 6.2). a+b: superposition of frames $t = 5.60$ s and $t = 5.68$ s. a+c: superposition of frames $t = 5.60$ s and $t = 5.76$ s. a+d: superposition of frames $t = 5.60$ s and $t = 5.84$ s.

the measurements and especially the general trend in a very satisfactory way. This indicates that the anticrack model not only delivers better precision than shear models but also gives a better understanding of the fundamentals of weak layer failure.

A detailed experimental test case has been provided by Sigrist and Schweizer [69]. In this experiment, of the type shown in Fig. 2.4, all material properties necessary to apply the anticrack model have been measured, including Young's modulus (Table 2.4). The mean critical cut length obtained in 21 field experiments on a 30° slope amounted to $r_c = 23$ cm ± 2 cm. Using the material properties given by Sigrist and listed in Table 2.4, and applying the anticrack model Eq. 4.13 as above, the model predicts a critical crack length of 35 cm ± 5 cm (see example 4 in section 4.9). However, this is not the cut length measured by Sigrist: In his experiment the edges of the sample were vertical, while in Eq. 4.13 the edges are assumed slope-normal. One can account for the difference by adding $\pm(h/2) \tan \theta$ to r_c (see Fig. 4.6). In Sigrist's case the correction is -8 cm and therefore the value to compare with Sigrist's average cut length is $r'_c = 27$ cm ± 5 cm. This is indeed close to Sigrist's measured 23 cm ± 2 cm. In snow science, where uncertainty is often large, this degree of agreement is very satisfying. By comparison, the simple shear model [53] predicts $r'_c = 2.0$ m ± 0.3 m for the same parameters, which is too large by one order of magnitude.

The Davos Wannengrat experiment provides measured data for a first validation of the collapse wave calculation [81, 82]. The theoretical estimation of the propagation velocity is carried out as explained in chapter 5 using the field data presented in Table 6.1 I (see also section 5.4 for further details). The results of this calculation are compared with the measured velocity in Table 6.1 II. In the experiment, after slowing down from initially 35 m/s, the collapse wave reached a stationary state in the middle of the specimen [81, 82], attaining a constant speed of 20 m/s ± 4 over a length of 1 m. Then, approaching the opposite end of the specimen the velocity increased again to reach a final 40 m/s. The stationary velocity of 20 m/s ± 4 m/s observed in the Wannengrat experiment compares favourably with the calculated asymptotic velocity of 26 m/s

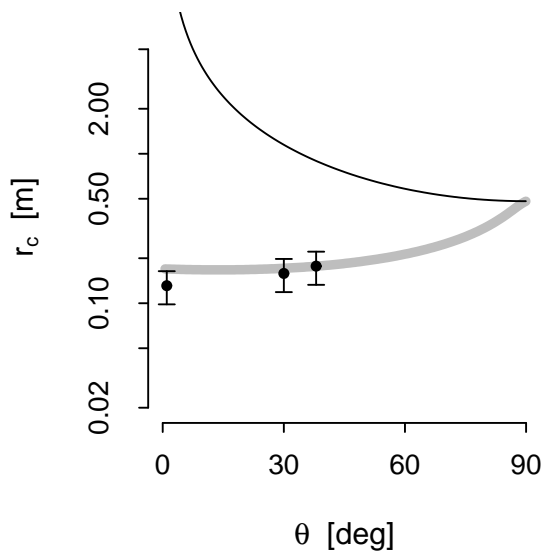


Figure 6.4: Comparison of model calculations and experimental results. Critical crack length versus slope angle. Squares: PST experiment [25]. Gray line: anticrack model; black line: simple shear model according to McClung [53]. Material properties as in Table 2.3.

± 5 m/s. Other models of fracture speed [4, 55, 56] predict much higher propagation velocities of the order of 100 m/s to 1000 m/s [4] or have no theoretical justification [55, 56].

In summary, the results discussed in this section indicate that the anticrack model captures the essential physics of the fracture process of a weak, collapsible layer. Simple shear models on the contrary conflict in many ways with the experimental evidence. This is not to say that simple shear fracture never occurs in snow. It probably applies under circumstances when the fracture plane is strictly not collapsible, e.g. in the case of very compact layers of snow.

Table 6.1: Validation of collapse wave model. **I.** Material properties for van Herwijnen's PST experiments according to [82]. The Young's modulus is estimated according to Scapozza's model Eq. 2.1. **II.** Comparison of calculated velocity (c_{cal}) and measured velocity (c_{obs}).

I. Data	ρ [kg/m ³]	E [MPa]	ν [-]	h [m]	h_f [m]	θ [°]
Davos Wannengrat, 2/2008	247	8(4)	0.25	0.44	0.008	19

II. Results	L	l [m]	C	c_s [m/s]	c_{cal} [m/s]	c_{obs} [m/s]
Davos Wannengrat, 2/2008	3.55	1.6	0.25	104(25)	26(5)	20(4)

6.1.2 Phenomenology

In this section the qualitative predictions of the anticrack model are compared with the empirical knowledge on avalanche triggering that has accumulated during decades of snow research and terrain experience. The phenomenology has been related in sections 1.1, 2.1 and 2.2.

First the correlation of slab avalanche and whumpf events is inspected. From the point of view of simple shear models, which do not account for volumetric changes during fracture, whumpfs in horizontal terrain are viewed as an unrelated, different type of phenomenon and consequently the correlation with slab avalanches is fortuitous. In the anticrack model, the underlying process is the same. The essential difference between slab avalanches and whumpfs resides in the amount of crack-face friction and slope angle. A whumpf can simply be regarded as an incompleting slab avalanche which does not slide, due to friction forces between the crack faces which retain the delaminated mass of snow. This underlines the linkage between the occurrence of whumpfs and slab avalanches.

Experienced back-country skiers are aware that slab avalanches can be remotely triggered from adjacent flat ground or from across a slope. This is a natural consequence of the two-stage scenario implied by the anticrack model (see section 4.1), in which the propagation of the anticrack and the frictional sliding of the slab are decoupled. As the compressive component of stress σ never vanishes in skiable slopes, energy for crack propagation is available on slopes of any angle, including horizontal terrain. Therefore, anticracks can propagate into, across and out of zones where a net shear stress is absent, i.e. where $\tau - \tau_T = 0$ (or in other terms where slope angle is smaller than friction angle). Practically this means that anticracks can climb or descend slopes, and pass a rounded ridge. Simple shear models, in which a one-stage scenario is implicit (fracture can propagate if and only if crack-face friction is overcome by gravity), are unable to account for remote triggering. The simple shear crack has not the ability of the anticrack to cross zones of zero net shear stress, in which the slab does not slide after the passage of fracture.

As long as the collapsible layer and the slab extend in space, as long as the slab can transmit strain energy and as long as the release of gravitational potential energy is sufficient to overcome the resistance to fracture, the collapse wave is energetically self-sustained and can travel over long distances. This has indeed been reported in some instances [14, 39, 79]. In other instances, whumpfs were arrested after travelling a few metres or decametres, sometimes leaving a clearly visible perimeter fracture (Fig. 2.1). Thus it seems that there are circumstances where the slab can transmit collapse waves and other circumstances where it can not do so, or do so only over limited distances. The arrest of the collapse wave could be due to the presence of flaws in the slab. Transverse failure may result when the collapse wave hits a flaw. In this case some or all of the energy transported by the collapse wave is dissipated. The knowledge under which circumstances the slab material is able to transmit a collapse wave and under which circumstances it is not, could be a major step in understanding and predicting avalanche haz-

ard [26]. Experience indicates that there may be only a limited time-window in which a slab is able to propagate a collapse wave. One would certainly like to know more about the conditions that determine the beginning and the end of that time-window.

6.2 Scaling relations

In chapter 4 crack energy was shown to be a function of crack half-length r , normal stress σ , shear stress τ and, when crack faces are in contact, resultant shear stress τ_f (N.B. $\tau_f = \tau - \tau_r = \tau + \mu\sigma$ if $\tau + \mu\sigma \geq 0$ and zero if not). The scaling behaviour of the crack energy V as a function of σ and τ is now considered. As mentioned in section 3.1.4, the mechanical energy of simple shear cracks always scales as

$$V_m \propto \tau_f^2. \quad (6.1)$$

The index f appears because the slip surfaces in a mode II crack are always in contact. The mechanical energy of mixed-mode anticracks scales as

$$V_m \propto \begin{cases} \tau^2 + \sigma^2, & r \ll h, r < l, \\ \tau^2 \oplus \sigma^2, & r \gtrsim h, r < l, \\ \tau_f^2 \oplus \sigma \oplus 1, & r > l, \end{cases} \quad (6.2)$$

and that of notches, prior to contact, scales as

$$V_m \propto \begin{cases} \tau^2 + \sigma^2, & r \ll h, \\ \tau^2 \oplus \sigma\tau \oplus \sigma^2, & r \gtrsim h. \end{cases} \quad (6.3)$$

The summation symbol \oplus indicates a linear combination (summation after multiplication of the operand by a constant determined by the theory). In simple shear models, $\tau_f = 0$ implies $V_m = 0$. In the anticrack model, by contrast, neither $\tau = 0$ nor $\sigma = 0$ imply $V_m = 0$. Indeed, if $\tau = 0$, then necessarily $\sigma \neq 0$ and V becomes a function of σ alone, with $V(\sigma) \neq 0$; while if $\sigma = 0$, then necessarily $\tau \neq 0$ and V becomes a function of τ alone (or τ_f), with $V(\tau) \neq 0$ (or $V(\tau_f) \neq 0$, unless $\tau_f = 0$). Physically, this means that in absence of resultant shear stress there is still energy available for crack growth from the anticrack mechanism.

Despite van Herwijnen's experimental results [83], speculations re-emerged in recent years that shear fracture always precedes collapse [55, 56]. In fact this egg-or-hen question makes little sense. At grain-scale the random aggregate of ice grains fractures in a random combination of microscopic modes. At larger scales, the scaling relations indicate that both shear and compression contribute to crack energy and therefore to fracture energy. The relative contributions of shear mode and anticrack mode to crack energy, as the crack expands from nil, can be calculated. At nucleation time, $r \ll h$, the partitioning of the crack energy (the shear contribution

divided by the anticrack contribution to crack energy) is $\tau^2 : \sigma^2$ or equivalently $(\tan \theta)^2 : 1$. In a slope of 30° for example, the ratio is 1 : 3, i.e. there is 25 % energy contribution by the shear mode and 75 % by the anticrack mode. At 45° the partitioning is 1 : 1, or even. For larger cracks, the relative contribution of the anticrack mode increases until contact between the crack faces is established (Eq. 4.5). After contact it decreases and, for very long cracks and for $\tau_f \neq 0$, the partitioning asymptotically approaches 1 : 0, characteristic of simple shear. However, Eq. 4.9 does not describe a shear crack unless $h_f = 0$. The anticrack contribution in σ never vanishes, and for $\tau_f = 0$ it is the only one to provide energy.

It is also possible to compare a small shear crack and a small mixed-mode anticrack, both of equal size, by computing the ratio of the crack energy of the first with respect to the crack energy of the second. For the shear crack, the crack faces are always in contact, which gives rise to Coulomb friction with coefficient μ . For the mixed-mode anticrack, zero Coulomb friction prior to contact applies (due to the absence of compression of the crumbled weak layer). The ratio of crack energies (simple shear crack energy divided by mixed-mode anticrack energy) is then $\tau_f^2 : (\tau^2 + \sigma^2) = (\tau + \mu\sigma)^2 : (\tau^2 + \sigma^2) = (\sin \theta - \mu \cos \theta)^2 : 1$. With $\mu = 0.4$ this amounts to about 1 : 42 in a 30° slope and to about 1 : 9 in a 40° slope. This indicates that mixed-mode anticracking contributes considerably more energy (90 % and more) than simple shear cracking.

6.3 Discussion of model assumptions

The fact that volumetric collapse of weak layers does take place during fracture has been shown by van Herwijnen and Jamieson in field experiments [80, 83]. These experiments comprised the most common types of weak layers (buried surface hoar, depth hoar and faceted crystals) and different triggering mechanisms (rutschblock tests, notch experiments and skier triggering). Their results indicate that anticracking frequently if not always takes place in weak snowpack layers. van Herwijnen's experiments also demonstrate that shear fracture and collapse of the weak layer occur simultaneously when fracture is initiated [82]. This refutes conjectures that shear fracture is always first in the formation of slab avalanches.

A number of assumptions were made to obtain the crack energy function: (1) a continuum crack, (2) brittle fracture, (3) a one-dimensional plane strain configuration and a rigid substrate, (4) homogeneous and isotropic layers of snow, (5) a fracture energy that is independent of fracture mode and (6) negligible dissipation. These assumptions are discussed in this order below.

1. The continuum equations have no knowledge of the randomness of the snow structure at grain-scale (0.2 mm to 5 mm) and are not applicable at this resolution. In its present formulation, the model has no information on small-scale flaws that are always present because of the disordered and strongly heterogeneous microstructure of snow on the sub-centimeter scale. The model only knows of the explicit crack modelled as a boundary condition. In particular, the

following situations are not accounted for: (i) Screening of the stress field in the vicinity of the explicit crack, e.g. in presence of multiple weak layers. (ii) Arrest of fracture propagation, due to transverse cracks as shown in Fig. 1.2. (iii) Crack nucleation by interaction and coalescence of many small-scale flaws within the same layer.

2. It has been argued that snow is a quasi-brittle material. Accordingly, models of snow failure should take into account the existence of a fracture process zone of finite extension around the crack tip. This is typically modelled in terms of a displacement-softening slip surface characterised by a peak strength τ_p , residual friction stress τ_r and characteristic softening displacement δ [53]. Such displacement softening relationships can be used as an 'input' for finite element simulations using cohesive crack models [5]. Analytical results derived from cohesive crack models are obtained in the limit where the fracture process zone is small in comparison with the system dimensions (see explicitly [53, 59]). This is simply the limit of linear-elastic fracture mechanics (LEFM), and the expressions obtained are identical to those obtained from LEFM if one identifies the fracture energy w_f with the product $(\tau_p - \tau_r)\delta$. In particular, it can be easily shown that the present model yields the same results as the 'classical' cohesive crack models if one considers the case of pure shear. It was shown in section 4.3 that, in the absence of volume reduction, the model recovers McClung's propagation criterion (Eq. 3.2 in this text or Eq. 3 of [53]). Hence, the fact that the present model uses a LEFM formulation from the very beginning does no more (and no less) harm than the assumptions used by other authors to extract analytical fracture criteria from a more general quasi-brittle treatment.

3. In the model calculation a one-dimensional plane strain configuration and, except for short cracks, a rigid substrate were assumed. The critical crack size r_c and the critical line charge p were obtained for these configurations. The one-dimensional configuration underestimates r_c and p when compared with a two-dimensional, circular crack. The assumptions of plane-strain deformation and rigid substrate as well as the Timoshenko formalism overestimate r_c and p .

4. A homogeneous isotropic slab, and a homogeneous weak layer and substrate were assumed. In reality, all material properties of snow are stochastic functions of space. The randomness of material properties such as the fracture energy w_f implies a certain likelihood of precursor zones for fracture nucleation. Inhomogeneous material properties and geometry also affect the response of the slab to bending, stretching and compression, which in turn affects the energy barrier. Whenever random variables are involved, some events depend more on average properties of the distributions, other more on the tails of the distribution. Those affected by the tails (e.g. nucleation and arrest) are probably less accurately modelled than those depending more on average values (e.g. propagation).

5. A key parameter in the calculations is the fracture energy w_f , which is defined without specifying whether failure occurs under shear, compression, or mixed mode loading. This implies the assumption that the energy difference between the states of the weak layer before and after failure does not depend on the combination of macroscopic loading modes. While it is possible but not proven that the toppling of individual depth hoar crystals in slope-parallel shear may require

less energy than their vertical crushing, the situation is altered by the fact that, in a strongly heterogeneous and random material such as snow, loading is locally always in mixed mode, which reduces the anisotropy in w_f . Therefore it is plausible to expect little mode dependence of fracture energy. If this proves wrong in practice, w_f can be made a function of θ , but Fig. 6.4 does not indicate that this is necessary.

6. Dissipative terms were neglected in the formulation of mechanical energy. Dissipation of energy may for example increase the critical loads p a skier can apply dynamically to the snowpack before it fails. Dissipation may also play a role in the ECT-type experiments proposed by Simenhois and Birkeland [72] in which tapping on the upper surface of a field specimen induces the fracture in the weak layer. Until now, the experiments of Johnson, van Herwijnen, Sigrist and Gauthier [25, 40, 69, 83] can be explained without including dissipative terms other than crack-face friction.

6.4 Interpretation of the anticrack model

In order to investigate how the anticrack model affects the understanding of avalanche hazard, its predictions are compared with those of the simple shear model in an ideal situation. The comparison is illustrated on the concrete example of a snow cover with physical properties as listed in Table 6.2. Local variations of snowpack properties such as wind-deposits are disregarded. Instead, the spatial distribution of slab thickness h is assumed of the form $h = h_0 \cos \theta$, where θ is the slope angle and h_0 is a constant. This corresponds to an idealised snow cover in which snow is deposited vertically during snowfall (in the concrete example the slab thickness is 0.50 m in a slope of $\theta = 40^\circ$). The weak layer is supposed to extend throughout the snow cover. Immediately after fracture, the debris of the weak layer is assumed to oppose Coulomb type friction to slab motion (crack-face friction). In order to illustrate the influence of friction, a coefficient of $\mu = 0.5$ is assumed, a value proposed by Fyffe [20] and compatible with friction coefficients $\mu > 0.4$ measured by Casassa [11].

Fig. 6.5 shows critical crack half-lengths calculated with the simple shear model [53] and with the anticrack model (Eq. 4.10) as a function of slope angle. The graphs show that the predictions of both models are similar for very steep slopes near 90° , for which the simple shear model and mixed-mode anticrack model converge as $\sigma \rightarrow 0$. For lesser slope angles however, the predictions of both models differ considerably.

Table 6.2: Snowpack properties for the example discussed in this section (symbols: see text).

ρ [kg/m ³]	E [MPa]	ν	η	h_0 [m]	h_f [m]	w_f [J/m ²]	μ	θ [°]
200	5.0	0.2	0.98	0.65	0.01	0.07	0.5	0 – 90

The simple shear model (black curve in Fig. 6.5) divides the terrain into slopes in which fracture can be triggered and slopes in which it cannot, depending on the friction angle $\theta_\mu = \arctan \mu$. Untriggerable slopes are characterised by $\theta \leq \theta_\mu$ where critical crack sizes r_c do not exist. Triggerable slopes are characterised by $\theta > \theta_\mu$, where the critical crack size r_c is finite. With increasing slope angle the critical crack length rapidly decreases, increasing the odds to trigger failure. In the present example (see Table 6.2) the simple shear model predicts a critical crack length of 17 m in a slope of 30° and of 4.6 m in a slope of 40° for a crack-face friction coefficient of $\mu = 0.5$.

The anticrack model (grey curve in Fig. 6.5) does not divide the terrain into slopes in which fracture can or cannot be triggered: Except for vertical terrain, the critical crack size r_c is always finite. Given the existence of a collapsible weak layer, triggering a propagating crack is possible on all slopes, resulting in a whumpf, a slab avalanche or a remotely triggered slab avalanche if propagation is not arrested underway. The critical crack length to cross the energy barrier is in fact minimal in the horizontal snow cover. In the example the anticrack model predicts a critical crack length of 0.25 m in the horizontal, 0.31 m in a slope of 30° and 0.37 m in a slope of 40° . These lengths are much shorter than the above critical lengths for simple shear cracks in the same slope. This is a very satisfying result from a practical point of view, as it is difficult to conceive how a skier could create a shear crack of several metres in diameter (as the shear model would require) if his zone of influence, determined experimentally, is a meter at most [66].

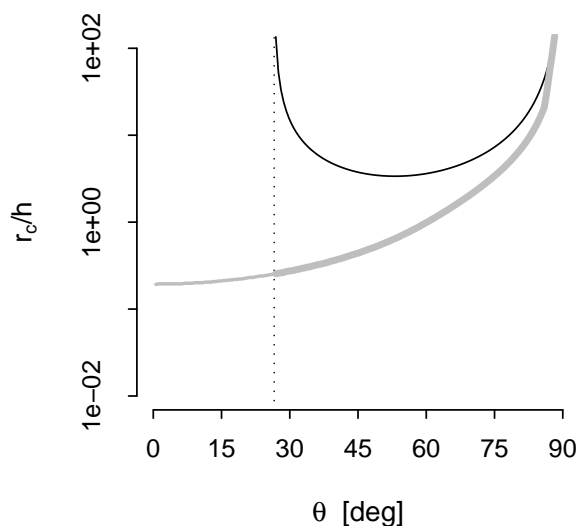


Figure 6.5: Critical crack length $r_c(\theta)$, as calculated with the simple shear model (black curve) and the anticrack model (grey curve; thin: fracture propagation results in a whumpf; thick: fracture propagation results in a slab avalanche). Increasing μ shifts the asymptote to the right, decreasing μ to the left. Here $\mu = 0.5$. Data according to Table 6.2.

A similar analysis applies to the condition for skier instability Eq. 4.20 (Fig. 6.6). This condition gives the minimal line load p , assumed here to act vertically, for which the energy barrier disappears, resulting in spontaneous crack nucleation. As previously, the simple shear model (black curve in Fig. 6.6) divides the terrain into slopes in which fracture cannot be triggered ($\theta \leq \theta_\mu$), where p is out of bounds and into slopes in which fracture can be triggered ($\theta > \theta_\mu$), where p is finite. With increasing slope angle the critical line load p rapidly and monotonically decreases. For a crack-face friction coefficient $\mu = 0.5$ (as used in Fig. 6.6), the calculated critical line loads for a simple shear crack are 4.5 kN/m in a slope of 40° and 19 kN/m in a slope of 30° . This represents 10 to 50 times the load of a skier of 70 kg on 1.70 m skies (which amounts to $p = 0.4$ kN/m).

As previously the anticrack model (grey curve in Fig. 6.6) does not divide the terrain into slopes in which fracture can or cannot be triggered. The critical line load to eliminate the energy barrier is nearly constant up to very steep slopes and amounts to about 0.8 kN/m in the example, which represents twice the load of the same skier as above. According to the model, skiing swiftly could thus cause fracture nucleation in the example snow cover. The wide plateau in Fig. 6.6 indicates that triggering an anticrack causing a whumpf or slab avalanche is equally difficult (or equally easy) on all skiable slopes, regardless of slope angle. However, triggering is often believed to be easier in steep slopes, as the simple shear model suggests. In fact a rigorous

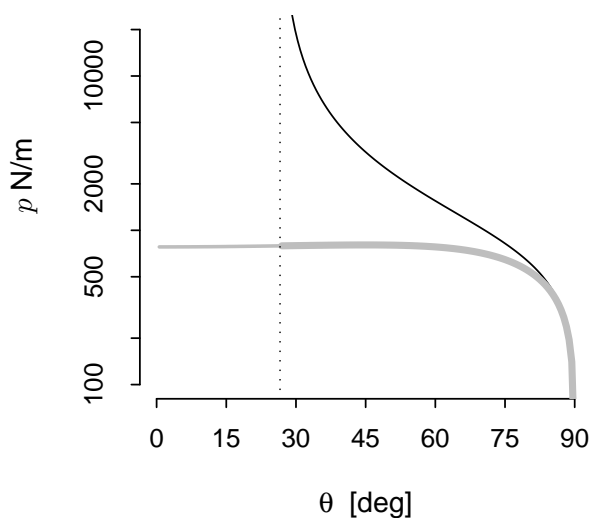


Figure 6.6: Critical line charge $p(\theta)$, as calculated with the simple shear model (black curve) and with the anticrack model (grey curve; thin: fracture propagation results in a whumpf; thick: fracture propagation results in a slab avalanche). Increasing μ shifts the asymptote to the right, decreasing μ shifts the asymptote to the left. Here $\mu = 0.5$. Data according to Table 6.2.

risk analysis related to slope angle has never been done and the relation between slope angle and probability of triggering has never been established [65]. The idea that triggering fracture is easier in steep slopes is therefore not substantiated. If incorrect, it may originate in biased perception: while triggering a whumpf is likely to pass unnoticed, triggering a slab avalanche is obviously not. Whatever the true relation is, is not known at present, but for the time being, one can conclude that the anticrack model implies that weak, collapsible layers in stratified snow fail about as easily on flat ground as in steep slopes, regardless of failure being spontaneous, artificial or triggered by a skier. In one case this proposition has already been anticipated and proven: Gauthier and Jamieson's PST experiments demonstrated very weak slope dependence for the onset of fracture propagation [25].

The analysis shows that it is difficult for a skier to trigger a supercritical shear crack. In the example, line forces up to 20 kN/m are required. It is considerably easier to trigger a supercritical anticrack, in which case loads around 1 kN/m are required. Quantitatively, neither the calculated critical load for a shear crack nor the calculated critical load for an anticrack appear entirely satisfying: The critical load calculated with the simple shear model seems too high, while that calculated with Eq. 4.20 seems too low. On the one side, disorder may knock down the energy barrier. On the other side, model assumptions may result in underestimating the critical loads. Dissipation results in less work done by the applied load p being available for fracture nucleation. Moreover, the Dirac-type load $p \propto \delta(x)$ and the Timoshenko beam approximation result in a very concentrated and therefore efficient, perhaps too efficient load model of the weak layer. A more detailed model should spread the load on the weak layer over a wider area. With more knowledge on the effective load distribution at hand, the skier situation could be modelled by superposition of the present solution using a Green's function approach.

Avalanche records show that the release of slab avalanches on slopes tilted by less than 26° is very exceptional and even a release for angles between 26° and 30° is rare [20, 65]. These angles usually relate to the steepest parts of the starting zone on a scale of $20 \text{ m} \times 20 \text{ m}$. Average angles of the entire starting zone are therefore expected to be somewhat lower.

Apparently, simple shear models explain this naturally: as slope angle decreases, both r_c and p become prohibitively high (as Figs. 6.5 and 6.6 show) and therefore triggering becomes increasingly unlikely the lower the slope angle, and impossible below the friction angle. In fact, the shear model implies that the minimum angle for triggering an avalanche should depend both on the amount of loading and on the friction coefficient of the fracture debris (or equivalently its friction angle).

The anticrack model also indicates that slab avalanches release on slopes steeper than the friction angle, but the threshold is sharp: Immediately below the friction angle, initiating sustained fracture results in a whumpf, while immediately above the friction angle, initiating sustained fracture results in an avalanche. There is no gradual increase of hazard with slope angle as in the shear model, but an immediate transition from whumpfing to avalanching. Moreover, the calculation shows that if the load is sufficient to trigger a whumpf in flat ground, the same load is also

sufficient to trigger an avalanche in steeper terrain (Fig. 6.6). A question remains. If crack-face friction coefficients in the debris can possibly be as low as 0.4 (section 2.5), corresponding to a friction angle of 22° , should avalanches not be expected down to slope angles of 22° ? In fact crack-face friction at the very start of slab motion has yet to be measured. The measurements of Casassa [11] are merely proxies and only yield indicative values. Still it may be asked whether such low release angles are theoretically possible or not. The total resistance to slab motion cannot entirely be reduced to crack-face friction. The snow in place around the delaminated slab, the *stauchwall*¹ in particular, stabilises the slab against downslope motion. Thus the net pull on the slab must not only overcome crack-face friction but also some additional resistance. But this argument does not apply when very large slabs are released, as the relative importance of the peripheral forces decreases with size. It should then be invoked that planar fracture interfaces (as assumed in the model) do not actually exist in nature. Real weak layers and interfaces are curved and rough at various scales: at the centimetre-scale as shown by Löwe, Egli and Bartlett. [49], at the metre-scale ("bumps") and at the slope scale (convexity-concavity). It can be expected that roughness stabilises the slab against slip, resulting in additional resistance to be overcome, and hence higher critical slope angles.

The problem of the slab sliding as a whole or staying in place as a whole just after it was undercut by an anticrack could be in fact even more complex. In a random material like snow, the crack-face friction coefficient μ can be considered a stochastic function of x and, in a real slope, the slope angle θ can be considered another stochastic function of x . The correlation lengths of these processes may differ by orders of magnitude, depending on terrain. Moreover, static friction applies to crack face friction, which in snow can be quite unpredictable due to the rapid sintering of snow on the scale of seconds, depending on factors such as grain structure and grain temperature [6]. In the general case the threshold slope angle for the whumpf-avalanche transition is thus expected to depend on these stochastic functions, on grain structure and grain temperature. Measuring and forecasting the whumpf-avalanche threshold angle and relating it to weak layer state would be of great practical value.

Avalanche warning services recommend not to ski steep slopes during periods of increased hazard. This recommendation appears in a very different light when the explanation is sought with the shear model or with the anticrack model. Suppose that, as is often the case, one has limited prior knowledge of the existence of weak layers and no prior knowledge of the spatial extension of the weak layers in the hill slopes. In the understanding of the shear model, one would expect that increasing slope angle increases the odds of triggering fracture in a weak layer (Fig 6.6, black curve). As this not the case in the anticrack model, the reason for avoiding steep terrain appears to reside in the availability of weak layers with crack-face friction larger than the local slope angle (or potentially so, because crack-face friction only comes into existence if failure is actually triggered). But even avoiding these "hot slopes" will not make the journey entirely safe, due to the possibility of remote triggering.

¹Stauchwall: downslope wall of the perimeter of the release area.

Avalanche warning services recommend that skiers should observe a minimum clearing distance between individuals during periods of increased hazard. In the understanding of the shear model, this recommendation makes sense only in slopes steeper than the friction angle. In gentler slopes there are no net shear forces to add when a crack forms in the weak layer. In the light of the anticrack model, this recommendation must on the contrary hold for any slope angle, including the horizontal. Indeed, the compressive components never vanish and, if two skiers are closeby, the condition for skier instability is easier to fulfill.

Another conclusion that can be drawn here is that valid signals for the instability of a weak layer can be found on gentle slopes and even on horizontal terrain as long as fracture nucleation is concerned (without regard of the subsequent friction problem). Practitioners have known and applied this idea for a long time, although seemingly without realising how conflicting it is with the simple shear model of slab avalanche formation, which implies that fracture nucleation and propagation can only be studied in steep slopes.

6.5 Triggering mechanisms

In chapter 4, a snowpack containing an unflawed weak layer was shown to be fundamentally metastable, i.e. stable if undisturbed. Instability can only be obtained in this case by a perturbation or by deterioration of the energy barrier. Three mechanisms for fracture nucleation were proposed, which achieve either the first or the second: nucleus instability, skier instability and gap instability.

Nucleus instability implies the existence of a pre-cracked area or flaw and therefore is not properly a nucleation criterion from nil, but a condition for a stable flaw to turn into a propagating fracture. This condition, given by Eq. 4.17, can only be fulfilled during snowfall as the load on the weak layer increases or, after snowfall, by deterioration of w_f or formation of depth hoar.

Skier instability and gap instability are proper nucleation mechanisms, as they eliminate the energy barrier for continuum cracks of size zero. The skier instability is dominated by the compression, not the shear, exerted on the weak layer. Indeed, assuming that the line load p acts vertically, Eq. 4.20 indicates that in slopes inclined less than 45° , over 75 % of the energy contribution of the skier to the reduction of the energy barrier comes from the slope-perpendicular component p_y . This is because $p_y \geq p_x$ for $\theta \leq 45^\circ$ and because of the prefactor $3\eta^2 \approx 3$ of p_y . In a slope of 30° the proportion increases to 90 %.

By contrast, the gap instability is purely a shear instability, as only τ but not σ appears in Eq. 4.22. Gaps reaching deep into the snowpack are rarely observed in snow and probably cannot explain many avalanches. The possibility however, cannot be excluded and occasionally they may be the cause for slab release. The dangerous gap reaches as deep or deeper than the weak layer (as shown in Fig. 4.9) and its faces must not touch. If there is contact between the opposing faces, the work of the contact forces increases the energy barrier and decreases

the chances of spontaneous triggering. Gaps may sometimes be formed by uneven creep of the snow cover, although this will quite often destroy the weak layer (A. Duclos, personal communication). Gaps may also be created by a skier leaving a deep track in the snowpack. This of course is not the usual trigger action due to compression of the weak layer described by Eq. 4.20 and should probably be considered an exception in practice. It indicates however, that even if the skies sink below the level of the weak layer, the triggering of fracture is still possible. Gap instability may give back some credit to an old argument by Perla and LaChapelle [61]: that a transverse fracture surface perpendicular to the slope may in some circumstances be the primary cause of slab avalanches. The difference with the original idea is that the gap is not identified with the crown wall, but with the originating point of the basal failure of the weak layer, from which the fracture may propagate upslope, downslope or in both directions.

The three triggering mechanisms discussed above are propositions that are deduced mathematically from the anticrack model in its present form. They are plausible and theoretically founded but remain conjectures and have to be validated by field experiments. The primary focus should be whether these mechanisms do or do not exhibit the correct trends, for example with slope angle θ (as in Figs. 6.5 and 6.6), with slab thickness h and with loading (e.g. by adding or removing snow on the surface and repeating the experiment under similar conditions). Such experiments may indicate in which direction the model has to be developed in the future.

6.6 Further research

Based on the anticrack model, many bifurcations for further research are possible. They can be grouped into the following topics: crack-face friction, dissipation, disorder and solutions for fast collapse waves, as briefly discussed below.

1. Crack-face friction poses many questions. Coulomb friction may not be sufficient to describe crack-face contacts, and adhesion, Newtonian friction, velocity dependence and sintering time scales may have to be taken into account. Interesting perspectives reside in the measurement of crack-face friction in PST-type or ECT-type experiments in steep slopes, e.g. by measuring the acceleration of the slab immediately after complete debonding.
2. Dissipation: Besides irreversible fracture, an important dissipative process for collapse waves seems to be the formation of transverse cracks across the slab. Fracture arrest appears to be an important factor for avalanche hazard. Experimental research related to this aspect of collapse waves has recently been undertaken by Gauthier and Jamieson [25, 26]. Some slabs seem very effective in transmitting collapse waves, while other slabs seem very effective in stopping collapse waves. It is not presently known why. A possible reason of arrest is the collapse wave hitting flaws in the slab, resulting in transverse fracture as shown in Fig. 1.2.
3. Disorder: Microstructural randomness at grain-scale, wind-deposited snow in turbulent air and countless other factors make snow a very heterogeneous material. As a consequence

material properties vary randomly in space and the energy barrier becomes a random variable. The objective is then to obtain a probabilistic expression for the Griffith-Irwin criterion. Yet another extension is possible. In the present work fracture nucleation was studied on a simple topology with a single crack. Anticrack physics can be revisited by extending the topology to a population of interacting flaws within the same weak layer or within different layers. Using extremal statistics the goal is then to find the probability of global failure of a specimen of given size under defined loading.

4. Collapse waves: In the development of the collapse wave model presented in chapter 5, only solutions for slow collapse waves with distinctly sub-shear velocity were obtained. The calculation also suggests the existence of faster collapse waves, notably super-shear and possibly even supersonic waves. These possibilities raise interesting theoretical and experimental questions.

Chapter 7

Conclusion

Like Steven Weinberg's chronology of the Big Bang's first three minutes [84], the present work may be concluded by giving a short account of the first three metres of the little bang that occurs when a slab avalanche is triggered on a slope. The events are related in terms of the size r of the expanding failure zone.

The nucleation of an avalanche begins, like the Big Bang, in a blur. The anticrack model tunes in at a scale of a few centimetres, at which the granular structure no longer impedes a continuum description of stress and strain fields in the slab. Initially, the slab is not supported homogeneously, but at random points by small crystalline grains of ice, the collectivity of which forms a network called a weak layer. The grains in this network are not equally strong nor equally spaced. When a small portion of this network fails, it is broken into debris which can pack tighter than the initial structure. This results in an interruption of the stress field. Both the compressive and the shear components vanish in the small area where the weak layer crumbles. This 'hole' in the stress field can be described as a mixed-mode anticrack exposed to the action of far-field compressive stress and shear stress. The mixed-mode anticrack may nucleate in a small zone where the grains are mostly frail and sparsely populated (e.g. Figs. 1.2a and 4.1a). It may also nucleate in stronger and more populated zones through the action of an external triggering agent, e.g. a skier. A necessary condition for the nucleus to expand is a monotonic decrease in crack energy. This occurs when the crack length exceeds the critical size determined by the energy barrier. For heavily loaded slopes this can be a length of a few centimetres, in lesser loaded slopes a few decimetres, in absence of volumetric collapse it can be a few metres. Beyond the critical length, crack growth releases more energy than it consumes. Only dissipative processes such as transverse fracture across the slab can now stop the propagation of the crack. If crack propagation carries on, at some stage the debris will attain maximum compaction in the middle of the crack (Fig. 4.1c). From that moment on, subsidence stops and a kink-shaped collapse wave gradually develops, heading out in all directions. This wave is the carrier for the progressive delamination of the weak layer. A typical wavelength is

of the order of a metre or a couple of metres, a typical propagation velocity around 20 m/s or 30 m/s. If crack-face friction in the delaminated section is large or the slope angle small, the slab subsides, resulting in a whumpf. If crack-face friction is small or the slope angle large, the slab slides, resulting in a slab avalanche. Other scenarios than this one are possible. For example, a skier may nucleate an unstable crack from nil.

In the following, conclusions which can be drawn from the mathematical model are listed. Regarding fracture nucleation, the following conclusions are made:

1. The anticrack model unifies the physics of whumpf and slab avalanche formation, which were originally thought to be independent. Nucleation and propagation of these instabilities can be described by the same energy function.
2. Under assumptions listed in section 6.3, the energy of formation $V(r)$ of a crack of size r in a weak subsurface layer of the snowpack has been determined (Eq. 4.10). The maximum of $V(r)$, if it exists, determines the energy barrier for crack propagation.
3. Within the assumptions of the present model, unflawed and undisturbed slopes are fundamentally stable as the energy barrier is always strictly positive in these cases.
4. The energy barrier can disappear altogether by action of a skier (Eq. 4.20) or by formation of a gap in a steep portion of snowpack (Eq. 4.22), resulting in fracture nucleation even in absence of a pre-cracked area or shear-deficit zone.
5. Simple shear cracks can neither nucleate nor propagate when crack-face friction surpasses the shear load on the weak layer. This limitation does not exist for anticracks.
6. A long anticrack with contacting crack faces cannot be approximated as a simple shear crack: The anticrack mechanism contributes by decreasing the effective fracture energy (Eq. 4.9).
7. According to the anticrack model, the release of a slab avalanche is the result of a two-stage scenario, in which two conditions have to be met separately. Firstly, fracture must be triggered and propagate in order to destroy cohesion across the weak layer. Secondly, the shear load on the weak layer must exceed the residual crack-face friction. If the second condition is not fulfilled, the slab will subside but not slide and the outcome is a whumpf.

Regarding fracture propagation, the following conclusions are made:

1. Collapse waves are driven by both slope-normal and slope-parallel components of gravity, which never simultaneously vanish for any slope angle. The collapse wave can therefore climb or descend a slope from adjacent flat ground or propagate across a slope inclined less than the friction angle. This explains the remote triggering of slab avalanches from adjacent flat ground and from within the slope.

2. The collapse wave is dispersive. A combination of material properties and stratification geometry determines its wavelength and propagation velocity. The velocities are distinctly smaller than those of elastic shear waves in the slab.
3. The collapse wave is an energetically self-sustained perturbation and therefore its propagation is not limited by the energy initially available during trigger action. The collapse wave gets its energy on the spot from the subsiding slab. This bridges the gap between the small amounts of energy needed to trigger fracture and the comparatively large amounts of energy needed to release a slab avalanche .
4. One reason for fracture arrest is the interruption of the strain field by the formation of transverse cracks, effectively blocking the flow of elastic strain energy across the slab. Based on field observations, the formation of transverse cracks not always results in fracture arrest. Transverse cracks may originate from the collapse wave hitting a flaw.

Regarding model validation, the following conclusions are made:

1. The superposition of successive video frames from the Davos-Stilli experiment (Fig. 6.2) shows an instance in which the fracture process develops as expected by the anticrack model.
2. The present theory is confirmed by recent field experiments which have shown that the critical length of artificial cracks is weakly affected by slope angle, for angles between 0° and 40° . In simple shear models, by comparison, the critical crack length for propagation of shear cracks along weak layers would increase without bound as the slope angle decreases towards the friction angle of crack faces.
3. According to first field measurements at Davos-Wannengrat, the model presented in chapter 5 predicts the velocity and wavelength of collapse waves with good precision.
4. The anticrack model is in line with field experience and explains remote triggering of slab avalanches, the linkage between whumpfs and avalanche hazard and the so far unexplained whumpf phenomenon itself.

Regarding model formulation, the following conclusions are made:

1. The mixed-mode anticrack model contains previous shear models [50, 53] as limiting cases. These cases are obtained by assuming zero volume reduction during failure ($h_f = 0$). The anticrack model also contains previous collapse models [32, 33].
2. The mathematical description of the anticrack is not particular to any specific microstructural model. The key elements - volumetric collapse of fracture debris and residual friction - apply to any weak layer composed of grains that can rearrange in a more tightly packed

order. In snow, this includes layers composed of faceted crystals or depth hoar. Indeed the present model produces accurate results for field experiments on weak layers of these types as done by Sigrist [69].

3. The vanishing compressive stress in the cracked weak layer (which is due to volumetric reduction) gives a natural explanation for zero residual Coulomb friction between crack faces. This favours the expansion of the crack until contact between slab and substrate is established.
4. For numerical applications, the anticrack model requires to compute the crack energy function $V(r)$ as a function of crack or notch size r (Eqs. 4.10, 4.13) and determine for which r the function attains its maximum.

Regarding the interpretation of the model for avalanche hazard, the following conclusions are made:

1. In simple shear models the slope angle is a dominant factor for fracture nucleation: Critical crack lengths strongly depend on slope angle. In the anticrack model, this is not the case: Critical crack lengths, if at all, depend weakly on slope angle. Moreover, if a load is sufficient to trigger a whumpf on flat terrain, the same load is also sufficient to trigger an avalanche in steeper terrain under similar conditions.
2. In simple shear models an increase (decrease) of avalanche hazard is attributed to a decrease (increase) in length of the critical shear crack: The dependence of avalanche hazard on slope angle is gradual. In the anticrack model, this view is replaced by a two-stage scenario: In the first stage, nucleation and propagation of a mixed-mode anticrack delaminates the slab from the snow below. This process can occur with or without shear loading and for arbitrary amounts of crack-face friction. In the second stage frictional forces between the crack faces decide whether the slab will slide, causing an avalanche, or subside, causing a whumpf.
3. The anticrack model indicates an immediate transition from whumpfing to avalanching as slope angle increases above friction angle.
4. In presence of flaws on the centimetre scale, stratified snow can collapse under its own weight, as shown by Eq. 4.14.
5. In skiable slopes, the critical size and critical line load for the onset of crack propagation are substantially lower for mixed-mode anticracks than for simple shear cracks. This is due to gravitational potential energy freed by bending of the unsupported slab, a contribution that is not taken into account by simple shear theories. A second reason is the absence of Coulomb friction for small anticracks.

6. The previously unexplained correlation between occurrence of whumpfs and occurrence of slab avalanches receives a natural explanation, as the underlying physics have been shown to be identical.
7. As opposed to a shear crack nucleus, an anticrack nucleus is an entity that may not readily disappear by sintering. The void between the faces -if it exists as such- must first be bridged by vapor transport, before additional transport mechanisms such as surface diffusion can set in. This may give some credit to the existence and persistence of so-called super-weak spots [64].
8. One can speculate that a contributing factor to slab avalanche hazard is the amount of crack-face friction appearing in the fractured weak layers: The lower the crack-face friction, the more total hillside surface is potentially available for avalanching.

Direct applications of the model are:

1. The anticrack model, Eq. 4.13, can be used to analyse notch experiments of the type proposed by Gauthier and Jamieson [25] and Sigrist and Schweizer [69]. The fracture energy of the weak layer w_f can be deduced analytically with the anticrack model: By substitution of $r = r_c$, where r_c is the measured critical length, into $\partial_r V(r, w_f) = 0$, where V is given by Eq. 4.13, an equation for w_f is obtained. The resulting value for w_f can be substituted into Eq. 4.10 to calculate the critical length of a crack.
2. Snow slope stability can be studied on data from field measurements or on snowpack model data [9, 48] by substitution of material properties and stratification geometry into the expressions for nucleus instability (Eq. 4.17), skier instability (Eq. 4.20) and gap instability (Eq. 4.22).
3. The notch experiments proposed by Gauthier and Jamieson [25] and by Sigrist and Schweizer [69] can be used for the purpose of determining the critical length for self-sustained fracture propagation. It is recommended that the length of the specimen should exceed a few times the critical length r_c or a few times the slab thickness h , whichever is larger. If the sample is shorter, a size effect due to the free boundary at the opposing end of the notch appears. If the notch experiment is used to create and examine properties of collapse waves, its length should exceed several times the wavelength.

Many questions have not been addressed by the present model:

1. Disorder was not taken into account in the present continuum crack formulation. An effect of disorder is the fluctuation in space of the crack energy. The energy barrier for crack propagation must then be considered a random variable.

2. The anticrack has been modelled in a 3-layer continuum extending in one dimension for reason of analytical simplicity. As a real snowpack extends in two dimensions and embodies multiple layers, the analytical expression for the crack energy is affected.
3. While the sustainability of the collapse wave has been addressed in terms of available energy, it has not been done so in terms of dissipative processes in the slab, e.g. in the formation of transverse cracks. Evidence for transverse crack opening has been observed in field experiments carried out with A. van Herwijnen. The amount of such damage may play an important role in fracture arrest, which seems crucial for the evaluation of avalanche hazard.
4. In the present model the weak layer is assumed to collapse instantaneously (once the required fracture energy is provided) and Coulomb friction is assumed to appear only once the faces of the anticrack make contact. Although to some extent justified, this is an idealisation.
5. The question of how volume reduction during failure is related to the initial structure of the material has been left aside.

The present model is in many respects an elementary formulation of mixed-mode anticracks in weak subsurface layers. The price for simplicity is, perhaps, limited accuracy. Although comparison with experiments indicates that the accuracy of the model predictions is by all means usable. The benefit of simplicity is the small number of parameters needed to apply the model. The traditional simple shear model requires a set of six descriptive parameters: the fracture energy w_f and the crack-face friction μ of the weak layer, the Young's modulus E , the density ρ and the thickness h of the slab, and the slope angle θ . In addition to those, the anticrack model requires only one more parameter: the collapse amplitude h_f .

The *raison d'être* of the present contribution is to account for volume loss in the fracture area and to understand the anticrack mechanism which is associated. The results explain why compressive forces are effective in nucleating and propagating failure in a weak layer of snow. The present theory is still very young. Some of the results are perhaps transitory, but it may already be said that anticrack physics is now well under way in snow science.

Appendix A

Material properties of snow and ice

Table A.1: Physical properties of dry seasonal snow (slab material and weak layer material).

Notation	Description	Range	Units
Slab material:			
ρ	Average density [64]	100 – 300	kg/m ³
E	Elastic modulus [57, 63, 67]	1 – 10 ²	MPa
ν	Poisson's ratio [67]	0.2 – 0.35	
Weak layer:			
w_f	Fracture energy [69, 71].	10 ⁻² – 10 ⁻¹	J/m ²
μ	Friction coefficient for snow contacts [11]	> 0.4	

Table A.2: Physical properties of ice (multicrystalline). Data compiled from [6, 34, 44]

Notation	Description	Value	Units
ρ_0	Density (273 K, 10 ⁵ Pa)	917(1)	kg/m ³
E	Elastic modulus	8.7 – 9.9	GPa
μ	Shear modulus	3.4 – 3.8	GPa
η	Poisson's ratio	0.31 – 0.37	-
Fracture:			
$K_{I,c}$	Toughness mode I	0.18(7)	MPa√m
Surface energy:			
γ_{sv}	Solid-vapor	0.109	J/m ²
γ_{sl}	Solid-liquid	0.033	J/m ²
γ_{ss}	Solid-grain boundary-solid	0.065	J/m ²

Appendix B

FEM results for crack energies

Tables B.1 and B.2 below list results from finite element modelling of cracks for configurations as listed in table 4.2. For discussion see section 4.8.

Table B.1: FEM results (Ansys 9.0) for crack energies per unit width for various slope angles θ .

Table 4.2a		Table 4.2b		Table 4.2b	
$\theta = 0^\circ$		$\theta = 30^\circ$		$\theta = 90^\circ$	
r [m]	$V_m(r)$ [J/m]	r [m]	$V_m(r)$ [J/m]	r [m]	$V_m(r)$ [J/m]
0.01	9.90×10^{-6}	0.01	2.42×10^{-5}	0.05	6.61×10^{-4}
0.05	2.89×10^{-4}	0.05	7.07×10^{-4}	0.15	7.23×10^{-3}
0.15	3.21×10^{-3}	0.15	7.83×10^{-3}	0.30	3.18×10^{-2}
0.30	1.89×10^{-2}	0.30	4.34×10^{-2}	0.50	9.72×10^{-2}
0.50	9.29×10^{-2}	0.50	1.99×10^{-1}	0.70	2.08×10^{-1}
0.70	3.12×10^{-1}	0.70	6.36×10^{-1}	0.90	3.74×10^{-1}
0.90	8.33×10^{-1}	0.90	1.66×10^0	2.00	2.74×10^0
1.42	5.77×10^0	1.14	4.28×10^0	3.00	8.14×10^0

Table B.2: FEM results (Ansys 9.0) for notch energies per unit width for various slope angles θ .

Table 4.2a		Table 4.2b		Table 4.2b		Table 4.2b	
-		case Fig. 4.5b		case Fig. 4.5c		-	
$\theta = 0^\circ$		$\theta = 30^\circ$		$\theta = 30^\circ$		$\theta = 90^\circ$	
r [m]	$V_m(r)$ [J/m]	r [m]	$V_m(r)$ [J/m]	r [m]	$V_m(r)$ [J/m]	r [m]	$V_m(r)$ [J/m]
0.01	1.26×10^{-5}	0.01	1.61×10^{-4}	0.01	6.40×10^{-6}	0.01	2.34×10^{-4}
0.05	2.15×10^{-4}	0.05	2.01×10^{-3}	0.02	1.35×10^{-5}	0.02	6.66×10^{-4}
0.15	2.22×10^{-3}	0.15	1.28×10^{-2}	0.05	2.38×10^{-5}	0.05	2.37×10^{-3}
0.30	1.49×10^{-2}	0.30	5.73×10^{-2}	0.10	1.56×10^{-4}	0.10	5.88×10^{-3}
0.50	8.36×10^{-2}	0.50	2.40×10^{-1}	0.15	8.26×10^{-4}	0.15	1.01×10^{-2}
0.70	3.02×10^{-1}	0.70	7.45×10^{-1}	0.30	1.35×10^{-2}	0.30	2.82×10^{-2}
0.90	8.43×10^{-1}	0.81	1.27×10^0	0.50	1.10×10^{-1}	0.50	6.81×10^{-2}
1.05	1.63×10^0			0.70	4.60×10^{-1}	0.70	1.31×10^{-1}

Bibliography

- [1] M. J. Alava, P. K. V. V. Nukala, and S. Zapperi. Statistical models of fracture. *Adv. Phys.*, 55(3-4):349–476, 2006.
- [2] P. F. Arndt and T. Nattermann. Criterion for crack formation in disordered materials. *Phys. Rev. B*, 63(13):134204, Apr. 2001.
- [3] E. M. Arons and S. C. Colbeck. Geometry of heat and mass-transfer in dry snow - a review of theory and experiment. *Review of Geophysics*, 33(4):463–493, 1995.
- [4] H. P. Bader and B. Salm. On the mechanics of snow slab release. *Cold Reg. Sci. Technol.*, 17:288–300, 1990.
- [5] Z. P. Bažant, G. Zi, and D. McClung. Size effect law and fracture mechanics of the triggering of dry snow slab avalanches. *Journal of Geophysical Research (Solid Earth)*, 108:2119, Feb. 2003.
- [6] J. R. Blackford. Sintering and microstructure of ice: a review. *J. Phys. D*, 40:R355–R385, 2007.
- [7] C. F. Bohren and R. L. Beschta. Comment on wave propagation in snow. *Am. J. Phys.*, 42:69–70, 1974.
- [8] C. C. Bradley. Collapsing snow. In *Proc. of the western snow conference, Fort Collins, USA*, pages 63–68, 1969.
- [9] E. Brun, P. David, and M. Sudul. A numerical-model to simulate snow-cover stratigraphy for operational avalanche forecasting. *J. Glaciol.*, 38(128):13–22, 1992.
- [10] G. Casassa, H. Narita, and N. Maeno. Measurement of friction coefficients of snow blocks. *Ann. Glaciol.*, 13:40–44, 1989.
- [11] G. Casassa, H. Narita, and N. Maeno. Shear cell experiments of snow and ice friction. *J. Appl. Phys.*, 69(6):3745–3753, 1991.
- [12] B. M. Chiaia, P. Cornetti, and B. Frigo. Triggering of dry snow slab avalanches: stress versus fracture mechanical approach. *Cold Reg. Sci. Technol.*, 53(2):170–178, 2008.

- [13] H. Conway and J. Abrahamson. Snow stability index. *J. Glaciol.*, 30:321–327, 1984.
- [14] S. L. den Hartog. Firn quake (a rare and poorly explained phenomenon). *Cold Reg. Sci. Technol.*, 6:173–174, 1982.
- [15] J. Dundurs. Edge-bonded dissimilar orthogonal elastic wedges. *J. Appl. Mech.*, 32:400–402, 1969.
- [16] Editorial Committee. *Report on Hanshin-Awaji Earthquake Disaster: Building Series Volume 1*. Architectural Institute of Japan, Tokyo, 1997.
- [17] J. Faillettaz. *Le déclenchement des avalanches de plaque de neige: De l'approche mécanique à l'approche statistique*. PhD thesis, Université Josef Fourier (Grenoble I), 2003.
- [18] R. C. Fletcher and D. D. Pollard. Anticrack model for pressure solution surfaces. *Geology*, 9:419–424, 1981.
- [19] A. D. Frolov and I. V. Fedyukin. Elastic properties of snow-ice formations in their whole density range. *Ann. Glaciol.*, 26:55–58, 1998.
- [20] B. Fyffe. *Mechanisms of snow slab avalanche release*. PhD thesis, University of Edinburgh, 2006.
- [21] B. Fyffe, J. Schwerdtfeger, J. R. Blackford, M. Zaiser, A. Konstantinidis, and E. C. Aifantis. Fracture toughness of snow: the influence of layered microstructure. *J. of the Mechanical Behaviour of Materials*, 18(3):195–214, 2007.
- [22] B. Fyffe and M. Zaiser. The effects of snow variability on slab avalanche release. *Cold Reg. Sci. Technol.*, 40(3):229–242, 2004.
- [23] D. Gauthier. *A practical field test for fracture propagation and arrest in weak snowpack layers*. PhD thesis, University of Calgary, 2007.
- [24] D. Gauthier and B. Jamieson. Evaluating a prototype field test for weak layer fracture and failure propagation. In *Proceedings of the 2006 International Snow Science Workshop, Telluride, Colorado*, 2006.
- [25] D. Gauthier and B. Jamieson. Evaluation of a prototype field test for fracture and failure propagation propensity in weak snowpack layers. *Cold Reg. Sci. Technol.*, 51(2-3):87–97, 2008.
- [26] D. Gauthier and B. Jamieson. Fracture propagation propensity in relation to snow slab avalanche release: Validating the propagation saw test. *Geophys. Res. Lett.*, 35:L13501, 2008.

- [27] A. A. Griffith. The phenomena of rupture and flow in solids. *Phil. Trans. Roy. Soc. Lond.*, A(221):163, 1920.
- [28] P. Gumbsch and R. M. Cannon. Atomistic aspects of brittle fracture. *MRS Bulletin*, 25(5), 2000.
- [29] S. Harvey and et al. *Caution Avalanches! Fifth edition*. Institute for Snow and Avalanche Research SLF, Davos; Federal Office of Sports Magglingen (BASPO); Swiss Alpine Club SAC; Swiss Army; Swiss Ski, SLF Davos, Switzerland, 2005.
- [30] J. Heierli. Solitary fracture waves in metastable snow stratifications. *Journal of Geophysical Research (Earth Surface)*, 110(F9):F02008, May 2005.
- [31] J. Heierli, P. Gumbsch, and M. Zaiser. Anticrack nucleation as triggering mechanism for slab avalanches. *Science*, 321(5886):240–243, 2008.
- [32] J. Heierli and M. Zaiser. An analytical model for fracture nucleation in collapsible stratifications. *Geophys. Res. Lett.*, 33:L06501, Mar. 2006.
- [33] J. Heierli and M. Zaiser. Failure initiation in snow stratifications containing weak layers: Nucleation of whumpfs and slab avalanches. *Cold Reg. Sci. Technol.*, 52(3):385–400, Feb. 2008.
- [34] P. V. Hobbs. *Ice physics*. Clarendon Press, Oxford, 1974.
- [35] J. W. Hutchinson and Z. Suo. Mixed-mode cracking in layered materials. *Adv. Appl. Mech.*, 29:63–191, 1992.
- [36] C. E. Inglis. Stresses in a plate due to the presence of cracks and sharp corners. *Trans. Inst. Naval Archit.*, 55:219, 1913.
- [37] J. B. Jamieson and J. Schweizer. Texture and strength changes of buried surface-hoar layers with implications for dry snow-slab avalanche release. *J. Glaciol.*, 46:151–160, 2000.
- [38] B. Johnson and B. Jamieson. Field data and theory for human-triggered "whumpfs" and remote avalanches. In *Proceedings of the 2000 International Snow Science Workshop, Big Sky, Montana*, 2001.
- [39] B. C. Johnson. *Remotely triggered slab avalanches*. PhD thesis, University of Calgary, 2001.
- [40] B. C. Johnson, J. B. Jamieson, and R. R. Stewart. Seismic measurements of fracture speed in a weak snowpack layer. *Cold Reg. Sci. Technol.*, 40:41–45, 2004.
- [41] I. Keplerus. *De niue sexangula*. Godefridum Tampach Verlag, Francofvrti ad Moenvm, (2nd ed. 2005, Hellerau-Verlag. Dresden), 1611.

- [42] H. O. Kirchner, G. Michot, and J. Schweizer. Fracture toughness of snow in shear under friction. *Phys. Rev. E*, 66(2):027103, 2002.
- [43] H. O. Kirchner, G. Michot, and T. Suzuki. Fracture toughness of snow in tension. *Philos. Mag. A*, 80(5):1265–1272, 2000.
- [44] H. O. Kirchner, H. Peterlik, and G. Michot. Size independence of the strength of snow. *Phys. Rev. E*, 69(1):011306, Jan. 2004.
- [45] C. A. Knight and N. C. Knight. Superheated ice: true compression fractures and fast internal melting. *Science*, 178(4061):613–614, 1972.
- [46] B. Lackinger. Supporting forces and stability of snow-slab avalanches: a parameter study. *Ann. Glaciol.*, 13:140–145, 1984.
- [47] B. Lawn. *Fracture of brittle solids - second edition*. Cambridge University Press, Cambridge, New York, Melbourne, 1993.
- [48] M. Lehning, P. Bartelt, B. Brown, and et. al. SNOWPACK model calculations for avalanche warning based upon a new network of weather and snow stations. *Cold Reg. Sci. Technol.*, 30(1-3):145–157, 1999.
- [49] H. Löwe, L. Egli, S. Bartlett, M. Guala, and C. Manes. On the evolution of the snow surface during snowfall. *Geophys. Res. Lett.*, 34:L21507, 2007.
- [50] F. Louchet, J. Faillietaz, D. Daudon, N. Bédouin, E. Collet, J. Lhuissier, and A.-M. Portal. Possible deviations from Griffith’s criterion in shallow slabs, and consequences on slab avalanche release. *Natural Hazards and Earth System Sciences*, 2:1–5, 2002.
- [51] P. Mahajan and S. K. Joshi. Modeling of interfacial crack velocities in snow. *Cold Reg. Sci. Technol.*, 51(2-3):98–111, 2008.
- [52] B. M. Malyshev and R. L. Salganik. The strength of adhesive joints using the theory of cracks. *Int. J. Fract. Mech.*, 5:114–128, 1965.
- [53] D. M. McClung. Shear fracture precipitated by strain softening as a mechanism of dry avalanche release. *J. Geophys. Res.*, 84(B7):3519–3526, 1979.
- [54] D. M. McClung. Fracture mechanical models of dry slab avalanche release. *J. Geophys. Res.*, 86(B11):10783–10790, 1981.
- [55] D. M. McClung. Approximate estimates for fracture speeds for dry slab avalanches. *Geophys. Res. Lett.*, 32:L08406, 2005.
- [56] D. M. McClung. Dry snow slab shear fracture speeds. *Geophys. Res. Lett.*, 34:L10502, 2007.

- [57] M. Mellor. A review of basic snow mechanics. In *The International Symposium on Snow Mechanics, Grindelwald, Switzerland, IAHS-AISH Publication 114*, pages 251–291, 1975.
- [58] H. Narita. Mechanical behavior and structure of snow under uniaxial tensile stress. *J. Glaciol.*, 26(94):275–282, 1980.
- [59] A. C. Palmer and J. R. Rice. The growth of slip surfaces in the progressive failure of over-consolidated clay. *Proceedings of the Royal Society of London, A*(332):527–548, 1973.
- [60] R. Perla, T. M. H. Beck, and T. T. Cheng. The shear-strength index of alpine snow. *Cold Reg. Sci. Technol.*, 6:11–20, 1982.
- [61] R. I. Perla and E. R. LaChapelle. A theory of snow slab failure. *J. Geophys. Res.*, 75(36):7619–7627, 1970.
- [62] M. Piche. A lifetime of learning in the winter of 2008. In *Proceedings of the 2008 International Snow Science Workshop, Whistler, Canada*, 2008.
- [63] C. Scapozza. *Entwicklung eines dichte- und temperaturabhngigen Stoffgesetzes zur Beschreibung des visko-elastischen Verhaltens von Schnee*. PhD thesis, ETH Zürich, 2004. Diss. ETH No. 15357.
- [64] J. Schweizer. Review of dry snow slab avalanche release. *Cold Reg. Sci. Technol.*, 30:43–57, 1999.
- [65] J. Schweizer, J. Bruce Jamieson, and M. Schneebeli. Snow avalanche formation. *Reviews of Geophysics*, 41:2–1, Nov. 2003.
- [66] J. Schweizer and C. Camponovo. The skiers zone of influence in triggering slab avalanches, *Ann. Glaciol. Ann. Glaciol.*, 32:314–320, 2002.
- [67] L. H. Shapiro, J. B. Johnson, M. Sturm, and G. L. Blaisdell. Snow mechanics. *CRREL Report*, 97(3), 1997.
- [68] C. Sigrist. *Measurement of fracture mechanical properties of snow and application to dry snow slab avalanches*. PhD thesis, ETH Zürich, 2006. Diss. ETH No. 16736.
- [69] C. Sigrist and J. Schweizer. Critical energy release rates of weak snowpack layers determined in field experiments. *Geophys. Res. Lett.*, 34:L03502, 2007.
- [70] C. Sigrist, J. Schweizer, H. J. Schindler, and J. Dual. On size and shape effects in snow fracture toughness measurements. *Cold Reg. Sci. Technol.*, 43(1-2):24–35, 2005.
- [71] C. Sigrist, J. Schweizer, H. J. Schindler, and J. Dual. The energy release rate of mode ii fractures in layered snow samples. *Int. J. Frac.*, 139(3-4):461–475, 2006.

- [72] R. Simenhois and K. Birkeland. A field test for fracture initiation and propagation. In *Proceedings of the 2006 International Snow Science Workshop, Telluride, Colorado*, 2006.
- [73] E. Sorge. The scientific results of the Wegener expedition to Greenland. *Geographical J. Lond.*, 81(4):333–344, 1933.
- [74] K. R. Sternlof, J. W. Rudnicki, and D. D. Pollard. Anticrack inclusion model for compaction bands in sandstone. *J. Geophys. Res.*, 110:B11403, 2005.
- [75] M. Stoffel and P. Bartelt. Modelling snow slab release using a temperature-dependent visoelastic finite element model with weak layers. *Surveys in Geophysics*, 24:417–430, 2003.
- [76] H. Tada, P. C. Paris, and G. R. Irwin. *The stress analysis of cracks handbook*. AMSE Press, New York, 2001.
- [77] I. Takei and N. Maeno. Mechanical vibration responses for snow samples near the melting temperature. *Ann. Glaciol.*, 38:130–134, 2004.
- [78] P. A. Thompson and G. S. Grest. Granular flow - friction and the dilatancy transition. *Phys. Rev. Lett.*, 67(13):1751–1754, 1991.
- [79] J. C. Truman. Wave propagation in snow. *Am. J. Phys.*, 41:282–283, 1973.
- [80] A. van Herwijnen. *Fractures in weak snowpack layers in relation to slab avalanche release*. PhD thesis, University of Calgary, 2005.
- [81] A. van Herwijnen, J. Heierli, and J. Schweizer. Field studies of collapse propagation in weak snow layers. In *EGU General Assembly, Vienna, Austria*, 2008.
- [82] A. van Herwijnen, J. Heierli, and J. Schweizer. Field study on fracture propagation in weak snowpack layers. In *Proceedings of the 2008 International Snow Science Workshop, Whistler, Canada*, 2008.
- [83] A. van Herwijnen and B. Jamieson. High-speed photography of fractures in weak snowpack layers. *Cold Reg. Sci. Technol.*, 43(1-2):71–82, 2005.
- [84] S. Weinberg. *The First Three Minutes: A Modern View of the Origin of the Universe*. Fontana, Oxford, 1977.
- [85] B. Wright. *Avalanche Card*. The Mountaineering Council of Scotland, The Old Granary, West Mill Street, Perth, PH1 5QP, Scotland, 2005.
- [86] M. Zaiser. Slab avalanche release viewed as interface fracture in a random medium. *Ann. Glaciol.*, 38:9–14, 2004.

Curriculum vitae bis Oktober 2008

Joachim Heierli

Geb. am 15 März 1964 in Richterswil, Schweiz.

Sprachen: Französisch, Deutsch und Englisch.

Schweizerische Staatsangehörigkeit.

Akademische Laufbahn:

- 10/2006 - heute Universität Karlsruhe, Fakultät für Maschinenbau,
Institut für Zuverlässigkeit von Bauteilen und Systemen.
Doktorand bei Prof. Peter Gumbsch.
- 10/1983 - 12/1988 Ecole polytechnique fédérale de Lausanne EPFL,
Physikstudium (Note 8/10) und *Physikdiplom* (Note 9/10).

Arbeitserfahrung:

- 1/2007 - heute University of Edinburgh, Institute of Materials and Processes,
Centre for Materials Science and Engineering,
Research associate bei Prof. Michael Zaiser.
Highlight: Publikation eines Artikels in der Zeitschrift Science.
- 8/2002 - 12/2006 Swiss Federal Institute for Snow and Avalanche Research SLF,
Wissenschaftlicher Angestellter unter der Leitung von Dr. J. Rhyner.
Highlight: Erste Publikation in einer Fachzeitschrift.
- 9/2000 - 7/2002 Siemens Building Technologies,
Softwareentwickler für web-basierte Fernsteuerung von
HLK Gebäudetechnik (Desigo PXweb).
- 6/1999 - 8/2000 Weltreise.
- 4/1997 - 5/1999 Boschung mecatronic,
Projektleiter Glatteis-Prognosemodelle unter der Leitung von Dr. E. Bornand.
Highlight: 1 internationales Patent.
- 8/1995 - 2/1997 Weltreise.
- 4/1992-7/1995 EMPA Materials Science and Technology, Abteilung Bauphysik,
Wissenschaftlicher Mitarbeiter unter der Leitung von Dr. T. Frank.
- 2/1989-3/1992 Werner Heierli GmbH,
Software- und Systementwickler für HLK Gebäudetechnik.